

**Electromagnetic properties of neutrinos and  
phenomenology of neutrino oscillations**

*By*

**Sandeep Joshi**

**PHYS01201604004**

**Bhabha Atomic Research Centre, Mumbai**

*A thesis submitted to the*

*Board of Studies in Physical Sciences*

*In partial fulfillment of requirements*

*For the Degree of*

**DOCTOR OF PHILOSOPHY**

*of*

**HOMI BHABHA NATIONAL INSTITUTE**



**December, 2020**

# Homi Bhabha National Institute

## Recommendations of the Viva Voce Committee

As members of the Viva Voce Board, we certify that we have read the dissertation prepared by **Sandeep Joshi** entitled "*Electromagnetic properties of neutrinos and phenomenology of neutrino oscillations*" and recommend that it maybe accepted as fulfilling the thesis requirement for the award of Degree of Doctor of Philosophy.

  
Chairman - Prof. A.K. Mohanty

Date:   
14-9-2021

  
Guide/Convener - Prof. Sudhir R. Jain

Date: 30-8-2021

  
Examiner - Prof. S. Uma Sankar

Date: 02/09/2021

  
Member 1 - Prof. Amol Dighe

Date: 02/09/2021

  
Member 2 - Prof. V.M. Datar

Date: 12/09/2021

  
Member 3 - Prof. L.M. Pant

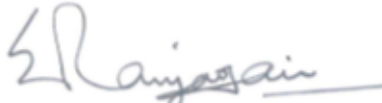
Date: 13/09/2021

Final approval and acceptance of this thesis is contingent upon the candidate's submission of the final copies of the thesis to HBNI.

I hereby certify that I have read this thesis prepared under my direction and recommend that it may be accepted as fulfilling the thesis requirement.

Date: 14-9-2021

Place: Mumbai



Guide

## STATEMENT BY AUTHOR

This dissertation has been submitted in partial fulfillment of requirements for an advanced degree at Homi Bhabha National Institute (HBNI) and is deposited in the Library to be made available to borrowers under rules of the HBNI.

Brief quotations from this dissertation are allowable without special permission, provided that accurate acknowledgement of source is made. Requests for permission for extended quotation from or reproduction of this manuscript in whole or in part may be granted by the Competent Authority of HBNI when in his or her judgement the proposed use of the material is in the interests of scholarship. In all other instances, however, permission must be obtained from the author.



**Sandeep Joshi**

## **DECLARATION**

I, hereby declare that the investigation presented in the thesis has been carried out by me.  
The work is original and has not been submitted earlier as a whole or in part for a degree  
/ diploma at this or any other Institution / University.

  
**Sandeep Joshi**

# List of Publications

## Refereed Journal

1. "Geometric phase for neutrino propagation in magnetic field", Sandeep Joshi and Sudhir R. Jain", Phys.Lett. B **754**, 135-138 (2016).
2. "Noncyclic geometric phases and helicity transitions for neutrino oscillations in a magnetic field", Sandeep Joshi and Sudhir R. Jain, Phys.Rev. D **96**, 096004 (2017).
3. "Neutrino spin-flavor oscillations in solar environment", Sandeep Joshi and Sudhir R. Jain, Res.Astron.Astrophys. **20(8)**, 123 (2020).
4. "Mixed state geometric phase for neutrino oscillations", Sandeep Joshi, Phys.Lett. B **809**, 135766 (2020).

## Conference Proceedings

1. "Geometric phase for neutrino propagation in a transverse magnetic field", S. Joshi and S.R. Jain, DAE Symp. Nucl. Phys. **60**, 842 (2015).
2. "Non-cyclic geometric phases for neutrino oscillations in uniformly twisting magnetic fields", S. Joshi and S.R. Jain, DAE Symp. Nucl. Phys. **61**, 896 (2016).
3. "Geometric Phases for Neutrino Oscillations in a Magnetic Field", S. Joshi, International Workshop on Applied Antineutrino Physics (IWAPP 2017) (Poster Presentation).
4. "Neutrino spin-flavor oscillations in the Sun: Differences between Dirac and Majorana neutrinos", S. Joshi and S.R. Jain, DAE Symp. Nucl. Phys. **63**, 1024 (2018).
5. "Coherence measure of neutrino oscillations", S. Joshi and S.R. Jain, DAE Symp. Nucl. Phys. **64**, 845 (2019).

## ACKNOWLEDGEMENTS

As I write the final page of this dissertation, the first person whom I would like to acknowledge is my advisor Prof. Sudhir R. Jain. It was only due to his continuous support, encouragement and guidance that this journey became exciting and fruitful. The amount of confidence he shows in the ideas of younger colleagues is unparalleled and quite encouraging. He has inspired me in so many different ways throughout these years.

The members of my doctoral committee played an important role in improving my understanding of the subject through their thought-provoking questions and invaluable suggestions. I would specially like to thank Prof. Amol Dighe and Prof. V.M. Datar for sharing their expertise. I would also like express my gratitude to Prof. A.K. Mohanty and Prof. L.M. Pant for their support and encouragement. Dr. Alok Saxena and Dr. E.T. Mirgule supported me during the initial days of my PhD. My sincere thanks to them as well.

I would also like to take this opportunity to acknowledge my fellow colleagues and friends. I am particularly thankful to Nischal, Harish, Jyoti, Garima, Komal, Rakesh, Abhay and Laxman sir for several interesting discussions on physics and non-physics related issues. My all-weather friends Prakash, Santosh, Prashant, Vinay, Vijay, Teja, Somananda and Sarita deserve special acknowledgement for making my life easier on several occasions.

A task of this magnitude cannot be completed without an ecosystem of strong personal support. I would specially like to mention the three pillars of my life: my mother who is my strongest support, my wife Bhawna who is always caring and encouraging and our daughter Subhashini who is a source of immense joy. I am also grateful to my sisters for their care and affection and their daughters Yashvi, Navika and Trishika who always cheer me up.

Finally, I would like to dedicate this Thesis to my Late father who always supported me and motivated me to do well in life.



# Contents

<b>Summary</b>	<b>i</b>
<b>List of Figures</b>	<b>iii</b>
<b>List of Tables</b>	<b>vi</b>
<b>1 Introduction</b>	<b>1</b>
1.1 Gauge Theories and the Standard Model . . . . .	2
1.1.1 $SU(2)_L \times U(1)_Y$ Electroweak theory . . . . .	5
1.1.2 Spontaneous symmetry breaking and particle spectrum . . . . .	7
1.2 Neutrino mass, mixing and oscillations . . . . .	13
1.2.1 Neutrino mixing . . . . .	16
1.2.2 Neutrino oscillations . . . . .	18
1.2.3 Neutrino oscillations in matter . . . . .	21
1.3 Overview of the thesis . . . . .	26
<b>2 Electromagnetic properties of neutrinos</b>	<b>29</b>
2.1 Electromagnetic form factors . . . . .	29
2.1.1 Dirac neutrinos . . . . .	31
2.1.2 Majorana neutrinos . . . . .	33
2.2 Neutrino dipole moments (NDM) . . . . .	36
2.2.1 Theoretical predictions in MESM . . . . .	36
2.2.2 Experimental limits and large magnetic moments . . . . .	39
2.3 Neutrino interaction with electromagnetic fields . . . . .	45
2.3.1 Neutrino spin and spin-flavor precession . . . . .	50
2.3.2 Two flavor Dirac and Majorana Hamiltonian . . . . .	56
<b>3 Neutrino spin-flavor oscillations in solar environment</b>	<b>61</b>
3.1 Introduction . . . . .	61
3.1.1 Solar neutrino production and flavor transitions . . . . .	63
3.1.2 Spin-flavor precession of solar neutrinos . . . . .	67
3.2 Magnetic field in the Sun . . . . .	69
3.3 An analytical model for zero vacuum mixing . . . . .	74

3.4	Including effects of $\theta_{12}$ . . . . .	77
3.5	Comparison with Borexino results . . . . .	81
3.6	Conclusions . . . . .	83
<b>4</b>	<b>Neutrino propagation in magnetic fields and geometric phases</b>	<b>87</b>
4.1	Introduction . . . . .	88
4.1.1	Adiabaticity and Berry's Phase . . . . .	90
4.1.2	Example- Spin precession in a magnetic field . . . . .	94
4.1.3	Aharonov- Anandan phase . . . . .	95
4.1.4	Noncyclic Geometric Phase . . . . .	97
4.2	Neutrino propagation in magnetic fields . . . . .	99
4.3	Bloch sphere representation of neutrino spin rotation and noncyclic geometric phases . . . . .	102
4.4	Neutrino Propagation in Neutron Stars . . . . .	107
4.4.1	Adiabaticity and Geometric phases . . . . .	109
4.4.2	Transition probabilities and cross boundary effect . . . . .	112
4.5	Possible methods of geometric phase detection . . . . .	114
4.6	Conclusions . . . . .	115
<b>5</b>	<b>Mixed state geometric phase for neutrino oscillations</b>	<b>119</b>
5.1	Introduction . . . . .	119
5.2	Mixed state geometric phase . . . . .	122
5.3	Two flavor neutrino oscillations . . . . .	124
5.3.1	Geometric phase versus quantum coherence . . . . .	131
5.4	Three flavor oscillations . . . . .	132
5.5	Conclusions . . . . .	134
<b>6</b>	<b>Summary and Outlook</b>	<b>137</b>
<b>A</b>	<b>Neutrino oscillations, wave packets and decoherence</b>	<b>143</b>
<b>B</b>	<b>Neutrino evolution equations and Demkov-Kunike model</b>	<b>159</b>
	<b>References</b>	<b>163</b>

# Summary

Neutrinos are one of the most intriguing particles of the Standard Model. The observation of oscillation among different neutrino flavors suggest the existence of an extended theory beyond the Standard Model. These extended theories have several new phenomenological features which might be detected in future neutrino experiments. One such possibility is the existence of neutrino electromagnetic interactions. Despite being electrically neutral, neutrinos acquire their electromagnetic properties through interaction with photons at quantum loop level. This can generate important new effects such as neutrino spin-flavor oscillations in the presence of background electromagnetic fields.

In the present Thesis, we study the phenomenology of neutrino flavor and spin-flavor oscillations in solar and astrophysical environments. In solar interiors the magnetic fields may be sufficiently large to cause appreciable neutrino transitions. Thus the solar neutrinos detected at Earth may act as a messenger of information about the solar magnetic fields. Using the current bounds on Helioseismology we construct analytical models for the magnetic field in all the three regions of the Sun. The  ${}^8B$  neutrinos produced in the solar interior may undergo transitions  $\nu_{eL} \rightarrow \bar{\nu}_{\mu R} \rightarrow \bar{\nu}_e$  due to combined effect of magnetic field and vacuum mixing. We numerically evaluate these transition probabilities and compare our results with the Borexino experiment to place bounds on the solar magnetic fields. It is found that whereas the Borexino bounds are too weak to place any upper limit on the magnetic field in the radiative zone of the Sun, for the solar core magnetic field we

are able to place an upper bound  $B_0 < 1.1 \times 10^6 \text{G}$ , which is an improvement by a factor of almost one-seventh of the current largest helioseismological bound. We also study neutrino spin transitions for neutrinos produced in extreme environments such as neutron stars (NS) using realistic density and magnetic field profiles. We show that while inside the NS the neutrino propagation is highly adiabatic, as the neutrinos come out of the NS the non-adiabatic effects start to become more important and at a distance of about 200 times the radius of a NS, the initial flux of left-handed neutrinos produced inside the NS is depleted to half of its original value.

The study of geometric properties of neutrino flavor and spin-flavor oscillations brings important new insights about the nature of this phenomenon. In this geometric picture the neutrino propagation in space can be visualized by studying the trajectory of neutrino spin-polarization vector in the projective Hilbert space of the system. Such an evolution is known to give rise to geometric phase due to non-trivial geometry of the projective Hilbert space. In case of spin precession  $\nu_L \rightarrow \nu_R$  of pure neutrino states, the neutrino spin-polarization traces out cyclic and noncyclic curves on the Bloch sphere for different parameters of the Hamiltonian. We derive analytical expressions for adiabatic, non-adiabatic and noncyclic geometric phases for different astrophysical environments. We show that the area enclosed by the trajectory of the curves on the Bloch sphere is related to the geometric phases acquired by the neutrino state during evolution.

We also discuss the geometric properties of neutrino flavor oscillation using density matrix formalism. For two flavor oscillations, the geometric phase is shown to be independent of the Majorana phase. We also show that the geometric phase can be used as a measure of coherence of the neutrino beam. In addition, our expressions of the mixed state geometric phase are a generalization of the previously obtained results of the pure state geometric phase for both two and three flavor neutrino oscillations.

# List of Figures

1.1	Tree-level Feynman diagrams of the elastic scattering of neutrinos with the background matter particles, which generate (a) charged-current potential $V_{CC}$ and (b) neutral-current potential $V_{NC}$ . . . . .	22
2.1	Effective vertex for neutrino-photon interaction. . . . .	30
2.2	One loop Feynman diagrams contributing to the Dirac neutrino vertex function in the MESM in the unitary gauge; $\alpha = e, \mu, \tau$ and $i, j = 1, 2, 3$ . In the renormalizable $R_\xi$ gauge there are extra diagrams in which internal $W$ lines are replaced by unphysical Higgs lines . . . . .	37
2.3	Typical Feynman diagrams contributing to the NMM vertex function at one-loop level. The cross in (a) and (b) represents mass insertion at external and internal fermion line respectively. In (b) the black dot shows $W_L - W_R$ mixing. . . . .	42
3.1	Schematic diagram of the solar $pp$ fusion chain. The neutrinos emitted in different reactions are marked in red. (Figure taken from Ref. ). . . . .	63
3.2	Energy spectrum of the solar neutrinos produced in different reactions in the $pp$ chain. (Figure taken from Ref. ). . . . .	64
3.3	Production of different components of the solar neutrinos as a function of distance from the center of the Sun (expressed in units of solar radius $R_\odot$ ). (Figure taken from Ref. ). . . . .	65
3.4	The solar $\nu_e$ survival probability as a function of energy (pink curve) with oscillation parameters obtained in Ref. . The data points with error bars show the Borexino measurements reported in Ref. . . . .	66
3.5	The longitudinal neutrino spin polarization $S_{\parallel}$ as it propagates in the magnetic field of the Sun. The solid curve is the magnetic field obtained by solving solar MHD equations in . The dashed curve is given by Eq. (3.9) and the dot-dashed curve by Eq. (3.10). The peak magnetic field for both models is taken to be $\approx 10^4$ G. . . . .	71
3.6	Electron number density variation vs. radial distance in the Sun. The <i>solid line</i> represents the solar model BS(2005) and the <i>dashed curves</i> are analytical approximations. . . . .	74

3.7	Transition probability of Dirac and Majorana neutrinos obtained from the solution of equation (3.21). Here the neutrinos are assumed to be produced at the center of the Sun with energy $E = 10$ MeV. . . . .	76
3.8	Eigenvalues of the Hamiltonian for $E = 10$ MeV neutrinos: (a) in the flavor basis, Eq. (3.25) for $\theta_{12} \approx 0$ . The two level <i>crossing points</i> correspond to SFP and MSW resonances. (b) in the mass eigenbasis, Eq. (3.27) for $\theta_{12} = 33.8^\circ$ . The <i>dashed/dot-dashed lines</i> correspond to $\nu_1/\nu_2$ respectively and the solid line represents $\bar{\nu}_\mu$ . Here we have used $B_0 = 10^6$ G and the eigenvalues are in dimensionless units. . . . .	79
3.9	The variation of probability $P(\nu_{eL} \rightarrow \bar{\nu}_{\mu R})$ with distance inside the Sun for maximum RZ magnetic field $B_0 = 10^6$ G. The neutrinos are assumed to be produced at the center of the Sun and $E = 10$ MeV. . . . .	81
3.10	The probability of solar electron neutrino ( $E = 10$ MeV) to anti-neutrino conversion at the Earth's surface (Eq. (3.24)) and comparison with Borexino results. The <i>dashed(red) curve and dotdashed(brown) curve</i> show the probability $P(\nu_e \rightarrow \bar{\nu}_e)$ calculated using the two field profiles marked with respective curves in Fig. 3.5. The <i>dotted(blue) line</i> signifies that the current upper bound $P(\nu_e \rightarrow \bar{\nu}_e) < 1.3 \times 10^{-4}$ from the Borexino experiment corresponds to a bound of $2.1 \times 10^8$ G on the RZ magnetic field and to a bound of $1.1 \times 10^6$ G on the core magnetic field. The <i>solid(black) lines</i> mark the helioseismological bounds of 30 MG and 7 MG on the RZ and solar core magnetic fields respectively. . . . .	82
4.1	Parallel transport on the surface of a sphere. The vector, initially located at the north pole, is parallel-transported along the path $C$ . As it returns to initial position, it gets rotated by an amount $\gamma$ that depends on the path $C$ traversed by the vector. . . . .	89
4.2	Cyclic evolution of vector in projective Hilbert state $\mathcal{P}(\mathcal{H})$ . A closed curve $\mathcal{C} = \pi(C)$ in $\mathcal{P}(\mathcal{H})$ can have infinitely many lifts in $\mathcal{H}$ which may or may not be closed. This is called principal fiber bundle picture of the state space. The bundle space $\mathcal{H}$ consists of three parts: the base manifold $\mathcal{P}(\mathcal{H})$ , the fiber which is the group $U(1)$ attached to each point of base manifold and the map $\pi : \mathcal{H} \rightarrow \mathcal{P}(\mathcal{H})$ . A closed curve in the bundle space begins and ends on the same fiber.(Figure taken from Ref. ). . . . .	96

4.3	Bloch sphere representation of neutrino spin rotation. Initially the neutrinos are produced in the left helicity state which corresponds to a point on the pole of the sphere. Under the effect of matter and magnetic field, neutrinos undergo spin-precession $\nu_{eL} \rightarrow \nu_{eR}$ and neutrino spin-vector $\mathbf{n}$ traces out cyclic [(a) and (b)] and noncyclic curves [(c) and (d)] on the Bloch sphere depending on the relative values of $\dot{\phi}_p$ and the parameters of $\mathbf{B}_{\text{eff}}$ . The circular curve describes the path of $\mathbf{B}_{\text{eff}}$ . The rotation frequency is in units of $\pi/R$ , and the positive and negative signs of $\dot{\phi}$ correspond to clockwise and anticlockwise rotation of the magnetic field about the neutrino direction respectively. We used the following parameters: electron number density $n_e = 10^{24} \text{g/cm}^3$ , neutron number density $n_n = n_e/6$ , matter potential $V = \sqrt{2}G_F(n_e - n_n/2)$ , and magnetic field strength $B = 10^6 \text{ G}$ . . . . .	104
4.4	Geometric phases associated with the curves in the Bloch sphere for neutrino spin-precession $\nu_{eL} \rightarrow \nu_{eR}$ . . . . .	105
4.5	(a) Density and (b) magnetic field profiles of the neutron star. Magnetic field is plotted in log scale. . . . .	108
4.6	$\log \gamma(z)$ as a function of distance (a) inside and (b) outside the NS. The adiabaticity condition $\gamma \gg 1$ is satisfied for all values of $\dot{\phi}$ while for the outside regions adiabaticity holds only in a limited region. . . . .	111
4.7	Geometric phases neutrino propagation in NS. In (a) the flat portion of the curve corresponds to neutrino propagation inside the NS, where the geometric phase is almost zero. In (b) $\dot{\phi}_{\text{res}}$ corresponds to the resonant condition $V = -\dot{\phi}$ . . . . .	112
4.8	Neutrino survival probability of spin and spin-flavor precession for various values of the rotation frequency. Nonzero values of $\dot{\phi}$ lead to suppression of transitions and the probability converges to one-half at a faster rate compared to the case when $\dot{\phi} = 0$ . For the case of spin transitions in nonrotating magnetic fields the probability does not converge to 0.5 but instead approaches 1 in the limit $z \gg R$ . This is because for this case $\cos \theta_{\text{eff}} = 0$ and the oscillatory term in Eq. (4.71) converges to 1 in the limit $z \gg R$ . . . . .	114
5.1	Comparison of mixed state geometric phase (5.31) and quantum coherence (5.37) with respect to coherence parameter $w_e - w_\mu$ . The neutrino oscillation parameters are taken as: $\Delta m^2 = 2.5 \times 10^{-3} \text{ eV}^2$ , $\theta = 48.6^\circ$ , $L/E = 520 \text{ (km/GeV)}$ . . . . .	132

# List of Tables

1.1	The quantum numbers of the fermion doublet and singlet fields, and the Higgs field $\Phi$ in the SM. Also shown are the quantum numbers for the right-handed neutrino fields in the extended SM. . . . .	6
1.2	Best fit values of the neutrino oscillation parameters . . . . .	21
3.1	The location of SFP resonance in the Sun (in units $r/R_{\odot}$ ) for different neutrino energies. . . . .	73

---

## CHAPTER 1

---

### Introduction

---

Modern physics rests firmly on two pillars: quantum mechanics and general theory of relativity. While quantum mechanics describes the nature of matter at extremely small subatomic scales, general relativity is required for large scales where the gravitational effects become important. The quantum mechanics of all the known fundamental particles and their interactions is formulated by the Standard Model (SM) of particle physics. This model describes the fundamental building blocks of matter, quarks and leptons, and their governing forces: the strong, electromagnetic and weak interactions, in a single mathematical framework. The SM, developed in the 1970s, has not only been able to explain almost all of the experimental results, but it also predicted new particles and phenomena, which were discovered in subsequent experiments. For example, the existence of charm, bottom and top quarks, massive  $W$  and  $Z$  vector bosons, the tau neutrino, scalar Higgs boson and the neutral current interactions were all successful predictions of the SM.

## 1.1 Gauge Theories and the Standard Model

The SM has two main components: local gauge invariance and spontaneous symmetry breaking. The local gauge invariance determines the interactions of the gauge fields and the number of gauge bosons in the SM. It also forces the gauge fields and the matter fields to remain massless. The particles acquire their masses due to spontaneous symmetry breaking by the scalar Higgs field [1–7].

To illustrate the principle of local gauge invariance consider the Lagrangian of a free Dirac field  $\Psi(x)$ :

$$\mathcal{L}_0 = \bar{\Psi}(x)(i\rlap{\not{D}} - m)\Psi(x), \quad (1.1)$$

where  $\rlap{\not{D}} = \gamma^\mu \partial_\mu$ . The gauge principle demands that under the transformation

$$\Psi(x) \rightarrow e^{i\alpha(x)}\Psi(x), \quad (1.2)$$

where  $\alpha(x)$  depends on the space-time coordinate  $x$ , the Lagrangian should remain invariant. However, it can be seen that under this transformation  $\partial_\mu \Psi(x) \rightarrow e^{i\alpha(x)}(\partial_\mu \Psi(x) + i\partial_\mu \alpha(x)\Psi(x))$ , thus  $\mathcal{L}_0$  does not remain invariant. To restore the gauge invariance we need to introduce a new gauge field  $A_\mu$  to cancel out the extra term. We thus define covariant derivative

$$D_\mu = \partial_\mu + ieA_\mu(x), \quad (1.3)$$

such that under the transformation (1.2):

$$A_\mu(x) \rightarrow A_\mu(x) - \frac{1}{e}\partial_\mu \alpha(x), \quad (1.4)$$

which results in  $D_\mu \Psi(x) \rightarrow e^{i\alpha(x)}D_\mu \Psi(x)$ . We can now write a locally gauge invariant Lagrangian

$$\mathcal{L} = \bar{\Psi}(x)(i\rlap{\not{D}} - m)\Psi(x) = \mathcal{L}_0 - e\bar{\Psi}(x)\gamma^\mu\Psi(x)A_\mu. \quad (1.5)$$

Thus the demand for the local gauge invariance results in an interaction term between the Dirac fermion and the gauge field  $A_\mu(x)$ , which is the familiar electron-photon vertex of quantum electrodynamics (QED). The QED represents an archetypal gauge theory which exhibits local  $U(1)$  gauge invariance. The full Lagrangian for QED includes a kinetic term for the propagating photon field  $A_\mu(x)$ :

$$\mathcal{L}_{\text{QED}} = -\frac{1}{4}F_{\mu\nu}F^{\mu\nu} + \bar{\Psi}(x)(i\not{D} - m)\Psi(x), \quad (1.6)$$

where  $F_{\mu\nu} = \partial_\mu A_\nu - \partial_\nu A_\mu$  is the electromagnetic field strength tensor which remains invariant under the transformation (1.2).

The idea of local gauge invariance was extended to non-Abelian groups by Yang-Mills [8], which ultimately led to the formulation of the SM. Of particular interest is the the Lie group  $SU(N)$  having  $N^2 - 1$  generators, which obey the commutation relation

$$[t^a, t^b] = if^{abc}t^c, \quad (1.7)$$

where  $f^{abc}$  are the structure constants of the group. The local gauge transformation for the spinor field  $\Psi(x) = (\psi_1(x), \psi_2(x), \dots, \psi_N(x))^T$  can be realized by an  $SU(N)$  matrix  $U(x)$  in the following manner:

$$\Psi(x) \rightarrow U(x)\Psi(x) = e^{i\theta^a(x)T^a}\Psi(x), \quad (1.8)$$

where  $T^a$  is the matrix representation of the generators  $t^a$ ,  $\theta^a(x)$  are space-time dependent real functions and the index  $a$  is summed over from 1 to  $N^2 - 1$ . As in the Abelian case, to preserve the gauge invariance one needs to introduce a set of  $N^2 - 1$  gauge fields by defining the covariant derivative:

$$D_\mu = \partial_\mu + igT^a A_\mu^a(x), \quad (1.9)$$

such that the gauge fields  $A_\mu^a(x)$  transform as

$$T^a A_\mu^a(x) \rightarrow UT^a A_\mu^a(x)U^{-1} + \frac{i}{g}(\partial_\mu U)U^{-1}. \quad (1.10)$$

The explicit transformation of the gauge fields can be obtained by considering the infinitesimal transformation

$$\Psi(x) \rightarrow (1 + i\delta\theta^a(x)T^a)\Psi(x), \quad (1.11)$$

from which we get

$$A_\mu^a(x) \rightarrow A_\mu^a(x) - \frac{1}{g}\partial_\mu\delta\theta^a - f^{abc}\delta\theta^b A_\mu^c. \quad (1.12)$$

The non-Abelian generalization of the kinetic term of the gauge fields can be found by requiring the field strength tensor to transform as

$$F_{\mu\nu}^a T^a \rightarrow UF_{\mu\nu}^a T^a U^{-1}, \quad (1.13)$$

which leads to

$$F_{\mu\nu}^a T^a = -\frac{i}{g}[D_\mu, D_\nu], \quad (1.14)$$

$$F_{\mu\nu}^a = \partial_\mu A_\nu^a - \partial_\nu A_\mu^a - gf^{abc}A_\mu^b A_\nu^c. \quad (1.15)$$

Finally, the full Lagrangian for the non-Abelian  $SU(N)$  gauge theory interacting with the fermion field can be written as

$$\mathcal{L} = -\frac{1}{4}F_{\mu\nu}^a F^{a\mu\nu} + \bar{\Psi}(x)(i\not{D} - m)\Psi(x). \quad (1.16)$$

From Eqs. (1.15) and (1.16) it can be easily checked that the Lagrangian contains terms which are cubic and quartic in  $A_\mu^a$ . These terms give rise to self-interactions among the gauge fields, which were absent in the case of QED. All the interaction terms involve the coupling constant  $g$  which is thus universal. Also it can be noticed that there are no mass

terms for the gauge fields in the Lagrangian (1.16), since a term of the form  $m^2 A_\mu^a A^{a\mu}$  explicitly breaks the gauge invariance of the theory. Thus the gauge fields remain massless.

### 1.1.1 $SU(2)_L \times U(1)_Y$ Electroweak theory

The SM is a non-Abelian gauge theory based on the symmetry group  $SU(3)_C \times SU(2)_L \times U(1)_Y$ , where  $SU(3)_C$  corresponds to the color symmetry of strong interactions,  $SU(2)_L$  corresponds to the weak isospin symmetry and  $U(1)_Y$  corresponds to the hypercharge symmetry. The electroweak sector  $SU(2)_L \times U(1)_Y$  of the SM describes the weak and electromagnetic interactions in a unified manner. The weak isospin group  $SU(2)_L$  act on the left-handed chiral components of the fermion fields, while the right-handed components are  $SU(2)_L$  singlets. This group has three generators  $T^a$ ,  $a = 1, 2, 3$ . In the fundamental representation the generators are given by the Pauli matrices :  $T^a = \sigma^a/2$ , which satisfy the commutation relation

$$\left[ \frac{\sigma^a}{2}, \frac{\sigma^b}{2} \right] = i\epsilon^{abc} \frac{\sigma^c}{2}. \quad (1.17)$$

The Abelian group  $U(1)_Y$  is generated by the hypercharge operator which is related to the weak isospin  $T^3$  and charge operator  $Q$ :

$$Y = Q - T^3. \quad (1.18)$$

The matter content of the SM consist of quarks and leptons which are organized in three generations. The left-handed fermions are assigned to be  $SU(2)_L$  doublets while the right-handed fermions are represented by  $SU(2)_L$  singlets:

$$Q_L = \begin{pmatrix} u_L \\ d_L \end{pmatrix}, \begin{pmatrix} c_L \\ s_L \end{pmatrix}, \begin{pmatrix} t_L \\ b_L \end{pmatrix}; \quad L_L = \begin{pmatrix} \nu_{eL} \\ e_L \end{pmatrix}, \begin{pmatrix} \nu_{\mu L} \\ \mu_L \end{pmatrix}, \begin{pmatrix} \nu_{\tau L} \\ \tau_L \end{pmatrix} \quad (1.19)$$

$$U_R = u_R, c_R, t_R; \quad D_R = d_R, s_R, b_R; \quad E_R = e_R, \mu_R, \tau_R. \quad (1.20)$$

Particle content	Isospin $T$	Isospin $T^3$	Hypercharge $Y$	Electric charge $Q$
$Q_L = \begin{pmatrix} u_L \\ d_L \end{pmatrix}, \begin{pmatrix} c_L \\ s_L \end{pmatrix}, \begin{pmatrix} t_L \\ b_L \end{pmatrix}$	1/2	1/2 -1/2	1/6	2/3 -1/3
$L_L = \begin{pmatrix} \nu_{eL} \\ e_L \end{pmatrix}, \begin{pmatrix} \nu_{\mu L} \\ \mu_L \end{pmatrix}, \begin{pmatrix} \nu_{\tau L} \\ \tau_L \end{pmatrix}$	1/2	1/2 -1/2	-1/2	0 -1
$U_R = u_R, c_R, t_R$	0	0	2/3	2/3
$D_R = d_R, s_R, b_R$	0	0	-1/3	-1/3
$E_R = e_R, \mu_R, \tau_R$	0	0	-1	-1
$\Phi = \begin{pmatrix} \phi^+ \\ \phi^0 \end{pmatrix}$	1/2	1/2 -1/2	1/2	1 0
$\nu_R = \nu_{eR}, \nu_{\mu R}, \nu_{\tau R}$	0	0	0	0

Table 1.1: The quantum numbers of the fermion doublet and singlet fields, and the Higgs field  $\Phi$  in the SM. Also shown are the quantum numbers for the right-handed neutrino fields in the extended SM.

Table 1.1 lists the quantum numbers of the particles in the SM.

In order to have local gauge invariance in the theory, we must introduce three gauge fields  $W_\mu^a$  ( $a = 1, 2, 3$ ) associated with the generators of the group  $SU(2)_L$ , and one vector field  $B_\mu$  associated with the generator of the group  $U(1)_Y$ . The gauge invariant Lagrangian for the matter fields is then given by

$$\mathcal{L}_{\text{matter}} = \bar{Q}_{\alpha L} i \not{D} Q_{\alpha L} + \bar{L}_{\alpha L} i \not{D} L_{\alpha L} + \bar{U}_{\alpha R} i \not{D}' U_{\alpha R} + \bar{D}_{\alpha R} i \not{D}' D_{\alpha R} + \bar{E}_{\alpha R} i \not{D}' E_{\alpha R}, \quad (1.21)$$

where the index  $\alpha$  is summed over the three generations of quarks and leptons. The covariant derivatives in Eq. (1.21) have the form:

$$D_\mu = \partial_\mu + ig \frac{\sigma^a}{2} W_\mu^a + ig' Y B_\mu, \quad (1.22)$$

$$D'_\mu = \partial_\mu + ig' Y B_\mu, \quad (1.23)$$

where  $g$  and  $g'$  are the coupling constants for the groups  $SU(2)_L$  and  $U(1)_Y$  respectively. Also, the kinetic term for the gauge fields  $W_\mu^a$  and  $B_\mu$  can be expressed as

$$\mathcal{L}_{\text{gauge}} = -\frac{1}{4}B_{\mu\nu}B^{\mu\nu} - \frac{1}{4}W_{\mu\nu}^a W^{a\mu\nu}, \quad (1.24)$$

where field strength tensor is given by

$$B_{\mu\nu} = \partial_\mu B_\nu - \partial_\nu B_\mu, \quad (1.25)$$

$$W_{\mu\nu}^a = \partial_\mu W_\nu^a - \partial_\nu W_\mu^a - g\epsilon^{abc}W_\mu^b W_\nu^c. \quad (1.26)$$

As discussed in the last Section, the gauge symmetry forbids a mass term for the gauge fields in the theory. Now, the mass term for the fermions has the form:  $m\bar{\psi}\psi = m(\bar{\psi}_L\psi_R + \text{h.c.})$ . Since the left-handed and right-handed fermion fields have different transformations under the gauge group  $SU(2)_L \times U(1)_Y$ , this term is not gauge invariant and cannot be included in the Lagrangian (1.21). Hence in this model we obtain massless gauge and matter fields.

Now the gauge symmetry  $SU(2)_L \times U(1)_Y$  must be spontaneously broken to  $U(1)_Q$  at low energies, since only the electric charge  $Q$  is conserved in nature. The mechanism responsible for this symmetry breaking, known as the Higgs mechanism, also generates mass of the gauge bosons and the fermions.

### 1.1.2 Spontaneous symmetry breaking and particle spectrum

To break the gauge symmetry spontaneously we introduce the Higgs field  $\Phi$  which is represented by an  $SU(2)_L$  doublet of complex scalar fields

$$\Phi = \begin{pmatrix} \phi^+ \\ \phi^0 \end{pmatrix}, \quad Y = +1/2, \quad (1.27)$$

where  $\phi^+$  charged and  $\phi^0$  is neutral. The Lagrangian for the Higgs field  $\Phi$  is given by

$$\mathcal{L}_{\text{Higgs}} = (D_\mu \Phi)^\dagger D^\mu \Phi - \mu^2 \Phi^\dagger \Phi - \lambda (\Phi^\dagger \Phi)^2, \quad (1.28)$$

where  $\mu^2$  is real,  $\lambda > 0$  to have lower bound on the potential and  $D_\mu$  is given by Eq. (1.22) with  $Y = +1/2$ . In order to find the particle spectrum we must determine the vacuum state of the theory which corresponds to the ground state of the Higgs potential:

$$V(\Phi) = \mu^2 \Phi^\dagger \Phi + \lambda (\Phi^\dagger \Phi)^2. \quad (1.29)$$

Minimizing  $V(\Phi)$  gives us the ground state configuration of the system. If  $\mu^2 > 0$ , the potential minimum is located at the origin  $\langle \Phi \rangle = 0$ . Thus we have a symmetric ground state which is invariant under the gauge transformations and the gauge symmetry is preserved. On the other hand if  $\mu^2 < 0$ , the minimum of potential occurs at

$$\langle \Phi^\dagger \Phi \rangle = \frac{-\mu^2}{2\lambda} = \frac{v^2}{2}, \quad (1.30)$$

where  $v = \sqrt{-\mu^2/\lambda}$  is called the vacuum expectation value (vev) of the Higgs field. Since the vacuum must be electrically neutral, the vev is due to  $\phi^0$ . We thus obtain an infinite set of degenerate ground states from which a particular state can be chosen as the vacuum:

$$\langle \Phi \rangle = \frac{1}{\sqrt{2}} \begin{pmatrix} 0 \\ v \end{pmatrix}. \quad (1.31)$$

The above vacuum state is not invariant under the symmetry of the Lagrangian (1.28). Thus the gauge symmetry  $SU(2)_L \times U(1)_Y$  is spontaneously broken by the vacuum. However, the vacuum remains invariant under the transformations of the group  $U(1)_Q$  since the Higgs field has zero  $U(1)_Q$  charge. This results in the appearance of a massless gauge boson which can be identified with the photon. The spontaneous symmetry breaking also leads to the mass of the gauge fields  $W_\mu^a$ . To see this, we parametrize the Higgs doublet

in the general form

$$\Phi(x) = e^{i\sigma^a \xi^a(x)/2v} \frac{1}{\sqrt{2}} \begin{pmatrix} 0 \\ v + h(x) \end{pmatrix}, \quad (1.32)$$

where  $\xi^a(x) = (\xi^1(x), \xi^2(x), \xi^3(x))$  and  $h(x)$  are the four real scalar fields. The perturbative field  $h(x)$  describes the excitations of the Higgs field above vacuum. On the other hand, the fields  $\xi^a(x)$  can be rotated away by the following transformation:

$$\Phi(x) \rightarrow U(\xi)\Phi(x) = e^{-i\sigma^a \xi^a(x)/2v} \Phi(x), \quad (1.33)$$

This transformation defines the unitary gauge and in this gauge the Higgs doublet is given by

$$\Phi(x) = \frac{1}{\sqrt{2}} \begin{pmatrix} 0 \\ v + h(x) \end{pmatrix}, \quad (1.34)$$

At the same time the gauge fields  $W_\mu^a$  are subjected to the transformation given by Eq. (1.10)

$$\frac{\sigma^a W_\mu^a}{2} \rightarrow U(\xi) \frac{\sigma^a W_\mu^a}{2} U^{-1}(\xi) + \frac{i}{g} (\partial_\mu U(\xi)) U^{-1}(\xi). \quad (1.35)$$

In this manner the three unphysical Goldstone bosons  $\xi_\mu^a$  ( $a = 1, 2, 3$ ) are absorbed into the gauge transformation i.e. into the longitudinal modes of the gauge bosons to make them massive. This is known as the Higgs mechanism [9–12]. The particle spectrum of the theory after spontaneous symmetry breaking has the following components:

(i) A linear combination of the gauge fields  $W_\mu^a$  ( $a = 1, 2, 3$ ) and  $B_\mu$  gives us three massive bosons which are identified with the  $W^\pm$  and  $Z$  bosons, while the fourth linear combination which remains massless is the photon. Consider the first term in the Higgs Lagrangian

(1.28):

$$\begin{aligned}
(D_\mu \Phi)^\dagger D^\mu \Phi &= \left| \left( \partial_\mu + ig \frac{\sigma^a}{2} W_\mu^a + i \frac{g'}{2} B_\mu \right) \begin{pmatrix} 0 \\ \frac{v+h(x)}{\sqrt{2}} \end{pmatrix} \right|^2 \\
&= \frac{1}{2} (\partial_\mu h(x))^2 + \frac{1}{8} (v+h(x))^2 \left( g^2 (W_\mu^1 W^{1\mu} + W_\mu^2 W^{2\mu}) + \right. \\
&\quad \left. (-gW_\mu^3 + g'B_\mu)^2 \right). \tag{1.36}
\end{aligned}$$

We define the charged and neutral physical gauge bosons as

$$W_\mu^\pm = \frac{1}{\sqrt{2}} (W_\mu^1 \pm iW_\mu^2), \tag{1.37}$$

$$\begin{pmatrix} A_\mu \\ Z_\mu \end{pmatrix} = \begin{pmatrix} \cos \theta_W & \sin \theta_W \\ -\sin \theta_W & \cos \theta_W \end{pmatrix} \begin{pmatrix} B_\mu \\ W_\mu^3 \end{pmatrix}, \tag{1.38}$$

where the angle  $\theta_W$  is called the weak mixing angle or the Weinberg angle, defined by [13]

$$\tan \theta_W = \frac{g'}{g}. \tag{1.39}$$

In terms of the new fields the Lagrangian term (1.36) becomes

$$(D_\mu \Phi)^\dagger D^\mu \Phi = \frac{1}{2} (\partial_\mu h(x))^2 + (v+h(x))^2 \left( \frac{g^2}{4} W_\mu^+ W^{-\mu} + \frac{g^2 + g'^2}{4} Z_\mu Z^\mu \right). \tag{1.40}$$

Thus the  $W$  and  $Z$  gauge bosons acquire masses proportional to the vev of the Higgs field:

$$m_W = \frac{gv}{2}, \quad m_Z = \frac{\sqrt{g^2 + g'^2}v}{2} = \frac{m_W}{\cos \theta_W}, \tag{1.41}$$

whereas the  $A_\mu$  boson remains massless. The SM makes precise predictions for the masses  $m_W$  and  $m_Z$  of the gauge boson, the mixing angle  $\theta_W$  as well as the Higgs vev  $v$ . For example, consider the muon decay  $\mu^- \rightarrow e^- \bar{\nu}_e \nu_\mu$ . In the limit of low momentum transfer,

the  $W$  propagator can be approximated by a local four-fermion interaction which gives:

$$\frac{g^2}{8m_W^2} = \frac{G_F}{\sqrt{2}}. \quad (1.42)$$

The measured muon lifetime provides a precise determination of the constant  $G_F$ :

$$G_F = 1.16637 \times 10^{-5} \text{ GeV}^{-2}. \quad (1.43)$$

Thus from Eqs. (1.41), (1.42) and (1.43) we obtain the vev of the Higgs field which characterizes the electroweak symmetry breaking scale:

$$v = (\sqrt{2}G_F)^{-1/2} \simeq 246 \text{ GeV}. \quad (1.44)$$

(ii) The Higgs Lagrangian (1.28) has introduced a new particle in the SM known as the Higgs boson. The mass of the Higgs boson arises due to the potential term (1.29) which can be written in the unitary gauge as:

$$V(\Phi) = \lambda v^2 h^2 + \lambda v h^3 + \frac{h^4}{4}. \quad (1.45)$$

This equation suggests the mass of the Higgs boson as

$$m_H = \sqrt{2\lambda v^2} = \sqrt{-2\mu^2}. \quad (1.46)$$

Since  $\mu^2$  is not connected to any other observable quantity, the mass of the Higgs boson cannot be predicted within the SM and has to be determined experimentally. In 2012, the ATLAS and CMS collaboration discovered the Higgs boson with mass  $m_H \approx 125$  GeV [14, 15].

(iii) The fermions acquire their mass through Yukawa coupling with the Higgs doublet.

The gauge invariant Lagrangian describing this interaction has the following form:

$$\mathcal{L}_{\text{Yukawa}} = -Y_{\alpha\beta}^{(u)} \bar{Q}_{\alpha L} \tilde{\Phi} U_{\beta R} - Y_{\alpha\beta}^{(d)} \bar{Q}_{\alpha L} \Phi D_{\beta R} - Y_{\alpha\beta}^{(l)} \bar{L}_{\alpha L} \Phi E_{\beta R} + \text{h.c.}, \quad (1.47)$$

where  $\tilde{\Phi} = i\sigma_2 \Phi^*$ ,  $\alpha, \beta$  are indices summed over the quark and lepton generations, and  $Y_{\alpha\beta}^{(f)}$ ,  $f = u, d, l$  denote the Yukawa couplings of quarks and leptons with the Higgs field.

In the unitary gauge the above Lagrangian can be written as

$$\mathcal{L}_{\text{Yukawa}} = -\left(1 + \frac{h(x)}{v}\right) \left[ \bar{u}_{\alpha L} M_{\alpha\beta}^{(u)} u_{\beta R} + \bar{d}_{\alpha L} M_{\alpha\beta}^{(d)} d_{\beta R} + \bar{l}_{\alpha L} M_{\alpha\beta}^{(l)} l_{\beta R} \right] + \text{h.c.}, \quad (1.48)$$

where the quarks and lepton fields are arranged in the following array :

$$u = \begin{pmatrix} u \\ c \\ t \end{pmatrix}, \quad d = \begin{pmatrix} d \\ s \\ b \end{pmatrix}, \quad l = \begin{pmatrix} e \\ \mu \\ \tau \end{pmatrix}, \quad (1.49)$$

and

$$M_{\alpha\beta}^{(f)} = \frac{v}{\sqrt{2}} Y_{\alpha\beta}^{(f)}, \quad f = u, d, l, \quad (1.50)$$

are the complex  $3 \times 3$  mass matrices for up-type quark, down-type quark and charged leptons respectively. The above mass matrices can be diagonalized by the following bi-unitary transformation:

$$V_L^{(f)\dagger} M^{(f)} V_R^{(f)} = D^{(f)}, \quad f = u, d, l, \quad (1.51)$$

where  $V_L$  and  $V_R$  are the appropriate  $3 \times 3$  unitary matrices and  $D^{(f)}$  are the diagonal matrices:

$$D^{(u)} = \text{Diag}(m_u, m_c, m_t), \quad D^{(d)} = \text{Diag}(m_d, m_s, m_b), \quad D^{(l)} = \text{Diag}(m_e, m_\mu, m_\tau). \quad (1.52)$$

In this manner we obtain the mass terms for the quarks and charged leptons in the SM. Eq. (1.50) implies that these masses are proportional to the Higgs vev. In addition since the elements of the Yukawa coupling matrix  $Y$  and the transformation matrices  $V_L$  and  $V_R$  are unknown, the quark and lepton masses cannot be predicted. The experimental measurements of the above nine fundamental parameters of the SM reveals the following hierarchy:  $m_u \ll m_c \ll m_t, m_d \ll m_s \ll m_b, m_e \ll m_\mu \ll m_\tau$ , which has no explanation within the SM. Also notice that there are no mass terms for the neutrinos. This is due to the fact that the SM contains only left-handed neutrino fields (Eqs. (1.19) and (1.20)), which excludes the possibility of a Yukawa type coupling of neutrinos with the Higgs doublet. Thus in the SM the neutrinos remain massless.

The full Lagrangian for the Standard Electroweak Model can be written as

$$\mathcal{L} = \mathcal{L}_{\text{matter}} + \mathcal{L}_{\text{gauge}} + \mathcal{L}_{\text{Higgs}} + \mathcal{L}_{\text{Yukawa}}, \quad (1.53)$$

where the corresponding terms given by Eqs. (1.21), (1.24), (1.28) and (1.48) respectively.

## 1.2 Neutrino mass, mixing and oscillations

The existence of neutrino mass is so far the only experimental evidence for the physics beyond the SM. As discussed in the last Section, the SM is formulated in a manner such that the neutrinos have zero mass. However, there is no fundamental symmetry in the SM which forbids neutrino mass. One of the ways to generate neutrino mass is to extend the SM by adding three right-handed neutrino fields  $\nu_R = \nu_{eR}, \nu_{\mu R}, \nu_{\tau R}$ . This eliminates the inherent asymmetry in the SM between the quark and lepton sectors and is called minimally extended Standard Model (MESM). The right-handed neutrino fields are  $SU(2)_L$  singlets and have hypercharge  $Y = 0$  (see Table 1.1). Thus they have no interactions with the gauge bosons and are called *sterile*.

In the MESM the presence of right-handed neutrino fields allows us to construct a Dirac neutrino mass term which arises due to the Yukawa coupling:

$$\mathcal{L}_{\text{Dirac}} = -Y_{\alpha\beta}^{(\nu)} \bar{L}_{\alpha L} \tilde{\Phi} \nu_{\beta R} + \text{h.c.}, \quad (1.54)$$

where  $Y_{\alpha\beta}^{(\nu)}$  are the coupling constants. After the spontaneous symmetry breaking the neutrino mass term can be written as

$$\mathcal{L}_{\text{Dirac}} = -\bar{\nu}_L M_D \nu_R + \text{h.c.}, \quad (1.55)$$

where

$$M_D = \frac{v}{\sqrt{2}} Y^{(\nu)} \quad (1.56)$$

is a complex  $3 \times 3$  Dirac mass matrix, and  $\nu_L$  and  $\nu_R$  are the left- and right-handed neutrino arrays respectively:

$$\nu_L = \begin{pmatrix} \nu_{eL} \\ \nu_{\mu L} \\ \nu_{\tau L} \end{pmatrix}; \quad \nu_R = \begin{pmatrix} \nu_{eR} \\ \nu_{\mu R} \\ \nu_{\tau R} \end{pmatrix}. \quad (1.57)$$

The matrix  $M_D$  is, in general, not diagonal. To obtain masses of the physical fields,  $M^D$  needs to be diagonalized by the following bi-unitary transformation

$$U^\dagger M_D V = M_\nu = \text{diag}\{m_1, m_2, m_3\}. \quad (1.58)$$

The resulting Dirac mass term is given by

$$\mathcal{L}_{\text{Dirac}} = -\bar{\nu}'_L M_\nu \nu'_R + \text{h.c.} = \sum_{i=1}^3 m_i \bar{\nu}_i \nu_i, \quad (1.59)$$

where  $\nu'_L$  and  $\nu'_R$  are the chiral projections of the physical Dirac neutrino fields  $\nu_i$  with definite mass  $m_i$  :

$$\nu'_L = U^\dagger \nu_L = \begin{pmatrix} \nu_{1L} \\ \nu_{2L} \\ \nu_{3L} \end{pmatrix}, \quad \nu'_R = V^\dagger \nu_R = \begin{pmatrix} \nu_{1R} \\ \nu_{2R} \\ \nu_{3R} \end{pmatrix}, \quad (1.60)$$

$$\nu' = \nu'_L + \nu'_R = \begin{pmatrix} \nu_1 \\ \nu_2 \\ \nu_3 \end{pmatrix}, \quad (1.61)$$

such that  $P_L \nu' = \nu'_L$  and  $P_R \nu' = \nu'_R$ .

We have shown that in the MESM the Dirac neutrino can be generated through the usual Higgs mechanism. According to Eq. (1.56), the neutrino masses obtained in this way are proportional to Higgs vev, just like the masses of other fermions in the SM. This is expected since this model treats the neutrino fields on the same footing as the fields of the other fermions. However, the current experimental bounds on the neutrino mass (for example [16]) suggest that the neutrinos are at least five orders of magnitude lighter than the lightest fermion, the electron. Thus it is unlikely that the standard Higgs mechanism alone is responsible for the generation of neutrino mass.

The simplest way to generate small neutrino masses is provided by the *seesaw mechanism*. In this model one writes a Majorana mass term for the right-handed neutrinos which arises due to some fundamental interactions at higher energy scale. The diagonalization of the combined Dirac-Majorana Lagrangian then gives us two neutrino mass scales for the left-handed and right-handed neutrinos respectively:  $m_{\nu L} \simeq M_D^T M_R^{-1} M_D$  and  $m_{\nu R} \simeq M_R$ , where  $M_D$  and  $M_R$  correspond to Dirac and Majorana mass matrices respectively. Now as we saw above, the Dirac mass term is generated by Higgs mechanism. Thus the order of magnitude of elements of  $M^D$  is probably of the order of other fermion masses. However the Majorana mass term  $M_R$ , being an SM singlet, corresponds to some large mass scale

$\Lambda$  beyond the SM i.e.  $\Lambda \gg v$ . If we take  $\Lambda$  to be the typical grand unification scale ( $\sim 10^{14} - 10^{16}$  GeV) then the light neutrino masses, which are given by the eigenvalues of  $m_{\nu L}$ , are suppressed relative to  $M_D$  by a ratio  $v/\Lambda \sim 10^{-14} - 10^{-12}$ . In this manner one can generate small neutrino masses over several orders of magnitude by choosing different values for the elements of  $M_D$  and  $M_R$ .

### 1.2.1 Neutrino mixing

Regardless of how the small neutrino mass arises, their existence have major consequences in the low energy phenomenology. For example, the Lagrangian for the charged-current interactions of leptons with the  $W$  bosons is given by:

$$\mathcal{L}_{CC} = -\frac{g}{\sqrt{2}}\bar{\nu}_L\gamma^\mu l_L W_\mu^- + \text{h.c.} \quad (1.62)$$

We can choose a basis in which the charged lepton mass term is diagonal i.e. the mass eigenstates of charged leptons coincide with their flavor eigenstates. In this basis, using the transformation (1.60), we can write the above Lagrangian in terms of the neutrino mass eigenstates  $\nu'$ :

$$\begin{aligned} \mathcal{L}_{CC} &= -\frac{g}{\sqrt{2}}\bar{\nu}'_L U^\dagger \gamma^\mu l_L W_\mu^- + \text{h.c.} \\ &= -\frac{g}{\sqrt{2}} \begin{pmatrix} \bar{\nu}_{1L} & \bar{\nu}_{2L} & \bar{\nu}_{3L} \end{pmatrix} U^\dagger \gamma^\mu \begin{pmatrix} e_L \\ \mu_L \\ \tau_L \end{pmatrix} W_\mu^- + \text{h.c.} \\ &= -\frac{g}{\sqrt{2}} \sum_{\alpha=e,\mu,\tau} \sum_{k=1}^3 U_{\alpha k}^* \bar{\nu}_{kL} \gamma^\mu l_{\alpha L} W_\mu^- + \text{h.c.} \end{aligned} \quad (1.63)$$

The unitary matrix  $U$  is called neutrino mixing matrix or the PMNS (Pontecorvo-Maki-Nakagawa-Sakata) matrix [17, 18]. An immediate consequence of neutrino mixing is that it leads to lepton flavor violation, unless the mixing matrix is unity. For Dirac neutrinos the

total lepton number is conserved which arise as a global symmetry of the Dirac Lagrangian under the  $U(1)$  phase transformations of the lepton fields. However, the Majorana mass term is not invariant under these transformations which leads to lepton number violation in the case of massive Majorana neutrinos.

The  $3 \times 3$  unitary matrix  $U$  can be parameterized using three angles and six phases. However, three of these phases are unphysical since they can be absorbed into the phases of charged lepton fields in Eq. (1.63). For the case of Dirac neutrinos two additional phases can be eliminated by rephasing the massive neutrino fields  $\nu_{kL}$ . Thus Dirac neutrino mixing matrix is characterized, apart from the three mixing angles, by one physical phase which give rise to CP violation. For Majorana neutrinos the mass term is not invariant under rephasing of  $\nu_{kL}$  which results in three physical phases in the mixing matrix. In general, the mixing matrix  $U$  can be written as [4]:

$$U = U^D D^M, \quad (1.64)$$

where  $U^D$  is the Dirac-like mixing matrix with one Dirac phase and  $D^M$  is a diagonal matrix with two Majorana phases. Clearly for the Dirac neutrinos:  $U = U^D$ . The standard parametrization of matrix  $U^D$  is given by

$$U = \begin{pmatrix} c_{12}c_{13} & s_{12}c_{13} & s_{13}e^{-i\delta} \\ -s_{12}c_{23} - c_{12}s_{23}s_{13}e^{i\delta} & c_{12}c_{23} - s_{12}s_{23}s_{13}e^{i\delta} & s_{23}c_{13} \\ s_{12}s_{23} - c_{12}c_{23}s_{13}e^{i\delta} & -c_{12}s_{23} - s_{12}c_{23}s_{13}e^{i\delta} & c_{23}c_{13} \end{pmatrix}, \quad (1.65)$$

where  $c_{ab} \equiv \cos \theta_{ab}$  and  $s_{ab} \equiv \sin \theta_{ab}$ .  $\theta_{12}$ ,  $\theta_{13}$ , and  $\theta_{23}$  are the three mixing angles such that  $0 \leq \theta_{ab} \leq \pi/2$  and  $\delta$  is the Dirac CP violating phase,  $0 \leq \delta \leq 2\pi$ . The diagonal matrix  $D^M$  can be written as:

$$D^M = \text{Diag}\{1, e^{i\rho}, e^{i\sigma}\}, \quad (1.66)$$

where  $\rho$  and  $\sigma$  are the two Majorana phases.

## 1.2.2 Neutrino oscillations

The observation of neutrino oscillations in several different experiments is a definitive evidence of neutrino mass and flavor mixing. In a typical experiment the neutrinos are produced in a charged-current interaction together with a charged antilepton. According to Eq. (1.63) a neutrino with flavor  $\nu_\alpha$ ,  $\alpha = e, \mu, \tau$  is produced in a superposition of physical fields  $\nu_k$  with different masses  $m_k$ . Thus we can write:

$$|\nu_\alpha\rangle = \sum_k U_{\alpha k}^* |\nu_k\rangle, \quad (1.67)$$

where  $|\nu_k\rangle$  are the eigenstates of the neutrino propagation Hamiltonian with energy eigenvalues  $E_k = \sqrt{p_k^2 + m_k^2}$  and are called mass eigenstates. As the neutrinos propagate, the eigenstates  $|\nu_k\rangle$  evolve differently due to different energy eigenvalues  $E_k$ . This leads to transitions among the different flavor eigenstates  $|\nu_\alpha\rangle$  which are termed as neutrino oscillations. If the neutrinos are initially produced in a flavor  $\nu_\alpha$  then after traveling a distance  $L$  the probability for the transition  $\nu_\alpha \rightarrow \nu_\beta$  is given by Eq. (A.6) in Appendix A:

$$\begin{aligned} \mathcal{P}_{\nu_\alpha \rightarrow \nu_\beta}(L, E) &= \sum_{j,k} U_{\alpha k}^* U_{\beta k} U_{\alpha j} U_{\beta j}^* \exp\left(-i \frac{\Delta m_{kj}^2 L}{2E}\right) \\ &= \delta_{\alpha\beta} - 2\text{Re} \sum_{k>j} U_{\alpha k}^* U_{\beta k} U_{\alpha j} U_{\beta j}^* \exp\left(-i \frac{\Delta m_{kj}^2 L}{2E}\right), \end{aligned} \quad (1.68)$$

where  $\Delta m_{kj}^2 = m_k^2 - m_j^2$ , and  $E$  is the neutrino energy. The unitarity of the mixing matrix  $U$  gives us the relation:

$$\sum_k U_{\alpha k} U_{\beta k}^* = \delta_{\alpha\beta} \quad (1.69)$$

$$\Rightarrow \sum |U_{\alpha k}|^2 |U_{\beta k}|^2 = \delta_{\alpha\beta} - 2 \sum_{k>j} \text{Re}(U_{\alpha k}^* U_{\beta k} U_{\alpha j} U_{\beta j}^*). \quad (1.70)$$

Thus we can write the Eq. (1.68) in a useful form:

$$\begin{aligned} \mathcal{P}_{\nu_\alpha \rightarrow \nu_\beta}(L, E) = & \delta_{\alpha\beta} - 4 \sum_{k>j} \text{Re}(U_{\alpha k}^* U_{\beta k} U_{\alpha j} U_{\beta j}^*) \sin^2 \left( \frac{\Delta m_{kj}^2 L}{4E} \right) \\ & + 2 \sum_{k>j} \text{Im}(U_{\alpha k}^* U_{\beta k} U_{\alpha j} U_{\beta j}^*) \sin \left( \frac{\Delta m_{kj}^2 L}{2E} \right). \end{aligned} \quad (1.71)$$

For the channel  $\alpha = \beta$ , Eq. (1.71) gives us the survival probability

$$\mathcal{P}_{\nu_\alpha \rightarrow \nu_\alpha}(L, E) = 1 - 4 \sum_{k>j} \text{Re}(|U_{\alpha k}|^2 |U_{\beta k}|^2) \sin^2 \left( \frac{\Delta m_{kj}^2 L}{4E} \right). \quad (1.72)$$

Let us now consider the case of antineutrinos which are produced through the Hermitian conjugate part of the charged-current interaction (1.63). The antineutrino states are thus described by the relation

$$|\bar{\nu}_\alpha\rangle = \sum_k U_{\alpha k} |\nu_k\rangle. \quad (1.73)$$

The oscillation probability for the antineutrino transitions  $\bar{\nu}_\alpha \rightarrow \bar{\nu}_\beta$  is obtained by the replacement  $U \rightarrow U^*$  in Eq. (1.71):

$$\begin{aligned} \mathcal{P}_{\bar{\nu}_\alpha \rightarrow \bar{\nu}_\beta}(L, E) = & \delta_{\alpha\beta} - 4 \sum_{k>j} \text{Re}(U_{\alpha k}^* U_{\beta k} U_{\alpha j} U_{\beta j}^*) \sin^2 \left( \frac{\Delta m_{kj}^2 L}{4E} \right) \\ & - 2 \sum_{k>j} \text{Im}(U_{\alpha k}^* U_{\beta k} U_{\alpha j} U_{\beta j}^*) \sin \left( \frac{\Delta m_{kj}^2 L}{2E} \right). \end{aligned} \quad (1.74)$$

The difference in the oscillation probabilities of the neutrinos and antineutrinos indicate CP violation, which can be expressed by

$$\Delta\mathcal{P} = \mathcal{P}_{\nu_\alpha \rightarrow \nu_\beta} - \mathcal{P}_{\bar{\nu}_\alpha \rightarrow \bar{\nu}_\beta} = 4 \sum_{k>j} \text{Im}(U_{\alpha k}^* U_{\beta k} U_{\alpha j} U_{\beta j}^*) \sin \left( \frac{\Delta m_{kj}^2 L}{2E} \right). \quad (1.75)$$

Thus CP violation requires imaginary terms in the mixing matrix. If CP is violated then T is violated by the same amount to keep the CPT conserved. Thus  $\Delta\mathcal{P} = \mathcal{P}_{\nu_\alpha \rightarrow \nu_\beta} - \mathcal{P}_{\nu_\beta \rightarrow \nu_\alpha}$ .

Also if  $\alpha = \beta$ , then

$$\Delta\mathcal{P} = 4 \sum_{k>j} \text{Im}(|U_{\alpha k}|^2 |U_{\beta k}|^2) \sin\left(\frac{\Delta m_{kj}^2 L}{2E}\right) = 0. \quad (1.76)$$

Thus to observe CP violation one needs to measure transition probability between two different flavor states.

The special case of two-neutrino mixing provides a useful approximation to study several important properties of the neutrino oscillation phenomenon [19]. In this case the two flavor states  $\nu_\alpha$  and  $\nu_\beta$  are linear superposition of two mass eigenstates  $\nu_1$  and  $\nu_2$ . The  $2 \times 2$  mixing matrix can be written as

$$U = \begin{pmatrix} \cos\theta & \sin\theta \\ -\sin\theta & \cos\theta \end{pmatrix}, \quad (1.77)$$

where  $\theta$  is the mixing angle. From Eq. (1.72) the survival probability is given by

$$\mathcal{P}_{\nu_\alpha \rightarrow \nu_\alpha}(L, E) = 1 - \sin^2 2\theta \sin^2\left(\frac{\Delta m^2 L}{4E}\right), \quad (1.78)$$

where  $\Delta m^2 = \Delta m_{21}^2$ . The last term indicates oscillations between the flavor states with a wavelength

$$L_{\text{osc}} = \frac{4\pi E}{\Delta m^2}. \quad (1.79)$$

The oscillation wavelength is the scale over which the quantum interference between massive neutrino states take place. However, there are several ways through which the coherence of massive neutrinos is lost and the interference effects are not observed (see Appendix A). In this case the oscillating term in Eq. (1.78) averages out and we obtain the incoherent survival probability

$$\langle \mathcal{P}_{\nu_\alpha \rightarrow \nu_\alpha} \rangle = 1 - \frac{1}{2} \sin^2 2\theta. \quad (1.80)$$

Parameter	NO Best fit $\pm 1\sigma$	IO Best fit $\pm 1\sigma$
$\theta_{12}(\circ)$	$33.56^{+0.77}_{-0.75}$	$33.56^{+0.77}_{-0.75}$
$\theta_{23}(\circ)$	$41.6^{+1.5}_{-1.2}$	$50.0^{+1.1}_{-1.4}$
$\theta_{13}(\circ)$	$8.46^{+0.15}_{-0.15}$	$8.49^{+0.15}_{-0.15}$
$\delta_{CP}(\circ)$	$261^{+51}_{-59}$	$277^{+40}_{-46}$
$\Delta m_{21}^2/10^{-5} \text{ eV}^2$	$7.50^{+0.19}_{-0.17}$	$7.50^{+0.19}_{-0.17}$
$\Delta m_{3l}^2/10^{-3} \text{ eV}^2$	$2.524^{+0.039}_{-0.040}$	$-2.514^{+0.038}_{-0.041}$

Table 1.2: Best fit values of the neutrino oscillation parameters for normal ordering (NO) and inverted ordering (IO) obtained by global analysis of the neutrino oscillation data, as presented in Ref. [20].  $\Delta m_{3l}^2 \equiv \Delta m_{31}^2 > 0$  for NO and  $\Delta m_{3l}^2 \equiv \Delta m_{32}^2 < 0$  for IO.

The results from solar, atmospheric, reactor and accelerator neutrino experiments have convincingly shown that the neutrinos are mixed and massive particles. The parameters of the three neutrino mixing (1.65) have been obtained by various groups through the global analysis of the neutrino oscillation data. In Table 1.2 we show the best-fit values of the neutrino oscillation parameters as reported in Ref. [20].

### 1.2.3 Neutrino oscillations in matter

It was shown by Wolfenstein [21] that the propagation of neutrinos through matter induces an effective potential due to coherent forward scattering of neutrinos off the background matter particles. Since the background matter at ordinary temperatures does not contain muons or taus, the electron neutrinos  $\nu_e$  encounter both charged-current and neutral-current interactions while  $\nu_\mu$  and  $\nu_\tau$  undergo only neutral-current interactions (Fig. 1.1). Thus the effective potential is flavor dependent which results in a modification in the neutrino mass and mixing in matter. This leads to significant changes in the neutrino oscillation probability in the medium.

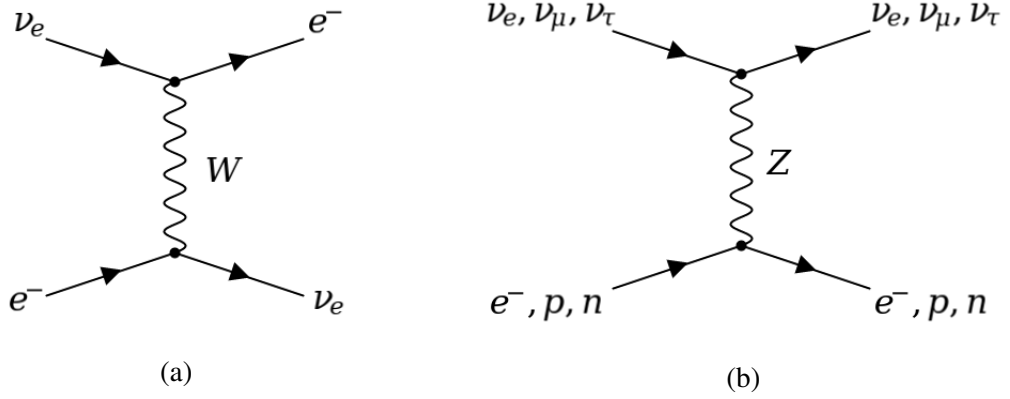


Figure 1.1: Tree-level Feynman diagrams of the elastic scattering of neutrinos with the background matter particles, which generate (a) charged-current potential  $V_{CC}$  and (b) neutral-current potential  $V_{NC}$ .

Consider first the elastic  $\nu_e e^-$  scattering through charged-current interaction (Fig. 1.1a).

The effective low energy Hamiltonian for this process is given by

$$\begin{aligned} \mathcal{H}_{\text{eff}}^{\text{CC}} &= \frac{G_F}{\sqrt{2}} [\bar{e}(p_1)\gamma_\lambda(1 - \gamma^5)\nu_e(p_2)] [\bar{\nu}_e(p_3)\gamma^\lambda(1 - \gamma^5)e(p_4)] \\ &= \frac{G_F}{\sqrt{2}} [\bar{\nu}_e(p_3)\gamma_\lambda(1 - \gamma^5)\nu_e(p_2)] [\bar{e}(p_1)\gamma^\lambda(1 - \gamma^5)e(p_4)], \end{aligned} \quad (1.81)$$

where we have used Fierz transformation in the last term. For the elastic forward scattering of neutrinos off the electrons, the neutrino momentum remains unchanged i.e.  $p_2 = p_3 = p$ , which results in the effective Hamiltonian

$$\mathcal{H}_{\text{eff}}^{\text{CC}} = \sqrt{2}G_F\bar{\nu}_{eL}\gamma_\lambda\nu_{eL}\langle\bar{e}\gamma^\lambda(1 - \gamma^5)e\rangle. \quad (1.82)$$

In normal unpolarized matter at rest, averaging over electron background results in [19]:

$$\langle\bar{e}\gamma^\lambda(1 - \gamma^5)e\rangle = \delta^{\lambda 0}\langle\bar{e}\gamma_0 e\rangle = \delta^{\lambda 0}n_e, \quad (1.83)$$

where  $n_e$  is the number density of electrons in the medium. Thus (1.82) becomes

$$\mathcal{H}_{\text{eff}}^{\text{CC}} = \sqrt{2}G_F n_e \bar{\nu}_{eL} \gamma_0 \nu_{eL} = V_{CC} \bar{\nu}_{eL} \gamma_0 \nu_{eL}, \quad (1.84)$$

where the charged-current potential is given by

$$V_{\text{CC}} = \sqrt{2}G_F n_e. \quad (1.85)$$

In a similar manner one can find out the effective neutral-current potential in matter which is same for neutrinos of all the flavors [22]:

$$V_{\text{NC}} = -\frac{1}{2}\sqrt{2}G_F n_n, \quad (1.86)$$

where  $n_n$  is the number density of neutrons in the medium. Thus the effective potential for a neutrino of flavor  $\alpha$  in an unpolarized medium can be written as

$$V_\alpha = V_{\text{CC}}\delta_{\alpha e} + V_{\text{NC}} = \sqrt{2}G_F \left( n_e \delta_{\alpha e} - \frac{n_n}{2} \right). \quad (1.87)$$

Consider now the case of two-neutrino mixing in a medium. The evolution equation for the propagation of ultrarelativistic neutrinos in matter is given by

$$i \frac{d}{dx} \begin{pmatrix} \nu_e \\ \nu_\mu \end{pmatrix} = H_m \begin{pmatrix} \nu_e \\ \nu_\mu \end{pmatrix}, \quad (1.88)$$

where Hamiltonian  $H_m$  in matter is the sum of vacuum Hamiltonian and the interaction Hamiltonian. In the flavor basis  $H_m$  is given by

$$H_m = U \begin{pmatrix} -\Delta m^2/4E & 0 \\ 0 & \Delta m^2/4E \end{pmatrix} U^\dagger + \begin{pmatrix} V_{\text{CC}} + V_{\text{NC}} & 0 \\ 0 & V_{\text{NC}} \end{pmatrix}, \quad (1.89)$$

where  $U$  is the mixing matrix (1.77). Neglecting the terms proportional to identity matrix, we obtain

$$H_m = \frac{1}{4E} \begin{pmatrix} -\Delta m^2 \cos 2\theta + A & \Delta m^2 \sin 2\theta \\ \Delta m^2 \sin 2\theta & -\Delta m^2 \cos 2\theta - A \end{pmatrix}, \quad (1.90)$$

where  $A = 2EV_{CC} = 2\sqrt{2}G_F n_e E$ . In a medium with constant density the above Hamiltonian can be diagonalized by the following transformation to the mass basis in matter:

$$U_m^\dagger H_m U_m = \text{Diag}\left(-\Delta m_m^2/4E, \Delta m_m^2/4E\right), \quad (1.91)$$

where

$$U_m = \begin{pmatrix} \cos \theta_m & \sin \theta_m \\ -\sin \theta_m & \cos \theta_m \end{pmatrix}, \quad (1.92)$$

is the unitary mixing matrix in matter. The mixing angle and mass-squared difference in matter are given by

$$\cos 2\theta_m = \frac{\Delta m^2 \cos 2\theta - A}{\sqrt{(\Delta m^2 \cos 2\theta - A)^2 + (\Delta m^2 \sin 2\theta)^2}}, \quad (1.93)$$

$$\Delta m_m^2 = \sqrt{(\Delta m^2 \cos 2\theta - A)^2 + (\Delta m^2 \sin 2\theta)^2}. \quad (1.94)$$

The oscillation probabilities in matter are thus given by

$$\mathcal{P}_m(\nu_e \rightarrow \nu_e) = 1 - \sin^2 2\theta_m \sin^2 \left( \frac{\Delta m_m^2 L}{4E} \right), \quad (1.95)$$

which is the same as Eq. (1.78) with modification  $\theta \rightarrow \theta_m$  and  $\Delta m^2 \rightarrow \Delta m_m^2$ . Thus the neutrino propagation in matter leads to changes in their oscillation probabilities compared to the vacuum values. However, in this case a new feature arises which can lead to enhancement in neutrino transitions in a medium. This can be seen from Eq. (1.93) according to which the mixing angle becomes maximum when

$$A = \Delta m^2 \cos 2\theta. \quad (1.96)$$

This condition is called resonance and corresponds to the electron number density

$$n_e^R = \frac{\Delta m^2 \cos 2\theta}{2\sqrt{2}G_F E}. \quad (1.97)$$

At resonance the mixing angle becomes  $\pi/4$  and there is a possibility of complete conversion of original neutrino beam to a different flavor.

The presence of resonance can have important consequences for neutrino propagation in a medium with varying density. In such a medium the neutrino mass eigenstates are no longer the eigenstates of the Hamiltonian (1.90). Thus the Hamiltonian is not diagonal in the mass basis. In this case the transformation to the mass basis

$$\begin{pmatrix} \nu_e \\ \nu_\mu \end{pmatrix} = U_m \begin{pmatrix} \nu_{1m} \\ \nu_{2m} \end{pmatrix} \quad (1.98)$$

yields the evolution equation

$$\begin{aligned} i \frac{d}{dx} \begin{pmatrix} \nu_{1m} \\ \nu_{2m} \end{pmatrix} &= \left( U_m^\dagger H_m U_m - i U_m^\dagger \frac{dU_m}{dx} \right) \begin{pmatrix} \nu_{1m} \\ \nu_{2m} \end{pmatrix} \\ &= \begin{pmatrix} -\Delta m_m^2/4E & -i d\theta_m/dx \\ i d\theta_m/dx & \Delta m_m^2/4E \end{pmatrix} \begin{pmatrix} \nu_{1m} \\ \nu_{2m} \end{pmatrix} \end{aligned} \quad (1.99)$$

Let the density of the medium is a slowly varying function of distance  $x$  so that  $d\theta_m/dx$  is small. In particular we assume

$$\left| \frac{d\theta_m}{dx} \right| \ll \left| \frac{\Delta m_m^2}{2E} \right|, \quad (1.100)$$

which corresponds to the case where transitions between  $\nu_{1m}$  and  $\nu_{2m}$  are negligible. This is called adiabatic approximation. Under this approximation Eq. (1.99) can be integrated to give the  $\nu_e$  survival probability [19]

$$\mathcal{P}_m^{\text{adia}}(\nu_e \rightarrow \nu_e) = \frac{1}{2} (1 + \cos 2\theta \cos 2\theta_m). \quad (1.101)$$

The adiabatic propagation of neutrinos in a medium with varying density can lead to resonant transitions which is known as MSW (Mikheyev-Smirnov-Wolfenstein) effect [23,24].

The essence of this effect can be seen by considering an electron neutrino produced at the center of the Sun or in a star where the density is infinitely high. Then Eq. (1.93) implies mixing angle at this point is  $\theta_m \approx \pi/2$ , and Eq. (1.98) implies that  $\nu_e$  corresponds to the mass eigenstate  $\nu_{2m}$ . As the neutrinos move outward to regions of smaller density, it will pass through resonance region where Eq. (1.97) is satisfied and finally proceed to vacuum where the angle  $\theta_m$  is equal to the vacuum mixing angle. If the propagation is adiabatic the neutrinos will remain in the mass eigenstate  $\nu_{2m}$ , which at a point in vacuum is given by  $\nu_2 = \nu_e \sin \theta + \nu_\mu \cos \theta$ . Thus the probability of finding  $\nu_e$  decreases from one to the value  $\sin^2 \theta$ . This can have dramatic consequences if the angle  $\theta$  is small, in which case we obtain large flavor conversion in spite of a small mixing angle.

### 1.3 Overview of the thesis

In this Chapter we presented some of the well-known features of the Standard Model. We also discussed the phenomenon of neutrino oscillations which arises due to non-zero neutrino mass. Theory and experiments of neutrino oscillations have a rich history [25–27] and it continues to play an important role in the efforts to discover new physics beyond the SM. On the experimental front several experiments are in progress and are planned with different neutrino sources. Some of the important recent measurements include constraints on the neutrino CP violating phase at T2K [28], measurement of reactor antineutrino spectra at Daya Bay [29] and the measurement of neutrino produced in the CNO cycle in the Sun at Borexino [30]. On the theoretical side several studies have been carried out to understand the intricacies and implications of the neutrino oscillation phenomenon.

In this Thesis, we study the phenomenological aspects of neutrino flavor and spin-flavor oscillations, and point out several new features and observables that can give important insights about the phenomenon of neutrino oscillations. In Chapter 2 we study the electromagnetic character of neutrinos. This Chapter contains detailed discussions on neutrino

dipole moment: its origin, its experimental and theoretical limits and its implications for neutrino propagation in magnetic fields. This Chapter lays the foundation for the next two Chapters in which we study the phenomenon of neutrino spin-flavor oscillations in the astrophysical environments where they may generate novel and hopefully observable effects. In Chapter 3 we examine the effects of the solar magnetic fields on the electron neutrinos produced in the Sun. We evaluate neutrino spin-flavor transition probabilities and use bounds from the Borexino experiment to constrain the solar magnetic fields. In Chapter 4 we explore the quantum mechanical features of neutrino spin rotation and point to emergence of geometric phases in this phenomenon. We derive analytical expressions for adiabatic and non-adiabatic geometric phases for neutrino propagation in different environments such as the Sun and neutron stars and discuss their phenomenological implications. In Chapter 5 we study the geometric interpretation of neutrino flavor oscillations and derive mixed state geometric phase which arises during evolution of a neutrino beam. We show that our results are generalizations of the earlier results by various authors for both two and three flavor neutrino oscillations. Finally in Chapter 6 we summarize our results and present a future outlook.



---

**Electromagnetic properties of neutrinos**

---

The study of neutrino electromagnetic properties and interactions not only gives us important insights into various phenomena beyond the SM, this can also be used as a tool to distinguish between the Dirac and Majorana nature of neutrinos. In this Chapter we give a concise review of the neutrino electromagnetic properties such as origin of neutrino dipole moment (NDM), neutrino interactions with the electromagnetic fields and spin-flavor transitions in neutral matter and in magnetic fields. Some of the review articles and books which contain an extensive discussion of neutrino electromagnetic properties and related phenomenology can be found in Refs. [1, 2, 6, 31, 32].

## **2.1 Electromagnetic form factors**

Neutrinos, being electrically neutral particles, acquire their electromagnetic properties through interactions with a photon at quantum loop level. The coupling of the neutrino

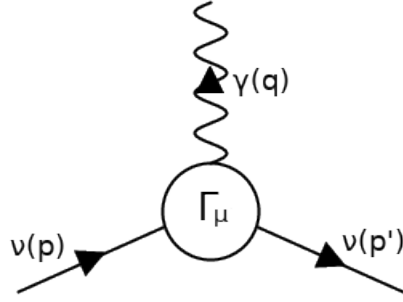


Figure 2.1: Effective vertex for neutrino-photon interaction.

field  $\nu(x)$  with the electromagnetic field  $A^\mu(x)$  in one-photon approximation can be described by an effective interaction Hamiltonian [31]

$$\mathcal{H}_{\text{em}}(x) = j_\mu(x)A^\mu(x) = \bar{\nu}(x)\Gamma_\mu\nu(x)A^\mu(x), \quad (2.1)$$

where  $j^\mu$  is the neutrino electromagnetic current density and  $\Gamma_\mu$  is the vertex function. For a given Lagrangian the vertex function is obtained by summing over all possible Feynman diagrams having the form shown in Fig. 2.1. For the diagram in Fig 2.1, the matrix elements of current  $j^\mu(x)$  are given by

$$\langle\nu(p')|j_\mu(x)|\nu(p)\rangle = \langle\nu(p')|e^{i\mathcal{P}\cdot x}j_\mu(0)e^{-i\mathcal{P}\cdot x}|\nu(p)\rangle = e^{-iq\cdot x}\langle\nu(p')|j_\mu(0)|\nu(p)\rangle, \quad (2.2)$$

where  $\mathcal{P}_\mu$  is the four-momentum operator,  $p$  and  $p'$  are the four momentum of initial and final neutrino states respectively, and  $q = p - p'$  is the four momentum of the photon. The evaluation of the matrix element in Eq. (2.2) depends on Dirac or Majorana nature of the neutrino, which gives rise to different form factor in both cases.

### 2.1.1 Dirac neutrinos

First we consider the case in which the neutrinos in Fig. 2.1 are described by free Dirac fields having the plane wave expansion

$$\psi(x) = \int \frac{d^3p}{(2\pi)^3 2E} \sum_{h=\pm 1} \left[ a(p, h) u(p, h) e^{-ip \cdot x} + b^\dagger(p, h) v(p, h) e^{ip \cdot x} \right], \quad (2.3)$$

where  $h$  is helicity,  $E$  is neutrino energy,  $u(p, h)$  and  $v(p, h)$  are positive and negative energy spinors. The particle and antiparticle annihilation operators  $a(p, h)$  and  $b(p, h)$  obey the following anti-commutation relation:

$$\{a(p, h), a^\dagger(p', h')\} = \{b(p, h), b^\dagger(p', h')\} = (2\pi)^3 2E \delta^3(\vec{p} - \vec{p}') \delta_{hh'}. \quad (2.4)$$

In this case the matrix element (2.2) is given by

$$\langle \nu(p') | j_\mu(x) | \nu(p) \rangle = e^{-iq \cdot x} \bar{u}(p') \Gamma_\mu(p, p') u(p), \quad (2.5)$$

where we have suppressed the helicity labels. Since  $(p + p')^2 = 4m^2 - q^2$ ,  $m$  being the neutrino mass, all possible terms in  $\Gamma_\mu(p, p')$  can be written in terms of  $q^2$ , which is the only independent kinematical quantity. Thus the vertex function  $\Gamma_\mu(p, p')$  can be decomposed in terms of Lorentz invariant form factors which depend only on  $q^2$ . The explicit form of the vertex function can be constrained by following two requirements:

(i) The conservation of the current  $j^\mu(x)$ , required by the gauge invariance of  $\mathcal{H}_{\text{em}}(x)$  in Eq. (2.1) under the transformation  $A^\mu \rightarrow A^\mu + \partial^\mu \phi(x)$ , implies  $\partial_\mu j^\mu(x) = 0$ . Using Eq. (2.5) we obtain

$$q^\mu \bar{u}(p') \Gamma_\mu(q) u(p) = 0. \quad (2.6)$$

(ii) The Hermiticity of the Hamiltonian in Eq. (2.1) requires that the current  $j_\mu$  must be Hermitian. Since

$$\langle \nu(p') | j_\mu(x) | \nu(p) \rangle^\dagger = e^{iq \cdot x} \left( \bar{u}(p') \Gamma_\mu(q) u(p) \right)^\dagger = e^{-iq \cdot x} \bar{u}(p') \gamma_0 \Gamma_\mu(-q)^\dagger \gamma_0 u(p), \quad (2.7)$$

we have

$$\Gamma_\mu(q) = \gamma_0 \Gamma_\mu(-q)^\dagger \gamma_0. \quad (2.8)$$

On the basis of above considerations we can write down the vertex function in terms of four independent form factors [2, 31, 33]:

$$\Gamma_\mu(q) = \mathbb{f}_Q(q^2) \gamma_\mu - i \mathbb{f}_M(q^2) \sigma_{\mu\nu} q^\nu + \mathbb{f}_E(q^2) \sigma_{\mu\nu} q^\nu \gamma_5 + \mathbb{f}_A(q^2) (q^2 \gamma_\mu - q_\mu \not{q}) \gamma_5, \quad (2.9)$$

where  $\mathbb{f}_Q(q^2)$ ,  $\mathbb{f}_M(q^2)$ ,  $\mathbb{f}_E(q^2)$  and  $\mathbb{f}_A(q^2)$  are the charge, magnetic dipole, electric dipole and anapole form factors respectively.

The physical interpretation of the form factors can be understood by taking the non-relativistic limit of the Hamiltonian in (2.1). For example, for the second term we obtain [33, 34]

$$\mathcal{H}_{\text{em}}^{\text{NR}}(\mathbb{f}_M) = -\mathbb{f}_M(0) \boldsymbol{\sigma} \cdot \mathbf{B}, \quad (2.10)$$

where  $\mathbf{B}$  is the magnetic field and  $\boldsymbol{\sigma}$  are Pauli matrices. Thus  $\mathbb{f}_M(0)$  represents the magnetic moment  $\mu$  of the neutrino. Similarly for other terms the non-relativistic limit gives us following form factors:

$$\mathbb{f}_Q(0) = \mathfrak{q}, \quad \mathbb{f}_E(0) = \epsilon, \quad \mathbb{f}_A(0) = \mathfrak{a}, \quad (2.11)$$

where  $\mathfrak{q}$ ,  $\epsilon$  and  $\mathfrak{a}$  are neutrino charge, electric dipole moment and anapole moment respectively.

Let us now study the CP properties of the Hamiltonian (2.1). The term  $\Gamma_\mu$  in Eq. (2.1)

arises from loop diagram involving weak interactions which maximally violate  $C$  and  $P$  individually. However the violation of CP has so far been observed only in the quark sector. Now the electromagnetic field transforms as  $A_\mu \xrightarrow{CP} -A_\mu$ . Thus for  $H_{\text{em}}$  to remain CP invariant we must have

$$j_\mu \xrightarrow{CP} -j_\mu \Rightarrow \Gamma_\mu(q) \xrightarrow{CP} -\Gamma_\mu(q). \quad (2.12)$$

Using the expansion (2.9) we obtain [31]:

$$\Gamma_\mu(q) \xrightarrow{CP} -(\mathbb{f}_Q(q^2)\gamma_\mu - i\mathbb{f}_M(q^2)\sigma_{\mu\nu}q^\nu - \mathbb{f}_E(q^2)\sigma_{\mu\nu}q^\nu\gamma_5 + \mathbb{f}_A(q^2)(q^2\gamma_\mu - q_\mu\not{q})\gamma_5). \quad (2.13)$$

Thus only the  $\mathbb{f}_E(q^2)$  term violates CP. Hence in a CP conserving case this term would vanish (i.e.  $\mathbb{f}_E(q^2) = 0$ ). However, in a general scenario including leptonic CP violation Dirac neutrinos have four finite form factors.

## 2.1.2 Majorana neutrinos

A massive Dirac neutrino can have four distinct states corresponding to two helicities of both, particles and antiparticles. For Majorana neutrinos, however, only two distinct states are possible since in this case the particle and antiparticle states are identical [35]. This reduction in the degree of freedom gives rise to special CP and electromagnetic properties of the Majorana neutrinos. The Majorana field is equal to its charge conjugate field  $\psi^c = \gamma_0\mathcal{C}\bar{\psi}^*$ , where  $\mathcal{C}$  is the charge conjugation operator, upto a global phase. Thus we can write

$$\bar{\psi}\Gamma_\mu\psi = \bar{\psi}^c\Gamma_\mu\psi^c = \psi^T\mathcal{C}^{-1}\Gamma_\mu\gamma_0\mathcal{C}\bar{\psi}^* = -\psi^\dagger(C^{-1}\Gamma_\mu\gamma_0\mathcal{C})^T\psi = \bar{\psi}\mathcal{C}\Gamma_\mu^T\mathcal{C}^{-1}\psi, \quad (2.14)$$

where we have used the identity  $\psi^T \Gamma_\mu \psi' = -\psi'^T \Gamma_\mu^T \psi$ . We thus arrive at the following identity for Majorana neutrinos

$$\Gamma_\mu = \mathcal{C} \Gamma_\mu^T \mathcal{C}^{-1}. \quad (2.15)$$

Now using the expansion (2.9) for  $\Gamma_\mu$  and using the following charge conjugation properties of gamma matrices:

$$\mathcal{C} \gamma_\mu^T \mathcal{C}^{-1} = -\gamma_\mu, \quad \mathcal{C} \sigma_{\mu\nu}^T \mathcal{C}^{-1} = -\sigma_{\mu\nu}, \quad \mathcal{C} (\sigma_{\mu\nu} \gamma_5)^T \mathcal{C}^{-1} = -\sigma_{\mu\nu} \gamma_5, \quad \mathcal{C} (\gamma_\mu \gamma_5)^T \mathcal{C}^{-1} = \gamma_\mu \gamma_5, \quad (2.16)$$

we obtain

$$\Gamma_\mu = -\mathbb{f}_Q(q^2) \gamma_\mu + i \mathbb{f}_M(q^2) \sigma_{\mu\nu} q^\nu - \mathbb{f}_E(q^2) \sigma_{\mu\nu} q^\nu \gamma_5 + \mathbb{f}_A(q^2) (q^2 \gamma_\mu - q_\mu \not{q}) \gamma_5. \quad (2.17)$$

Comparing Eqs. (2.9) and (2.17) we get

$$\mathbb{f}_Q(q^2) = \mathbb{f}_M(q^2) = \mathbb{f}_E(q^2) = 0. \quad (2.18)$$

Thus in comparison to the Dirac case in which we all the form factors are non vanishing, Majorana neutrino have only nonzero anapole form factor.

So far we have considered only one massive neutrino field. But due to the phenomenon of neutrino mixing we know that there must exist at least three neutrino mass eigenstates. Thus the definition (2.5) of the neutrino electromagnetic current must be generalized to calculate the matrix elements between two different neutrino states in the following manner:

$$\langle \nu_k(p') | j_\mu(x) | \nu_j(p) \rangle = e^{-iq \cdot x} \bar{u}_k(p') \Gamma_\mu^{kj}(q) u_j(p), \quad (2.19)$$

where  $q = p - p'$  and the  $k$ th neutrino state has mass  $m_k$ . Just like the earlier case, the vertex function  $\Gamma_\mu$  can now be decomposed into Lorentz invariant form factors

$$\Gamma_\mu^{kj}(q) = (\mathbb{f}_Q^{kj}(q^2) + \mathbb{f}_A^{kj}(q^2)q^2\gamma_5)(\gamma_\mu - q_\mu\not{q}/q^2) - i\mathbb{f}_M^{kj}(q^2)\sigma_{\mu\nu}q^\nu + \mathbb{f}_E^{kj}(q^2)\sigma_{\mu\nu}q^\nu\gamma_5. \quad (2.20)$$

Thus the four form factors now become Hermitian matrices which consists of *diagonal* ( $k = j$ ) and *off-diagonal* or *transition* form factors ( $k \neq j$ ).

Considering now the CP properties of the vertex function (2.20), we find that for the Dirac case CP conservation implies that the form factor matrices  $\mathbb{f}_Q$ ,  $\mathbb{f}_M$ ,  $\mathbb{f}_A$  are real and symmetric, while the matrix  $\mathbb{f}_E$  is purely imaginary and anti-symmetric. Thus we have for

$$\text{Dirac Neutrinos} \quad \begin{cases} \mathbb{f}_\Omega^{kj} = \mathbb{f}_\Omega^{jk} = (\mathbb{f}_\Omega^{kj})^* & (\Omega = Q, M, A) \\ \mathbb{f}_E^{kj} = -\mathbb{f}_E^{jk} = -(\mathbb{f}_E^{kj})^*. \end{cases} \quad (2.21)$$

The evaluation of Eq. (2.19) for Majorana neutrinos leads to an expression for the vertex function similar to Eq. (2.20) [31]. Now Eqs. (2.14) and (2.15) are defined only if both the incoming and outgoing neutrinos in Fig. 2.1 are in same mass eigenstate. Thus Eq. (2.18) holds only for the *diagonal* case. This implies that the the Majorana neutrinos can have non-vanishing *off-diagonal* terms in the form factor matrices  $\mathbb{f}_Q$ ,  $\mathbb{f}_M$  and  $\mathbb{f}_E$ , which leads to the following properties for

$$\text{Majorana Neutrinos} \quad \begin{cases} \mathbb{f}_\Omega^{kj} = -\mathbb{f}_\Omega^{jk} = -(\mathbb{f}_\Omega^{kj})^* & (\Omega = Q, M, E) \\ \mathbb{f}_A^{kj} = \mathbb{f}_A^{jk} = (\mathbb{f}_A^{kj})^*. \end{cases} \quad (2.22)$$

Now the CP conservation in the case of Majorana neutrinos allows the existence of either a transition electric form factor or a transition magnetic form factor, but not both simultaneously [31]. Since in the following Sections we will be concerned mostly with the magnetic and electric dipole moments, we conclude this Section with the statement that Dirac neutrinos can have both diagonal and transition dipole moments while Majorana neutrinos

have only transition dipole moments.

## 2.2 Neutrino dipole moments (NDM)

The possible existence of neutrino electric and magnetic dipole moments gives rise to a number of new phenomena beyond the SM physics. From theoretical point of view the neutrino dipole moments are closely related to their masses and CP properties and thus they may play an important role in distinguishing the Dirac or Majorana nature of neutrinos. The experimental searches for NDM's with different neutrino sources have also played an important role in placing upper limits on several electromagnetic quantities such as neutrino magnetic moment (NMM), millicharge and charge radius [32]. In this Section we first give a brief review of the predictions of NDM's for Dirac and Majorana neutrinos in beyond SM theories. Then we present some upper limits of the NMM that have been obtained in several different experiments.

### 2.2.1 Theoretical predictions in MESM

In the MESM including three right-handed Dirac neutrinos, the electromagnetic vertex (2.20) is given by the sum of one-loop diagrams shown in Fig. 2.2. The calculation of the vertex function yields the following values for the magnetic and electric dipole moments of Dirac neutrinos [1, 2, 36]:

$$\begin{aligned}\mu_{kj}^D &\simeq \frac{3eG_F}{16\sqrt{2}\pi^2}(m_k + m_j) \left( \delta_{kj} - \frac{1}{2} \sum_{\alpha=e,\mu,\tau} U_{\alpha k}^* U_{\alpha j} \left( \frac{m_\alpha}{m_W} \right)^2 \right), \\ i\epsilon_{kj}^D &\simeq \frac{3eG_F}{16\sqrt{2}\pi^2}(m_k - m_j) \left( \delta_{kj} - \frac{1}{2} \sum_{\alpha=e,\mu,\tau} U_{\alpha k}^* U_{\alpha j} \left( \frac{m_\alpha}{m_W} \right)^2 \right).\end{aligned}\quad (2.23)$$

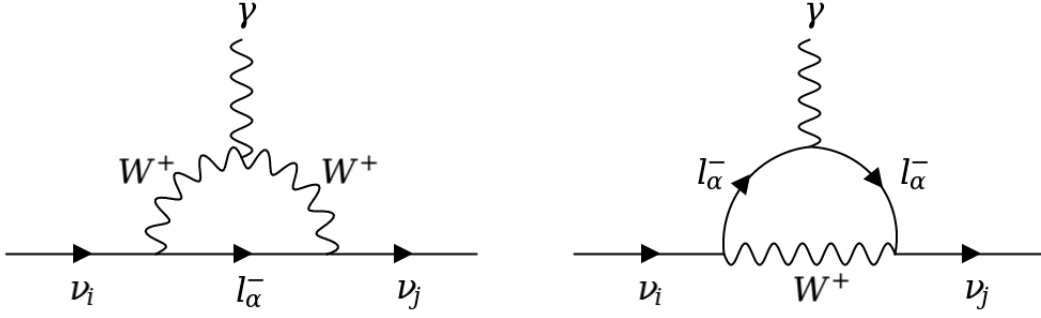


Figure 2.2: One loop Feynman diagrams contributing to the Dirac neutrino vertex function in the MESM in the unitary gauge;  $\alpha = e, \mu, \tau$  and  $i, j = 1, 2, 3$ . In the renormalizable  $R_\xi$  gauge there are extra diagrams in which internal  $W$  lines are replaced by unphysical Higgs lines [37–39].

For the diagonal case  $j = k$ , the electric dipole moments vanish, while the magnetic dipole moments are given by

$$\mu_{kk}^D \simeq \frac{3eG_F m_k}{8\sqrt{2}\pi^2} \approx 3.2 \times 10^{-19} \left( \frac{m_k}{1\text{eV}} \right) \mu_B, \quad (2.24)$$

where  $\mu_B$  is the Bohr magneton. The Dirac NMM's are thus proportional to their corresponding mass in the MESM. Given  $m_\nu \sim 0.1$  eV, this value is about nine orders of magnitude below the current best experimental bounds ( $\sim 10^{-11} \mu_B$ ). For the transition magnetic moments ( $k \neq j$ ) in Eq. (2.23), we obtain

$$\begin{aligned} \mu_{kj}^D &\simeq -\frac{3eG_F}{32\sqrt{2}\pi^2} (m_k + m_j) \sum_{\alpha=e,\mu,\tau} U_{\alpha k}^* U_{\alpha j} \left( \frac{m_\alpha}{m_W} \right)^2, \\ i\epsilon_{kj}^D &\simeq -\frac{3eG_F}{32\sqrt{2}\pi^2} (m_k - m_j) \sum_{\alpha=e,\mu,\tau} U_{\alpha k}^* U_{\alpha j} \left( \frac{m_\alpha}{m_W} \right)^2. \end{aligned} \quad (2.25)$$

Since  $(m_\alpha/m_W)^2 \sim 10^{-4}$ , these terms are further suppressed relative to their diagonal values. This is called GIM suppression, named after a similar mechanism in hadronic interactions in which the unitary mixing matrix produces an extra suppression in the flavor changing neutral currents.

In the case of Majorana neutrino, for each diagram in Fig. 2.2 there is an additional diagram containing charge conjugate fields. This is due to the non-trivial weak interaction

of the right-handed antineutrinos, while such contributions are absent for Dirac neutrinos since right-handed neutrinos have no weak interaction. The diagonal dipole moments vanish in this case, while the transition magnetic moments ( $k \neq j$ ) are given by [1, 2, 36]

$$\begin{aligned}\mu_{kj}^M &\simeq -\frac{3eG_F}{16\sqrt{2}\pi^2}(m_k + m_j) \sum_{\alpha=e,\mu,\tau} i \operatorname{Im}(U_{\alpha k}^* U_{\alpha j}) \left(\frac{m_\alpha}{m_W}\right)^2, \\ \epsilon_{kj}^M &\simeq \frac{3eG_F}{16\sqrt{2}\pi^2}(m_k - m_j) \sum_{\alpha=e,\mu,\tau} i \operatorname{Re}(U_{\alpha k}^* U_{\alpha j}) \left(\frac{m_\alpha}{m_W}\right)^2.\end{aligned}\quad (2.26)$$

If CP is conserved then the matrix elements  $U_{\alpha k}^* U_{\alpha j}$  are either real (when  $\nu_k$  and  $\nu_j$  have same CP phase) or purely imaginary (when they have opposite phase), thus only one of  $\epsilon_{kj}^M$  and  $\mu_{kj}^M$  remains nonvanishing respectively [31]. From Eq.(2.26) it can be seen that in this case also the transition dipole moments are GIM-suppressed and are of the same order of magnitude as the Dirac neutrinos.

From Eqs. (2.23) and (2.26) it can be seen that the NDM's are proportional to the neutrino mass. This can be understood if we note that the tensor and pseudo-tensor bilinears corresponding to the magnetic and electric dipole moment respectively are chirality changing operators, which connect left-chiral states with the right-chiral ones :

$$\bar{\psi}\sigma_{\mu\nu}\psi = \bar{\psi}_L\sigma_{\mu\nu}\psi_R + \text{h.c.}, \quad \bar{\psi}\sigma_{\mu\nu}\gamma_5\psi = \bar{\psi}_L\sigma_{\mu\nu}\gamma_5\psi_R + \text{h.c.}\quad (2.27)$$

In the MESM, since the right-chiral projections of fermions are  $SU(2)_L$  singlets, they do not interact with  $W^\pm$ . Thus in Fig. 2.2 it seems that only the left chiral fermions can flow in the external lines. To obtain chirality changing contributions one must include neutrino mass insertion at one of the external legs (see Fig. 2.3a). Hence NDM's are proportional to the neutrino mass.

## 2.2.2 Experimental limits and large magnetic moments

The most sensitive probe of the neutrino magnetic moment (NMM) is provided by direct measurements of the low energy (anti)neutrino-electron scattering. These experiments utilize solar, accelerator and reactor neutrinos as sources and furnish model independent NMM bounds. The scattering cross section for the process  $\nu_\alpha e \rightarrow \nu_\alpha e$  receives an extra contribution due to finite NMM, in addition to the usual term due to SM weak interaction. In the ultrarelativistic limit, the NMM term changes the helicity of the final neutrino state while the SM term conserves helicity. Thus these two terms add incoherently and final cross section can be written as [40]

$$\frac{d\sigma}{dT_e} = \left( \frac{d\sigma}{dT_e} \right)_{\text{SM}} + \left( \frac{d\sigma}{dT_e} \right)_{\text{NMM}}, \quad (2.28)$$

where  $T_e$  is the kinetic energy of the recoil electron. The NMM contribution is explicitly given by [41]

$$\left( \frac{d\sigma}{dT_e} \right)_{\text{NMM}} = \frac{\pi\alpha^2}{m_e^2} \left( \frac{1}{T_e} - \frac{1}{E} \right) \left( \frac{\mu_{\nu_\alpha}}{\mu_B} \right)^2, \quad (2.29)$$

where  $\mu_{\nu_\alpha}$  is the effective NMM,  $m_e$  is the electron mass,  $E$  is the neutrino energy and  $\alpha$  is the electromagnetic coupling constant. The effective NMM takes into account the neutrino mixing and oscillations during the propagation between the source and the detector and is given by [42]

$$(\mu_{\nu_\alpha}(L, E))^2 = \sum_j \left| \sum_k U_{\alpha k}^* e^{-iE_k L} \mu_{jk} \right|^2, \quad (2.30)$$

where  $L$  is the distance between source and detector and  $\mu_{jk}$  is the magnetic moment matrix, which in general contains both electric and magnetic dipole terms. For antineutrinos this term differs only by a phase factor. Thus the observable  $\mu_{\nu_\alpha}$  is an effective parameter and its exact implications depends on the experimental baseline.

The two terms in Eq. (2.28) exhibit different dependence on the electron recoil energy  $T_e$ . In particular, from Eq. (2.29) it can be seen that  $(d\sigma/dT_e)_{\text{NMM}}$  increases as we go

towards smaller  $T_e$ . Thus one can probe smaller values of  $\mu_{\nu_\alpha}$  by lowering the threshold value of  $T_e$ . In fact, for  $T_e \ll E$  the magnitude of  $(d\sigma/dT_e)_{\text{NMM}}$  exceeds the SM value  $(d\sigma/dT_e)_{\text{SM}}$  if [31]

$$T_e \lesssim \frac{\pi^2 \alpha^2}{G_F^2 m_e^3} \left( \frac{\mu_{\nu_\alpha}}{\mu_B} \right)^2 \approx 3 \times 10^{22} \left( \frac{\mu_{\nu_\alpha}}{\mu_B} \right)^2 \text{ keV}. \quad (2.31)$$

In a typical scattering experiment the observables which are measured are kinetic energy and scattering angle of the recoil electron. The observed agreement between the measured and expected recoil energy spectrum, assuming weak interaction alone, is then used to place upper bounds on  $\mu_{\nu_\alpha}$ . So far the most stringent bounds have been obtained in the following reactor experiments:

$$\mu_{\bar{\nu}_e} < \begin{cases} 9 \times 10^{-11} \mu_B & \text{MUNU [43],} \\ 7.4 \times 10^{-11} \mu_B & \text{TEXONO [44],} \\ 2.9 \times 10^{-11} \mu_B & \text{GEMMA [45].} \end{cases} \quad (2.32)$$

Several accelerator experiments have also been performed to search for NMM. The LAMPF and LSND experiments [46, 47] measured the  $\nu_e e^- \rightarrow \nu_e e^-$  scattering using neutrinos from muon decay at rest to obtain bounds on  $\mu_{\nu_e}$ . They also obtained bounds on  $\mu_{\nu_\mu}$  using  $\nu_\mu$  and  $\bar{\nu}_\mu$  fluxes from  $\pi^+$  and  $\mu^+$  decay. Finally, the DONUT experiment [48] identified the  $\nu_\tau$  component in the neutrino beam and investigated the  $\nu_\tau - e^-$  scattering events to place bounds on  $\nu_\tau$ . These results can be summarized as:

$$\begin{aligned} \mu_{\nu_e} &< \begin{cases} 10.8 \times 10^{-10} \mu_B & \text{LAMPF [46],} \\ 1.1 \times 10^{-9} \mu_B & \text{LSND [46],} \end{cases} \\ \mu_{\nu_\mu} &< \begin{cases} 7.4 \times 10^{-10} \mu_B & \text{LAMPF [46],} \\ 6.8 \times 10^{-10} \mu_B & \text{LSND [47],} \end{cases} \\ \mu_{\nu_\tau} &< 3.9 \times 10^{-7} \mu_B & \text{DONUT [48].} \end{aligned} \quad (2.33)$$

In addition, the search for NMM has also been performed at two major solar neutrino experiments viz. Super-Kamiokande [49] and Borexino [50]. Just like the experiments with reactor antineutrinos, these experiments also look for distortions in the energy spectrum of recoil electrons arising due to nonzero NMM of solar neutrino. They have obtained the following upper limits:

$$\mu_{\text{solar}} < \begin{cases} 1.1 \times 10^{-10} \mu_B & \text{Super - Kamiokande [49],} \\ 2.8 \times 10^{-11} \mu_B & \text{Borexino [50].} \end{cases} \quad (2.34)$$

In addition to the above measurements the XENON1T experiment has recently observed excess electron recoil events in low energy range of a few keV [51]. These excess events can be explained by the electromagnetic interaction of solar neutrinos, having Majorana transition magnetic moments in the range  $(1 - 3) \times 10^{-11} \mu_B$ , with the electrons in the detector [52, 53].

From the above bounds it is clear that the sensitivity of the present experiments is many orders away from the MESM predictions. To bridge this gap many theoretical models have been postulated which predict large NMM in the range  $(10^{-10} - 10^{-16}) \mu_B$  for Dirac and Majorana neutrinos. For example the left-right symmetric model predict enhanced NMM by averting the proportionality between NMM and neutrino mass [1, 2, 36, 54, 55]. This model is based on gauge group  $SU(2)_L \times SU(2)_R \times U(1)_{B-L}$ , so that at high energies parity invariance is restored and coupling constants satisfy  $g_L = g_R = g$ . Thus in addition to the SM  $W_L$  boson there is a heavier gauge boson  $W_R$  which arises due to the  $SU(2)_R$  part of the group and mediates right-handed charged-current weak interactions. The mixing between the  $W_L$  and  $W_R$  allows us to obtain Feynman diagram of the type shown in Fig. 2.3b, in which the mass insertion can take place in the internal fermion line and thus avoiding the proportionality between NMM and neutrino mass. In this model, for Dirac

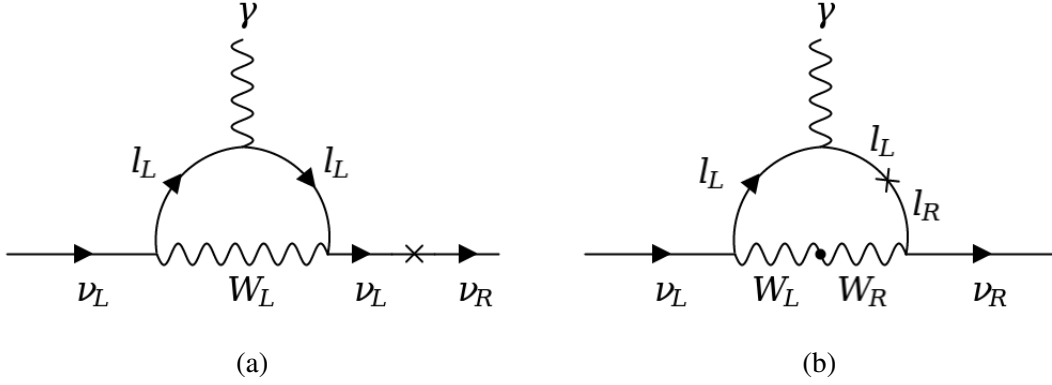


Figure 2.3: Typical Feynman diagrams contributing to the NMM vertex function at one-loop level. The cross in (a) and (b) represents mass insertion at external and internal fermion line respectively. In (b) the black dot shows  $W_L - W_R$  mixing.

neutrinos one obtains [1]:

$$\mu_{kj} \simeq \frac{eG_F}{4\sqrt{2}\pi^2} \sin 2\xi \sum_{\alpha=e,\mu,\tau} m_\alpha \left( e^{i\psi} U_{\alpha k}^* V_{\alpha j} + e^{-i\psi} U_{\alpha k} V_{\alpha j}^* \right), \quad (2.35)$$

where  $U$  and  $V$  are the mixing matrices of left-handed and right-handed neutrinos respectively,  $\xi$  is the mixing angle between  $W_L$  and  $W_R$  bosons and  $\psi$  is the CP violating phase. Thus in this case the NMM's are proportional to the charged lepton masses. However, there are strong experimental and theoretical constraints on the mixing angle  $\xi$  which limit  $\sin \xi < 10^{-7}$  [55], which implies that  $\mu_{kj} \simeq 10^{-16} \mu_B$ . To obtain larger magnetic moments, charged scalar particles are added to MESM with right-handed neutrinos [1, 56, 57] or to the left-right symmetric model [58]. The charged scalar contributions can give rise to magnetic moments in the range  $\mu_\nu \sim (10^{-11} - 10^{-10}) \mu_B$ . However, the above models suffer from large radiative corrections to the neutrino mass which is in conflict with the current experimental bounds. To obtain small neutrino mass a counter term must be introduced in the Lagrangian to cancel the divergent mass terms. Thus these models require some fine-tuning to keep neutrino mass consistent with the experimental bounds [1, 2].

In the models which generate new physics beyond the SM, there is a generic relation between neutrino mass and magnetic moment [1, 2, 31]. Let the NMM is generated by new physics at scale  $\Lambda \gg v$  described by loop diagrams of the type Fig. 2.1, where the blob

contains new physics effects. The NMM can be estimated as

$$\mu_\nu \sim \frac{eG}{\Lambda}, \quad (2.36)$$

where  $G$  is some combination of coupling constants and other loop factors. The same diagram with photon line removed gives radiative correction to the neutrino mass which is of the order

$$\delta m_\nu \sim G\Lambda. \quad (2.37)$$

From Eqs. (2.36) and (2.37) we obtain the relation

$$\delta m_\nu \sim \frac{\Lambda^2}{2m_e} \frac{\mu_\nu}{\mu_B} = \frac{\mu_\nu}{10^{-18}\mu_B} \left( \frac{\Lambda}{\text{TeV}} \right)^2 \text{ eV}. \quad (2.38)$$

Thus assuming  $\Lambda \sim 1 \text{ TeV}$ , NMM of  $\mu_\nu \sim 10^{-11}\mu_B$  will simultaneously generate large radiative corrections to the neutrino mass and a particular fine-tuning is required to keep neutrino masses within experimental bounds.

To avoid fine-tuning we require  $\delta m_\nu \lesssim m_\nu$  [59]. For  $m_\nu \sim 0.1 \text{ eV}$  and  $\Lambda \sim 1 \text{ TeV}$ , we obtain a naive naturalness bound from Eq. (2.38)

$$\mu_\nu \lesssim 10^{-19}\mu_B. \quad (2.39)$$

An effective field theory calculation of NMM for Dirac and Majorana neutrinos generated via new physics above the electroweak scale has been carried out in Refs. [60–62]. It was found that for new physics scale of  $\Lambda \sim 1 \text{ TeV}$  and neutrino mass of  $m_\nu \sim 0.2 \text{ eV}$  the naturalness condition  $\delta m_\nu \lesssim m_\nu$  yields a model-independent bound of  $\mu_\nu \lesssim 10^{-15}\mu_B$  for Dirac neutrinos. However for Majorana neutrinos due to anti-symmetry of the NMM operator the naturalness bound is much weaker ( $\lesssim 10^{-9}\mu_B$ ). Thus an experimental observation of NMM  $\gtrsim 10^{-14}\mu_B$  could be a plausible signature of a Majorana neutrinos [31].

From Eq. (2.38) it can be seen that to generate large NMM in a consistent manner one

has to find some mechanism which suppresses neutrino mass correction. In the following we briefly discuss two models which generate naturally large NMM without adding unacceptably large corrections to the neutrino mass.

(i) *Voloshin's symmetry*. One of the first attempts to solve the above problem was made by Voloshin [63], who proposed to suppress the ratio  $m_\nu/\mu_\nu$  using the symmetry properties of the NMM and mass operators. Under  $\nu_L \leftrightarrow \nu_L^c$  the Dirac mass and NMM terms transform as [64]:

$$\begin{aligned}\bar{\nu}_L C^{-1} \nu_L^c &\rightarrow \bar{\nu}_L^c C^{-1} \nu_L, \\ \bar{\nu}_L C^{-1} \sigma_{\mu\nu} \nu_L^c F^{\mu\nu} &\rightarrow -\bar{\nu}_L^c C^{-1} \sigma_{\mu\nu} \nu_L F^{\mu\nu}.\end{aligned}\tag{2.40}$$

Consider an  $SU(2)_\nu$  symmetry under which  $\nu_L$  and  $\nu_L^c$  transform as doublet. Then the mass term being symmetric under exchange of  $\nu_L$  and  $\nu_L^c$  would transform as a triplet, while the NMM term would be a singlet. So a model in which  $SU(2)_\nu$  is an exact symmetry, the mass term is forbidden while the NMM term is allowed. Thus one can get large  $\mu_\nu$  with  $m_\nu = 0$ . However, implementation of Voloshin's  $SU(2)_\nu$  symmetry is problematic since it does not commute with the gauge symmetry of  $SU(2)_L$  and so it is broken in realistic models [64]. Also some fine-tuning of parameters is again required to generate  $\mu_\nu \sim 10^{-12} \mu_B$  [59, 65].

To avoid these problems with  $SU(2)_\nu$  it was suggested in Ref. [66] to implement the Voloshin's mechanism using  $SU(2)_H$  horizontal symmetry which commutes with  $SU(2)_L$ . In this model, the  $SU(2)_H$  symmetry acts on the electron and muon generation and gives rise to large transition magnetic moment  $\mu_{\nu_e \nu_\mu}$  for Majorana neutrino. In the limit of exact  $SU(2)_H$  symmetry  $m_e = m_\mu$  and neutrino remain massless with nonzero magnetic moment. The symmetry must be thus broken to get  $m_e \neq m_\mu$  which generates small neutrino masses which can be controlled by imposing certain naturalness conditions. Subsequently a number of variants of Voloshin's symmetry mechanism and horizontal  $SU(2)_H$

symmetry have been considered in which it is possible to generate transition magnetic moments in the range  $\sim (10^{-12} - 10^{-10} \mu_B)$  while keeping the neutrino mass naturally small [52, 66–71].

(ii) *Zee’s model and spin suppression.* The spin suppression is another mechanism through which one can generate large NMM with small neutrino mass [72]. This mechanism is realized in Zee’s model [73] which is based on the SM gauge group  $SU(2)_L \times U(1)_Y$  and contains two Higgs doublet and one charged scalar  $h^+$  which is an  $SU(2)_L$  singlet. In this model the NMM contribution is obtained through the coupling  $\gamma h^+ W$  at two loop level. The corresponding mass contribution is obtained by removing the photon line. However, this would involve transition from spin 0 to spin 1 which is not possible with transversely polarized  $W$  boson. Thus due to spin conservation only the longitudinal component of  $W$  boson contributes in the mass diagram which leads to a suppression factor of  $m_l^2/m_W^2$ , where  $m_l$  is generic fermion mass [65]. A recent analysis of this model yields neutrino transition magnetic moments in the range  $(2 - 4) \times 10^{-12} \mu_B$  [52].

## 2.3 Neutrino interaction with electromagnetic fields

The nontrivial electromagnetic properties of neutrinos can generate important new effects when neutrinos propagate in a medium with classical electromagnetic fields. Such situations are usually encountered in astrophysical environments where neutrino propagate over large distances through magnetic fields in vacuum and in matter. The effect of the neutrino interaction with these electromagnetic fields must be taken into account while studying the evolution of neutrino flavor and spin components. Such an interaction is analogous to the coherent forward elastic scattering of neutrinos with matter and is given by an effective potential [31]:

$$V_{h \rightarrow h'} = \lim_{q \rightarrow 0} \frac{\langle \nu(p', h') | \int d^3x \mathcal{H}_{\text{em}}(x) | \nu(p, h) \rangle}{\langle \nu(p, h) | \nu(p, h) \rangle}, \quad (2.41)$$

where  $q = p - p'$ , and  $h$  denote neutrino helicity. Eq. (2.41) implies the possibility of helicity transitions ( $h' \neq h$ ) in presence of electromagnetic fields. The neutrino states are normalized as

$$\langle \nu(p, h') | \nu(p, h) \rangle = 2EV\delta_{hh'}, \quad (2.42)$$

where  $E = E'$  is the neutrino energy in limit  $q \rightarrow 0$  and  $V$  is the total volume. Substituting the normalization condition (2.42) in Eq. (2.41) we obtain

$$V_{h \rightarrow h'} = \frac{1}{2EV} \lim_{q \rightarrow 0} \left\langle \nu(p', h') \left| \int d^3x j_\mu(x) A^\mu(x) \right| \nu(p, h) \right\rangle. \quad (2.43)$$

Using Eqs. (2.2) and (2.5) we can write

$$\begin{aligned} V_{h \rightarrow h'} &= \frac{1}{2EV} \lim_{q \rightarrow 0} \int d^3x e^{-iq \cdot x} \langle \nu(p', h') | j_\mu(0) | \nu(p, h) \rangle A^\mu(x) \\ &= \frac{1}{2EVT} \lim_{q \rightarrow 0} \bar{u}(p', h') \Gamma_\mu(p, p') u(p, h) \tilde{A}^\mu(x), \end{aligned} \quad (2.44)$$

where  $T$  is the normalization time and

$$\tilde{A}^\mu(x) = \int d^4x e^{-iq \cdot x} A^\mu(x) \quad (2.45)$$

is the Fourier transform of  $A^\mu(x)$ . Substituting the expression (2.9) of the vertex function in Eq. (2.44)

$$\begin{aligned} V_{h \rightarrow h'} &= \frac{1}{2EVT} \lim_{q \rightarrow 0} \bar{u}(p', h') \left( \mathbb{f}_Q(q^2) \gamma_\mu - i \mathbb{f}_M(q^2) \sigma_{\mu\nu} q^\nu + \mathbb{f}_E(q^2) \sigma_{\mu\nu} q^\nu \gamma_5 + \right. \\ &\quad \left. \mathbb{f}_A(q^2) (q^2 \gamma_\mu - q_\mu \not{q}) \gamma_5 \right) u(p, h) \tilde{A}^\mu(x). \end{aligned} \quad (2.46)$$

Now using the following identities in Eq. (2.46):

$$\bar{u}(p', h') \gamma_\alpha u(p, h) = \bar{u}(p', h') \left( \frac{(p' + p)_\alpha}{2m} + \frac{i \sigma_{\alpha\beta} (p' - p)^\beta}{2m} \right) u(p, h), \quad (2.47)$$

$$\sigma_{\alpha\beta} (p' - p)^\beta A^\alpha = \sigma_{\alpha\beta} q^\beta A^\alpha = -\frac{i}{2} \sigma_{\alpha\beta} F^{\alpha\beta}, \quad (2.48)$$

where  $F^{\alpha\beta} = \partial^\alpha A^\beta - \partial^\beta A^\alpha$  is the electromagnetic field strength tensor, we obtain after neglecting the anapole term:

$$V_{h_i \rightarrow h_f} = \frac{1}{VT} \lim_{q \rightarrow 0} \int d^4x \left\{ \mathbb{f}_Q(q^2) \bar{u}(p', h') \frac{(p' + p)_\mu}{4mE} u(p, h) A^\mu(x) + \frac{1}{4E} \bar{u}(p', h') \sigma_{\mu\nu} F^{\mu\nu} \left( \frac{\mathbb{f}_Q(q^2)}{2m} - \mathbb{f}_M(q^2) - i\mathbb{f}_E(q^2) \gamma_5 \right) u(p, h) \right\} e^{-iq \cdot x}. \quad (2.49)$$

Considering electromagnetic fields which are approximately constant over the dimensions of the neutrino wave packet, we can consider the integrand in Eq. (2.50) to be a constant. Finally we take the limit  $q \rightarrow 0$ , and use the normalization

$$\bar{u}(p, h') u(p, h) = 2m \delta_{h'h} \quad (2.50)$$

to obtain

$$V_{h \rightarrow h'} = \mathbb{q}_1 \frac{p_\mu}{E} A^\mu(x) \delta_{h'h} + \frac{1}{4E} \bar{u}(p, h') \sigma_{\mu\nu} F^{\mu\nu} \left( \frac{\mathbb{q}_1}{2m} - \mu - i\epsilon \gamma_5 \right) u(p, h). \quad (2.51)$$

Consider the first term in Eq. (2.21) in an electrostatic field  $A^\mu = (A^0, 0, 0, 0)$ :  $V_{h \rightarrow h'} = \mathbb{q}_1 A^0 \delta_{h'h}$ . This term corresponds to the familiar expression of electrostatic energy of a charged particle in a potential. The first term in the second bracket corresponds to the charge magnetic moment of the particle. Since for neutrinos we take  $\mathbb{q}_1 = 0$ , only last two terms remain. As shown in Section 2.1 these two terms correspond to the "anomalous dipole moments" which are generated due to quantum loop effects.

To cast Eq. (2.51) in a familiar form, we first consider the case of helicity conserving potential which we can write as [31]:

$$V_{h \rightarrow h} = -\frac{1}{4E} \text{Tr} \left[ \bar{u}(p, h) \sigma_{\mu\nu} F^{\mu\nu} \left( \mu + i\epsilon \gamma_5 \right) u(p, h) \right]. \quad (2.52)$$

The spinors obey the identity [4]:

$$\begin{aligned}\frac{\bar{u}(p, h)u(p, h)}{2m} &= \Lambda_+ P_h, \\ \text{where } \Lambda_+ &= \frac{\not{p} + m}{2m}, \\ \text{and } P_h &= \frac{1 + h\gamma^5 \not{p}}{2}.\end{aligned}\tag{2.53}$$

Substituting Eq. (2.53) in Eq. (2.52) and using the following trace properties of gamma matrices

$$\begin{aligned}\text{Tr}[\gamma^\alpha \gamma^\beta \gamma^\mu \gamma^\nu] &= 4(g^{\alpha\beta} g^{\mu\nu} - g^{\alpha\mu} g^{\beta\nu} + g^{\alpha\nu} g^{\beta\mu}), \\ \text{Tr}[\gamma^\alpha \gamma^\beta \gamma^\mu \gamma^\nu \gamma^5] &= -4i\epsilon^{\alpha\beta\mu\nu},\end{aligned}\tag{2.54}$$

we obtain

$$V_{h \rightarrow h} = -\frac{h}{2E} \left( \mu \epsilon_{\alpha\beta\mu\nu} p^\alpha s^\beta F^{\mu\nu} - 2\epsilon F^{\mu\nu} s_\mu p_\nu \right).\tag{2.55}$$

Expanding this term and using the respective expressions of the electric and magnetic fields

$$\mathcal{E}^i = F^{0i}, \quad \mathcal{B}^i = -\frac{1}{2}\epsilon^{ijk} F^{jk},\tag{2.56}$$

where the  $i, j, k \neq 0$ , we get

$$V_{h \rightarrow h} = -\frac{m}{E} (\vec{\mu} \cdot \vec{\mathcal{B}} + \vec{\epsilon} \cdot \vec{\mathcal{E}}),\tag{2.57}$$

where

$$\vec{\mu} = h\mu \frac{\vec{p}}{|p|}, \quad \vec{\epsilon} = h\epsilon \frac{\vec{p}}{|p|}.\tag{2.58}$$

Thus the helicity conserving potential comes out to be proportional to the longitudinal component of the electric and magnetic fields. In the non relativistic limit  $E \approx m$ , Eq. (2.57) reduce to the usual classical expression for spin precession. However, in the case of

ultra relativistic neutrinos the factor  $m/E$  leads to suppression of the longitudinal components of the electromagnetic fields in the Hamiltonian.

To calculate the helicity changing potential  $V_{-h \rightarrow h}$  we define the matrix

$$M = \vec{\tau} \cdot \vec{\gamma} \gamma_5, \quad (2.59)$$

where  $\vec{\tau}$  is a unit vector orthogonal to  $\vec{p}$ . It can be shown that [31]

$$\frac{u(p, -h)\bar{u}(p, h)}{2m} = M\Lambda_+(p)P_h = P_{-h}\Lambda_+(p)M. \quad (2.60)$$

Substituting Eq. (2.60) in Eq. (2.52) and using the trace properties Eq. (2.54), we obtain

$$V_{-h \rightarrow h} = -\frac{\tau^k}{2E} \left[ \mu (\epsilon^{k\alpha\mu\nu} p_\alpha F_{\mu\nu} + 2imh F^{k\alpha} s_\alpha) + \epsilon (2F^{k\alpha} p_\alpha - imh \epsilon^{k\alpha\mu\nu} s_\alpha F_{\mu\nu}) \right], \quad (2.61)$$

Expanding in terms of electric and magnetic fields (2.56), we have

$$\begin{aligned} V_{-h \rightarrow h} = & \mu \left( -\vec{\tau} \cdot \vec{\mathcal{B}} - ih\vec{\tau} \cdot \frac{\vec{p} \times \vec{\mathcal{B}}}{|\vec{p}|} + \vec{\tau} \cdot \frac{\vec{p} \times \vec{\mathcal{E}}}{E} - ih\frac{|\vec{p}|}{E} \vec{\tau} \cdot \vec{\mathcal{E}} \right) + \\ & \epsilon \left( -\vec{\tau} \cdot \vec{\mathcal{E}} - ih\vec{\tau} \cdot \frac{\vec{p} \times \vec{\mathcal{E}}}{|\vec{p}|} - \vec{\tau} \cdot \frac{\vec{p} \times \vec{\mathcal{B}}}{E} + ih\frac{|\vec{p}|}{E} \vec{\tau} \cdot \vec{\mathcal{B}} \right). \end{aligned} \quad (2.62)$$

Since the vector  $\vec{\tau}$  is orthogonal to  $\vec{p}$ , we can choose

$$\vec{p} = (0, 0, |\vec{p}|), \quad \vec{\tau} = (-1, 0, 0). \quad (2.63)$$

Then we have

$$V_{-h \rightarrow h} = \mu \left( \mathcal{B}^1 - ih\mathcal{B}^2 + \frac{|\vec{p}|}{E} \mathcal{E}^2 + ih\frac{|\vec{p}|}{E} \mathcal{E}^1 \right) + \epsilon \left( \mathcal{E}^1 - ih\mathcal{E}^2 - \frac{|\vec{p}|}{E} \mathcal{B}^2 + ih\frac{|\vec{p}|}{E} \mathcal{B}^1 \right), \quad (2.64)$$

where  $\vec{\mathcal{E}} = (\mathcal{E}^1, \mathcal{E}^2, \mathcal{E}^3)$  and  $\vec{\mathcal{B}} = (\mathcal{B}^1, \mathcal{B}^2, \mathcal{B}^3)$ . If there is only a pure magnetic field we obtain

$$V_{-h \rightarrow h} = \left( \mu - ih \frac{|\vec{p}|}{E} \epsilon \right) \mathcal{B}_\perp, \quad (2.65)$$

where  $\mathcal{B}_\perp = \mathcal{B}^1 \pm i\mathcal{B}^2$  is the transverse component of the magnetic field. It can be seen that for the case of non-relativistic neutrinos ( $|\vec{p}| \ll E$ ) this expression correspond to the classical torque

$$V_{-h \rightarrow h} \simeq \mu \mathcal{B}_\perp = |\vec{\mu} \times \vec{\mathcal{B}}|. \quad (2.66)$$

The above expressions for the neutrino effective potential in electromagnetic fields can be generalized using vertex function Eq. (2.20) which connects different massive neutrinos states, so that Eq. (2.41) modifies to

$$V_{\nu_j(h) \rightarrow \nu_k(h')} = \lim_{q \rightarrow 0} \frac{\langle \nu_k(p', h') | \int d^3x \mathcal{H}_{\text{em}}(x) | \nu_j(p, h) \rangle}{\langle \nu(p, h) | \nu(p, h) \rangle}. \quad (2.67)$$

In this case the potential is generated by transition dipole moments which is of special interest for Majorana neutrinos. The helicity flipping potential (2.65) can thus be generalized to

$$V_{\nu_j(h) \rightarrow \nu_k(h')} = \left( \mu_{kj} - ih \frac{|\vec{p}|}{E} \epsilon_{kj} \right) \mathcal{B}_\perp. \quad (2.68)$$

The expressions derived in this Section can be used to study the evolution of neutrino spin and spin-flavor in a medium in presence of electromagnetic fields.

### 2.3.1 Neutrino spin and spin-flavor precession

Consider a Dirac neutrino with diagonal magnetic moment  $\mu$  propagating in a magnetic field  $\vec{\mathcal{B}}$ . If the neutrino is initially in a definite helicity state  $h_i$ , then after a time  $t$ , the neutrino state is described by a superposition of the two helicity states

$$|\nu(t)\rangle = \sum_{h=\pm 1} \psi_h(t) |\nu(p, h)\rangle. \quad (2.69)$$

where  $\psi_h$  represents the amplitude for helicity state  $h$ . The time evolution of  $|\nu(t)\rangle$  is given by

$$i \frac{d}{dt} |\nu(t)\rangle = H_{\text{em}}(t) |\nu(t)\rangle, \quad (2.70)$$

where  $H_{\text{em}} = \int d^3x \mathcal{H}_{\text{em}}$  is the interaction Hamiltonian. From Eqs.(2.41), (2.69) and (2.70), we obtain

$$i \frac{d\psi_h(t)}{dt} = \sum_{h'=\pm 1} \psi_{h'}(t) \frac{\langle \nu(p, h) | H_{\text{em}}(t) | \nu(p, h') \rangle}{\langle \nu(p, h) | \nu(p, h) \rangle} = \sum_{h'=\pm 1} \psi_{h'}(t) V_{h' \rightarrow h}(t), \quad (2.71)$$

with  $\psi_h(0) = \delta_{hh_i}$ . Since the helicity conserving potential (2.57) is strongly suppressed for ultrarelativistic neutrinos, we examine only the effect of the helicity flipping potential (2.65) which depends only on the transverse magnetic field. Considering only the contribution due to magnetic moment, we can write

$$V_{h' \rightarrow h} = \mu \mathcal{B}_\perp \delta_{-hh'}. \quad (2.72)$$

The matrix representation of Eq. (2.71) in the basis  $|\nu\rangle = (\nu_L \ \nu_R)^T$  is then given by

$$i \frac{d}{dx} \begin{pmatrix} \psi_L(x) \\ \psi_R(x) \end{pmatrix} = \begin{pmatrix} 0 & \mu \mathcal{B}_\perp(x) \\ \mu \mathcal{B}_\perp(x) & 0 \end{pmatrix} \begin{pmatrix} \psi_L(x) \\ \psi_R(x) \end{pmatrix}, \quad (2.73)$$

where we approximated the distance  $x$  along the neutrino trajectory with time  $t$  for ultrarelativistic neutrinos [31]. Let us now consider the transition  $\nu_{eL} \rightarrow \nu_{eR}$  which may be of importance in astrophysical objects such as the Sun [74]. In this case the matter effects due to coherent forward scattering of neutrinos with the background particles become important and Eq. (2.73) becomes

$$i \frac{d}{dx} \begin{pmatrix} \psi_L(x) \\ \psi_R(x) \end{pmatrix} = \begin{pmatrix} V(x) & \mu \mathcal{B}_\perp(x) \\ \mu \mathcal{B}_\perp(x) & 0 \end{pmatrix} \begin{pmatrix} \psi_L(x) \\ \psi_R(x) \end{pmatrix}, \quad (2.74)$$

where the matter potential  $V$  acts only on the left-handed Dirac neutrinos. The Eq. (2.74) can also be derived using the quasiclassical Bargmann-Michel-Telegdi (BMT) equation for the evolution of neutrino spin in presence of magnetic field [75].

Since in a more general case a neutrino state is a superposition of different massive neutrinos with both helicities, Eq. (2.69) must be generalized to

$$|\nu(t)\rangle = \sum_k \sum_{h=\pm 1} \psi_{kh}(t) |\nu_k(p, h)\rangle. \quad (2.75)$$

The time evolution of the state  $|\nu(t)\rangle$  is governed by the Schrödinger equation

$$i \frac{d}{dt} |\nu(t)\rangle = H(t) |\nu(t)\rangle, \quad (2.76)$$

where the Hamiltonian  $H$  is the sum of vacuum Hamiltonian  $H_0$ , weak interaction Hamiltonian  $H_{\text{wk}}$  and the electromagnetic Hamiltonian  $H_{\text{em}}$ :

$$H = H_0 + H_{\text{wk}} + H_{\text{em}}. \quad (2.77)$$

From Eqs. (2.75) and (2.76) the evolution equation for the helicity amplitudes can be easily obtained

$$i \frac{d\psi_{kh}(t)}{dt} = \sum_j \sum_{h'=\pm 1} \frac{\langle \nu_k(p, h) | H(t) | \nu_j(p, h') \rangle}{\langle \nu(p, h) | \nu(p, h) \rangle} \psi_{jh'}(t). \quad (2.78)$$

For ultrarelativistic neutrinos we have

$$\frac{\langle \nu_k(p, h) | H_0 | \nu_j(p, h') \rangle}{\langle \nu(p, h) | \nu(p, h) \rangle} = \left( E_k + \frac{m_k^2}{2E_k} \right) \delta_{kj} \delta_{hh'} \approx \left( E + \frac{m_k^2}{2E} \right) \delta_{kj} \delta_{hh'}, \quad (2.79)$$

where  $m_k$  and  $E_K$  denotes the mass and energy of the  $k$ th eigenstate. Now let us consider the mixing between neutrino eigenstates. For the left-handed neutrinos we have

$$|\nu_k(p, -)\rangle = \sum_l U_{\alpha k} |\nu_\alpha(p, -)\rangle, \quad (2.80)$$

where  $U$  is the unitary mixing matrix. In the case of right-handed neutrinos the difference between Dirac and Majorana neutrinos shows up. In the case of right-handed Dirac neutrinos the mixing is arbitrary since they are sterile to weak interactions while right-handed Majorana neutrinos interact as Dirac antineutrinos.

$$|\nu_k^M(p, +)\rangle = \sum_l U_{\alpha k}^* |\nu_\alpha(p, +)\rangle. \quad (2.81)$$

Thus we can define the generalized mixing relation

$$|\nu_k(p, h)\rangle = \sum_\alpha U_{\alpha k}^{(h)} |\nu_\alpha(p, h)\rangle, \quad (2.82)$$

where  $U^{(-)} = U$  and for Dirac neutrinos we choose:  $U^{(+)} = U$ , while for Majorana neutrinos:  $U^{(+)} = U^*$ . The matrix elements of the weak interaction Hamiltonian  $H_{\text{wk}}$  can now be written as

$$\frac{\langle \nu_k(p, h) | H_{\text{wk}}(t) | \nu_j(p, h') \rangle}{\langle \nu(p, h) | \nu(p, h) \rangle} = \sum_l U_{\alpha k}^{(h)*} V_\alpha^{(h)}(t) U_{\alpha l}^{(h)} \delta_{hh'}, \quad (2.83)$$

where the matter potential for neutrino in flavor state  $\alpha$  is given by  $V_\alpha^{(-)} = V_\alpha$ ,  $V_\alpha^{(+)} = 0$  (Dirac neutrinos) and  $V_\alpha^{(+)} = -V_\alpha$  (Majorana neutrinos). Now let us finally consider the electromagnetic part of the Hamiltonian for which we have

$$\frac{\langle \nu_k(p, h) | H_{\text{em}} | \nu_j(p, h') \rangle}{\langle \nu(p, h) | \nu(p, h) \rangle} = \mu_{kj} \mathcal{B}_\perp(t) \delta_{-hh'}. \quad (2.84)$$

Substituting Eqs. (2.79), (2.83) and (2.84) in the equation (2.78), we obtain the equation for neutrino spin-flavor evolution with distance  $x$  along the neutrino trajectory:

$$i \frac{d\psi_{kh}(x)}{dx} = \sum_j \sum_{h'=\pm 1} \left[ \left( \frac{m_k^2}{2E} \delta_{kj} + \sum_\alpha U_{\alpha k}^{(h)*} V_\alpha^{(h)}(x) U_{\alpha j}^{(h)} \right) \delta_{hh'} + \mu_{kj} B_\perp(x) \delta_{-hh'} \right] \psi_{jh'}(x). \quad (2.85)$$

Eq. (2.85) gives the evolution in mass eigenbasis. To convert it in flavor basis we rewrite the Eq. (2.75) in terms of flavor states as

$$|\nu(t)\rangle = \sum_\alpha \sum_{h=\pm 1} \psi_{\alpha h}(t) |\nu_\alpha(p, h)\rangle. \quad (2.86)$$

Using the unitary transformation

$$|\nu_k\rangle = \sum_\alpha U_{\alpha k} |\nu_\alpha\rangle, \quad (2.87)$$

we get the relation

$$\psi_{\alpha h}(x) = \sum_k U_{\alpha k}^{(h)} \psi_{kh}(x). \quad (2.88)$$

From Eqs. (2.85) and (2.88) we obtain the evolution equation for the flavor amplitudes

$$i \frac{d\psi_{\alpha h}(x)}{dx} = \sum_\beta \sum_{h'=\pm 1} \left[ \left( \sum_k U_{\alpha k}^{(h)} \frac{m_k^2}{2E} U_{\beta k}^{(h)*} + V_\alpha^{(h)}(x) \delta_{\alpha\beta} \right) \delta_{hh'} + \mu_{\alpha\beta}^{(hh')} B_\perp(x) \delta_{-hh'} \right] \psi_{\beta h'}(x), \quad (2.89)$$

where the magnetic moment in the flavor basis is given by

$$\mu_{\alpha\beta}^{(hh')} = \sum_{k,j} U_{\alpha j}^{(h)} \mu_{kj} U_{\beta j}^{(h')*}. \quad (2.90)$$

It is interesting to compare the magnetic moment (2.90) in the flavor basis for Dirac and Majorana neutrinos, for which we obtained distinct form factors in Section 2.1. First let

us consider Dirac neutrinos for which we have

$$\mu_{\alpha\beta}^{(-+)} = \sum_{k,j} U_{\alpha k}^{(+)} \mu_{kj} U_{\beta j}^{(-)*} = \sum_{k,j} U_{\alpha k} \mu_{kj} U_{\beta j}^* = \mu_{\alpha\beta}^{(+)} \equiv \mu_{\alpha\beta}. \quad (2.91)$$

Since for Dirac neutrinos the form factors in the mass eigenbasis obey Eq. (2.21), thus we have

$$\mu_{jk} = \mu_{kj}^* \Rightarrow \mu_{\beta\alpha} = \mu_{\alpha\beta}^*. \quad (2.92)$$

For the case of Majorana neutrinos, we have

$$\mu_{\alpha\beta}^{(-+)} = \sum_{k,j} U_{\alpha k} \mu_{kj} U_{\beta j}, \quad \mu_{\alpha\beta}^{(+-)} = \sum_{k,j} U_{\alpha k}^* \mu_{kj} U_{\beta j}^*. \quad (2.93)$$

From Eq. (2.22), we can see that the transition form factors for Majorana neutrinos are anti-symmetric in mass eigenbasis

$$\mu_{jk} = -\mu_{kj} = \mu_{kj}^*. \quad (2.94)$$

This anti-symmetry of magnetic moments is preserved in the flavor basis:

$$\mu_{\alpha\beta}^{(-+)} = -\mu_{\beta\alpha}^{(-+)}, \quad \mu_{\alpha\beta}^{(+-)} = -\mu_{\alpha\beta}^{(+-)}, \quad (2.95)$$

which leads to vanishing diagonal magnetic moments in the flavor basis. In addition we have

$$\mu_{\alpha\beta}^{(-+)} = -\mu_{\alpha\beta}^{(+-)*}. \quad (2.96)$$

Using the above properties of the magnetic moment matrices, the spin-flavor evolution equation (2.89) can be used to construct appropriate Hamiltonians for Dirac and Majorana neutrinos.

### 2.3.2 Two flavor Dirac and Majorana Hamiltonian

The phenomenon of neutrino oscillations in many of the cases, for example solar and atmospheric neutrinos, can be effectively described using two neutrino mixing approximation. Considering the case of solar 1 – 2 sector and neglecting the small effects due to  $\theta_{12}$ , the mixing between the two flavor neutrinos is given by

$$\begin{pmatrix} \psi_{eh} \\ \psi_{\mu h} \end{pmatrix} = \begin{pmatrix} \cos \theta_{12} & \sin \theta_{12} \\ -\sin \theta_{12} & \cos \theta_{12} \end{pmatrix} \begin{pmatrix} \psi_{1h} \\ \psi_{2h} \end{pmatrix}, \quad (2.97)$$

where  $\theta_{12}$  is the mixing angle. First we consider Dirac neutrinos for which generalization of Eq. (2.73), with two neutrino mixing (2.97) is given by

$$i \frac{d}{dx} \begin{pmatrix} \psi_{eL} \\ \psi_{\mu L} \\ \psi_{eR} \\ \psi_{\mu R} \end{pmatrix} = H_D \begin{pmatrix} \psi_{eL} \\ \psi_{\mu L} \\ \psi_{eR} \\ \psi_{\mu R} \end{pmatrix}, \quad (2.98)$$

where the Dirac Hamiltonian is obtained from Eqs. (2.89):

$$H_D = \begin{pmatrix} -\frac{\Delta m^2}{4E} \cos 2\theta_{12} + V_e & \frac{\Delta m^2}{4E} \sin 2\theta_{12} & \mu_{ee} \mathcal{B}_\perp & \mu_{e\mu} \mathcal{B}_\perp \\ \frac{\Delta m^2}{4E} \sin 2\theta_{12} & \frac{\Delta m^2}{4E} \cos \theta_{12} + V_\mu & \mu_{\mu e} \mathcal{B}_\perp & \mu_{\mu\mu} \mathcal{B}_\perp \\ \mu_{ee} \mathcal{B}_\perp & \mu_{\mu e} \mathcal{B}_\perp & -\frac{\Delta m^2}{4E} \cos 2\theta_{12} & \frac{\Delta m^2}{4E} \sin 2\theta_{12} \\ \mu_{e\mu} \mathcal{B}_\perp & \mu_{\mu\mu} \mathcal{B}_\perp & \frac{\Delta m^2}{4E} \sin 2\theta_{12} & \frac{\Delta m^2}{4E} \cos 2\theta_{12} \end{pmatrix}, \quad (2.99)$$

where  $V_e = V_{CC} + V_{NC}$  and  $V_\mu = V_{NC}$  are matter potentials for left-handed electron and muon neutrinos respectively and  $\Delta m^2 \equiv \Delta m_{21}^2$  is the neutrino mass-squared difference. Using Eq. (2.91) and mixing matrix given in Eq. (2.97), the effective magnetic moments

for Dirac neutrinos in flavor basis can be written as,

$$\begin{aligned}
\mu_{ee} &= \mu_{11} \cos^2 \theta_{12} + \mu_{22} \sin^2 \theta_{12} + \mu_{12} \sin 2\theta_{12}, \\
\mu_{e\mu} &= \frac{1}{2} (\mu_{22} - \mu_{11}) \sin 2\theta_{12} + \mu_{12} \cos 2\theta_{12}, \\
\mu_{\mu\mu} &= \mu_{11} \sin^2 \theta_{12} + \mu_{22} \cos^2 \theta_{12} - \mu_{12} \sin 2\theta_{12},
\end{aligned} \tag{2.100}$$

where we have considered the magnetic moments  $\mu_{kj}$  in the mass eigenbasis to be real. The Hamiltonian (2.99) implies existence of two resonances which are generated by the matter potential, in addition to the usual MSW resonance which occurs in the channel  $\nu_{eL} \leftrightarrow \nu_{\mu L}$ .

(i) In the channel  $\nu_{eL} \leftrightarrow \nu_{\mu R}$ , the resonance occurs for

$$V_e = V_{\text{CC}} + V_{\text{NC}} = \frac{\Delta m^2}{2E} \cos 2\theta_{12}. \tag{2.101}$$

This density at which this resonance occurs is different from that of MSW resonance (see Section 3.2 for example).

(ii) In the channel  $\nu_{\mu L} \leftrightarrow \nu_{e R}$ , the resonance occurs for

$$V_\mu = V_{\text{NC}} = -\frac{\Delta m^2}{2E} \cos 2\theta_{12}. \tag{2.102}$$

Since  $\cos 2\theta_{12} > 0$ , and  $V_{\text{NC}}$  is negative this resonance can occur in normal matter. When these resonance conditions are satisfied, there is an enhancement in the respective transition probabilities, which is termed as resonance spin-flavor precession (RSFP) [76, 77].

Let us now consider Majorana neutrinos for which the basis vector (2.98) is given by  $(\nu_{eL}, \nu_{\mu L}, \bar{\nu}_e, \bar{\nu}_\mu)^T$ . In this basis the evolution equation Eq. (2.89) gives the Hamiltonian

$$H_M = \begin{pmatrix} -\frac{\Delta m^2}{4E} \cos 2\theta_{12} + V_e & \frac{\Delta m^2}{4E} \sin 2\theta_{12} & 0 & \mu_{e\mu} \mathcal{B}_\perp \\ \frac{\Delta m^2}{4E} \sin 2\theta_{12} & \frac{\Delta m^2}{4E} \cos 2\theta_{12} + V_\mu & -\mu_{\mu e} \mathcal{B}_\perp & 0 \\ 0 & -\mu_{\mu e} \mathcal{B}_\perp & -\frac{\Delta m^2}{4E} \cos 2\theta_{12} - V_e & \frac{\Delta m^2}{4E} \sin 2\theta_{12} \\ \mu_{e\mu} \mathcal{B}_\perp & 0 & \frac{\Delta m^2}{4E} \sin 2\theta_{12} & \frac{\Delta m^2}{4E} \cos 2\theta_{12} - V_\mu \end{pmatrix}, \quad (2.103)$$

where the magnetic moment is now given by  $\mu_{e\mu} \equiv \mu_{e\mu}^{(-+)} = \mu_{12}$ . It can be seen that due to the anti-symmetry condition (2.95), the diagonal magnetic moments do not appear in the Hamiltonian matrix. Also the Majorana off diagonal magnetic moment are in general different from the Dirac neutrino case (2.100). In this case also there are two possible resonances besides the MSW resonance:

(i) In the channel  $\nu_{eL} \leftrightarrow \bar{\nu}_\mu$ , the resonance occurs for

$$V_e + V_\mu = V_{CC} + 2V_{NC} = \frac{\Delta m^2}{2E} \cos 2\theta_{12}. \quad (2.104)$$

(ii) In the channel  $\nu_{\mu L} \leftrightarrow \bar{\nu}_{eR}$ , the resonance occurs for

$$V_e + V_\mu = V_{CC} + 2V_{NC} = -\frac{\Delta m^2}{2E} \cos 2\theta_{12}. \quad (2.105)$$

Now,  $V_{CC} + 2V_{NC} = \sqrt{2}G_F(n_e - n_n)$  and since  $\cos 2\theta_{12} > 0$ , in a typical astrophysical objects such as the Sun where  $n_n < n_e$ , only the first resonance can occur. The realization of the second resonance requires large number density of neutrons such as those in neutron stars.





---

**Neutrino spin-flavor oscillations in solar environment**

---

In this chapter we study the phenomenon of neutrino spin-flavor oscillations due to solar magnetic fields. This allows us to examine how significantly the electron neutrinos produced in the solar interior undergo a resonant spin-flavor conversion. We construct analytical models for the solar magnetic field in all the three regions of the Sun. Neutrino spin-flavor oscillations in these magnetic fields are examined by studying the level crossing phenomenon and comparing the two cases of zero and non-zero vacuum mixing respectively. Results from the Borexino experiment are used to place an upper limit on the magnetic field in the solar core. Related phenomena such as effects of matter on neutrino spin transitions and differences between Dirac and Majorana transitions in the solar magnetic fields are also discussed.

This chapter is mainly based on the Ref. [78].

### **3.1 Introduction**

The study of solar neutrinos and their oscillation phenomenology has revealed many facets of the physics of neutrinos. The Ray Davis experiment, which started in the 1960's in

Homestake mine, was the first to detect solar neutrinos reaching the Earth. After several years of operation, the experiment reported that there is about a two-third deficit in the observed solar neutrino flux compared to the standard solar model calculation [79]. The deficit was further confirmed by other solar neutrino experiments, notably SAGE, GALLEX and Super-Kamiokande (SK) [80–83]. This discrepancy between the observed rate of neutrino flux and its theoretical prediction is called the solar neutrino problem. One of the ways to resolve the problem was suggested by Pontecorvo on the basis of mixing between different neutrino flavors. He showed that if neutrinos have a non-zero mass then the neutrino flavor mixing will give rise to oscillations among different neutrino flavors [84]. Thus electron neutrinos produced in the Sun may convert to some other flavor of neutrinos on their way to Earth and become undetectable. The problem was finally resolved when the Sudbury Neutrino Observatory(SNO) detected neutrinos from all three flavors in the solar neutrino flux, which proved that there must be transitions among the three active neutrino flavors [85]. However, if vacuum neutrino oscillation alone were responsible for these flavor transitions, one would also be able to detect seasonal variation in the neutrino flux rate due to eccentricity of Earth’s orbit. The  ${}^8B$  neutrino spectrum in the SK experiment exhibited no such variation [86]. The mechanism of flavor transitions that is most favored by data is the adiabatic resonant conversion due to neutrino-matter interactions, also known as the Mikheev-Smirnov-Wolfenstein (MSW) effect. Wolfenstein showed that the coherent forward scattering of neutrinos with electrons, protons and neutrons will induce an additional potential which will modify the effective mass and mixing of neutrinos in the medium [21]. In a medium with variable density, such as the Sun, these matter effects can lead to enhanced transitions between  $\nu_e$  and  $\nu_\mu/\nu_\tau$ , even for small solar mixing angle (MSW-SMA) [23, 24]. However, most of the solar neutrino data, including data from the KamLAND experiment and recent data from the Borexino experiment, have established the large mixing angle (MSW-LMA) solution to the solar neutrino problem [87–91].

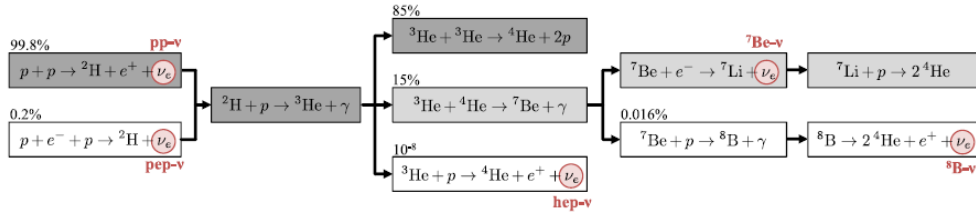


Figure 3.1: Schematic diagram of the solar  $pp$  fusion chain. The neutrinos emitted in different reactions are marked in red. (Figure taken from Ref. [91]).

### 3.1.1 Solar neutrino production and flavor transitions

The neutrinos in the Sun are predominantly produced via the  $pp$ -chain (shown in Fig. 3.1) which can be summarized by the overall reaction

$$4p \rightarrow {}^4\text{He} + 2e^+ + 2\nu_e + 26.7 \text{ MeV}. \quad (3.1)$$

In this reaction two electron neutrinos are emitted for each  ${}^4\text{He}$  nucleus produced in the Sun. These neutrinos, having small interaction cross section, stream freely through the solar plasma and reach Earth in about eight minutes, thus bringing important information about the solar core. From the solar luminosity the resulting solar neutrino flux at the Earth surface can be estimated to be about  $6.6 \times 10^{10} \text{ cm}^{-2}\text{s}^{-1}$ .

The solar  $pp$  chain ( Fig. 3.1) begins with the fusion of two protons to a deuteron via two parallel pathways called  $pp$  and  $pep$  reactions. The deuteron thus produced quickly fuses with proton to form  ${}^3\text{He}$ . From here onward three possible reaction channels open up. Most probable is fusion of two  ${}^3\text{He}$  nuclei to form  ${}^4\text{He}$  ( $pp$ -I branch). The other two lesser probable channels are fusion of  ${}^3\text{He}$  and  ${}^4\text{He}$  to form  ${}^7\text{Be}$  and capture of a proton by  ${}^3\text{He}$  leading to  ${}^4\text{He}$ . The  ${}^7\text{Be}$  produced is finally converted to  ${}^4\text{He}$  via production of either  ${}^7\text{Li}$  ( $pp$ -II branch) or  ${}^8\text{B}$  ( $pp$ -III branch) . The majority of the neutrinos (about 90%) are produced in the primary  $pp$  reaction, with energy  $E \leq 420 \text{ keV}$ . Of the remaining 10% a large fraction of neutrinos are emitted in the electron capture reaction on  ${}^7\text{Be}$  in the  $pp$ -II branch (mono-energetic neutrinos with  $E = 0.862 \text{ keV}$  or  $E = 384 \text{ keV}$ ). Smaller contributions

to the neutrino flux come from the  $pep$  fusion reaction (mono-energetic with  $E = 1.44$  MeV) and from the  ${}^8\text{B}$  decay in the  $pp$ -III branch ( $E \leq 14.6$  MeV). A minuscule fraction of neutrinos with highest energy are also expected to be emitted by proton capture of  ${}^3\text{He}$  ( $hep$  neutrinos), but due to negligible branching ratio of this reaction these neutrinos are beyond current detection sensitivity [88]. The energy spectrum of different components of the solar neutrinos is shown in Fig. 3.2.

Solar neutrinos are produced in the central region (Fig. 3.3), which almost coincides with the energy production region of the Sun [92]. Apart from the  $hep$  neutrinos, the region of production of  $pp$  neutrinos is largest and extends upto  $r \cong 0.25R_\odot$ . The  ${}^8\text{B}$  neutrinos are produced in a comparatively smaller region with  $r \lesssim 0.1R_\odot$ , which plays an important role in their resonant conversion.

It has been conclusively shown by several experiments that neutrinos undergo flavor conversion as they propagate outwards from the solar interiors. This flavor conversion can be characterized by a single function, the survival probability of electron neutrinos [93].

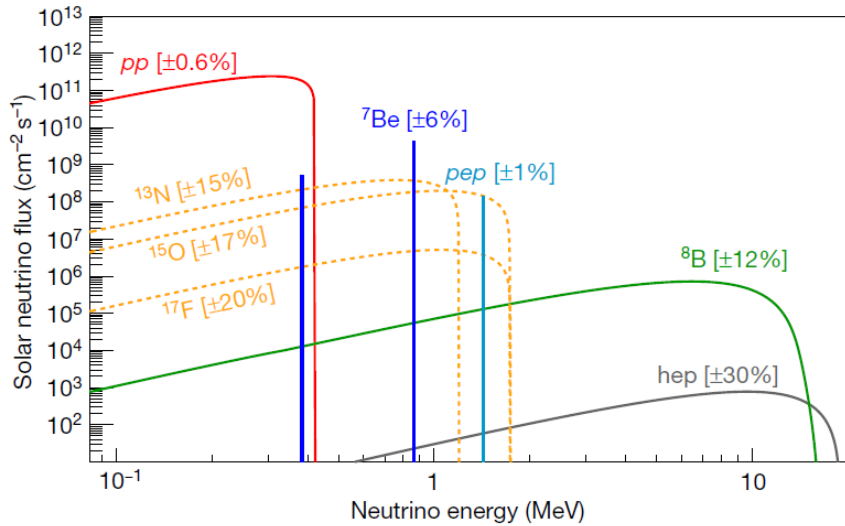


Figure 3.2: Energy spectrum of the solar neutrinos produced in different reactions in the  $pp$  chain. (Figure taken from Ref. [88]).

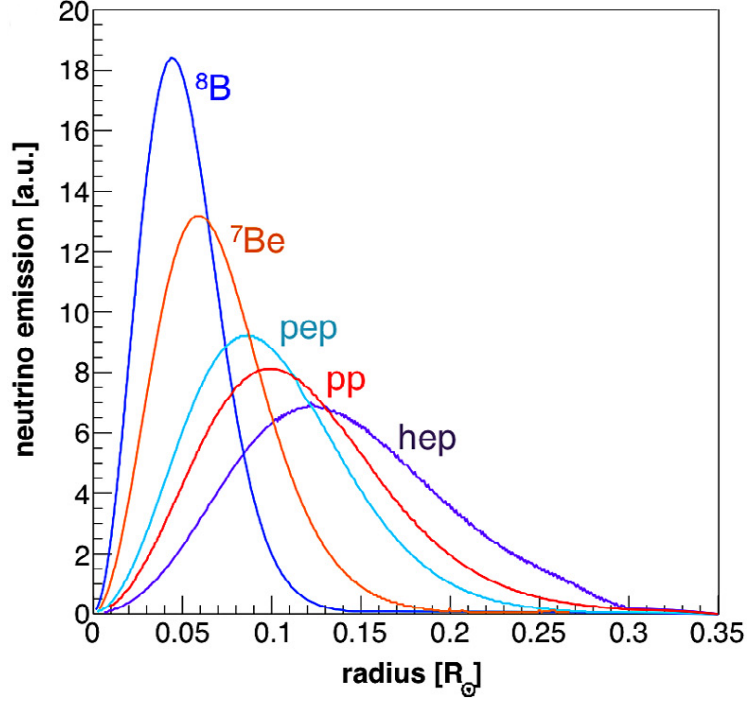


Figure 3.3: Production of different components of the solar neutrinos as a function of distance from the center of the Sun (expressed in units of solar radius  $R_{\odot}$ ). (Figure taken from Ref. [91]).

This probability  $P_{ee}$  is related to the effective two flavor neutrino oscillations by the relation [4, 94]:

$$P_{ee} = \cos^4 \theta_{13} P_{ee}^{2\nu} + \sin^4 \theta_{13} \quad (3.2)$$

The effective Hamiltonian for two neutrino propagation in matter can be written as [19, 93]

$$H = \begin{pmatrix} \frac{\Delta m^2 \cos 2\theta_{12}}{4E} - \frac{\sqrt{2}G_F \cos^2 \theta_{13} n_e}{2} & \frac{\Delta m^2 \sin 2\theta_{12}}{4E} \\ \frac{\Delta m^2 \sin 2\theta_{12}}{4E} & -\frac{\Delta m^2 \cos 2\theta_{12}}{4E} + \frac{\sqrt{2}G_F \cos^2 \theta_{13} n_e}{2} \end{pmatrix}, \quad (3.3)$$

where  $n_e$  is the number density of electrons and  $\Delta m^2 = \Delta m_{21}^2$ . The relative importance of the matter potential term and the vacuum oscillation term in the Hamiltonian can be parametrized by the following term

$$\beta = \frac{2\sqrt{2}G_F \cos^2 \theta_{13} n_e E}{\Delta m^2}, \quad (3.4)$$

which represents the ratio of the neutrino oscillation length in vacuum to the oscillation

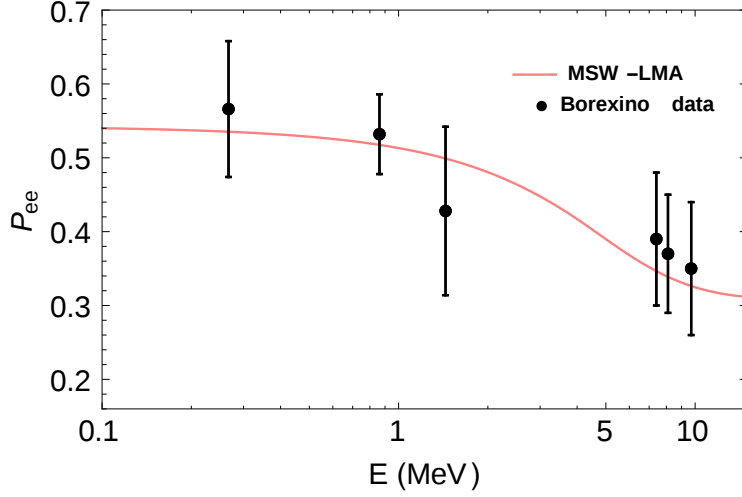


Figure 3.4: The solar  $\nu_e$  survival probability as a function of energy (pink curve) with oscillation parameters obtained in Ref. [20]. The data points with error bars show the Borexino measurements reported in Ref. [88].

length in matter. As the neutrinos travel through the varying density of the Sun, they may go through the MSW resonance condition and then proceed out to the vacuum. If the density variation is sufficiently slow so that the propagation is adiabatic, the neutrino will remain in the same mass eigenstate. In the MSW-LMA scenario the solar  $\nu_e$  daytime survival probability at Earth in the adiabatic limit can be approximated as [19, 93]

$$P_{ee} = \frac{1}{2} \cos^4 \theta_{13} (1 + \cos 2\theta_m \cos 2\theta_{12}), \quad (3.5)$$

where the mixing angle in matter is

$$\cos 2\theta_m = \frac{\cos 2\theta_{12} - \beta}{\sqrt{(\cos 2\theta_{12} - \beta)^2 + \sin^2 2\theta_{12}}}. \quad (3.6)$$

In Fig. 3.4 we plot the energy dependence of the survival probability  $P_{ee}$  for the oscillation parameters  $\Delta m_{21}^2 = 7.5 \times 10^{-5} \text{ eV}^2$  and  $\theta_{12} = 33^\circ$ , which correspond to the LMA solution of the solar neutrino problem. For the low energy neutrinos having  $\beta < \cos \theta_{12} \approx 0.4$ , the survival probability (3.5) has an approximate value

$$P_{ee} \approx \cos^4 \theta_{13} \left(1 - \frac{1}{2} \sin^2 2\theta_{12}\right) \approx 0.55, \quad (3.7)$$

which corresponds to vacuum averaged oscillations. On the other hand, for the high energy neutrinos with  $\beta > 1$ , Eq. (3.5) becomes

$$P_{ee} \approx \cos^4 \theta_{13} \sin^2 \theta_{12} \approx 0.3. \quad (3.8)$$

Thus in this energy region the enhanced conversion due to matter effects leads to about two third deficit in the solar  $\nu_e$  flux, which resolves the solar neutrino problem. As shown in Fig 3.4, for neutrinos with energy 1 MeV, vacuum oscillations are dominant mechanism, while for energies above 5 MeV matter effects are more prominent and the vacuum oscillations are suppressed. In the transition region the survival probability exhibits a strong energy dependence.

### 3.1.2 Spin-flavor precession of solar neutrinos

Another idea that was a popular candidate for the solution of the solar neutrino problem was spin precession of neutrinos in the magnetic field of the Sun. It was shown that if neutrinos have sufficiently large magnetic moment then the solar magnetic field can give rise to spin precession  $\nu_{eL} \rightarrow \nu_{eR}$ , which will cause a deficit in the solar  $\nu_e$  flux [74, 95]. This solution was partly supported by data from the Homestake experiment which observed anticorrelation between the neutrino flux and sunspot activity [96]. However, measurements from other experiments observed no such correlation [83]. Subsequently, the KamLAND experiment ruled out the spin-precession solution by placing a strong constraint on the flux of antineutrinos coming from the Sun [97]. A related effect due to neutrinos having non-zero transition magnetic moments is called resonant spin-flavor precession (RSFP) which results in both spin-flip and flavor change of neutrinos [76, 98]. This effect arises due to the combination of matter and magnetic field on neutrino propagation and is similar to the MSW resonance, and can take place in transverse [98]) as well as longitudinal magnetic fields [77]. Also, the neutrino spin and spin-flavor transitions can give rise to other interesting quantum mechanical effects such as non-vanishing geometric phases [99, 100], which

demonstrate the intimate connection between the geometry of neutrino spin trajectory in the projective Hilbert space and neutrino spin transition probabilities.

Having determined the basic oscillation parameters for solar neutrinos, the present effort is to search for sub-leading effects in the solar neutrino transitions which may give important clues for phenomena beyond the standard model. Various studies have been done to look for effects of non-standard interactions (NSI) [101], dark matter imprints on the neutrino spectrum [102], non-radiative neutrino decay [103] and the combined effect of NSI and spin-flavor precession (SFP) [104]. In this Chapter, we study the possible sub-leading effects caused by spin-flavor transitions due to neutrino propagation in the solar magnetic field.

The neutrino electromagnetic coupling is given by the Hamiltonian  $H_{EM} = \frac{1}{2}\bar{\nu}\mu\sigma_{\mu\nu}\nu F^{\mu\nu} + \text{h.c.}$ , where  $\mu$  is the neutrino magnetic moment matrix. For the case of Dirac neutrinos, the hermicity of the Hamiltonian requires  $\mu^\dagger = \mu$ . On the other hand, for Majorana neutrinos, CPT symmetry requires the magnetic moment matrix to be anti-symmetric, which results in vanishing diagonal magnetic moments [105]. This difference in the magnetic moment matrix gives rise to different spin-flavor transition probabilities for Dirac and Majorana neutrinos. The diagonal magnetic moment for a Dirac neutrino in the minimally extended standard model (MESM) including massive neutrinos is  $\mu_\nu \approx 3.2 \times 10^{-19}(m_\nu/1\text{eV})\mu_B$ , where  $m_\nu$  is the neutrino mass [54, 106]. The off-diagonal magnetic moments for both Dirac and Majorana neutrinos are further suppressed due to GIM mechanism [37]. However, the current best experimental bounds on the neutrino magnetic moment are in the range  $\mu_\nu \leq (2 - 10) \times 10^{-11}\mu_B$  [31, 32, 50]. Thus, the sensitivity of the present experiments is many orders away from the MESM predictions. To bridge this gap, many theoretical models have been postulated which avoid the GIM suppression and predict neutrino magnetic moment in the range  $(10^{-10} - 10^{-14})\mu_B$  (see Section 2.2.2 for details).

In the present work, we examine the effects of magnetic moments  $\sim 10^{-11}\mu_B$  on the solar

neutrino transition probabilities for both the cases of Dirac and Majorana neutrinos. In particular, we first perform calculations for the approximate case of vanishing vacuum mixing and show that the spin-flavor evolution equations can be reduced to a form which admit an exact solution. We then study the actual case of non-zero mixing angle and the effects of the level crossing phenomenon on neutrino transition probabilities and use the results to place bounds on the solar magnetic fields. In the previous work along these lines by various authors [107–114], several bounds have been obtained for both Dirac and Majorana spin-flavor transitions for different magnetic field configurations.

The magnitude of the spin-flavor transitions depend mainly on the strength of the magnetic field at the location of the SFP resonance. This in turn depends on the detailed magnetic field profile of the Sun, which is not very well known, especially in the interior regions of the Sun. In Section 3.2, we discuss current bounds on the solar magnetic field in various regions of the Sun and its effect on neutrino spin polarization. We also discuss the effective two-flavor model for neutrino spin-flavor precession. In Section 3.3, we show that in the approximate case of vanishing mixing angle the resulting set of equations possess analytically exact solutions. We also derive bounds on the solar magnetic fields using the existing experimental results. We then examine the effect of non-zero vacuum mixing on neutrino transition probabilities in Section 3.4 and constrain our theoretical results with the bounds from Borexino experiment in Section 3.5. Finally we discuss the results in the Section 3.6.

## 3.2 Magnetic field in the Sun

The magnetic field in different regions of the Sun exhibits different characteristic behaviors [113]. In the solar convective zone (CZ) the magnetic fields are believed to be generated from a dynamo mechanism active at its base. The current data from helioseismology points

to a thin shear layer at the bottom of the CZ, known as a tachocline, which generates a large-scale toroidal magnetic field. The strength of the magnetic field is predicted to be in the range 10-100 kG [115]. On the other hand, the radiative zone (RZ) magnetic field may have its origin in the formation of the Sun. Once formed, this primordial field might have been frozen in the RZ and the solar core without protruding much into the CZ [116]. The bound on the large-scale toroidal magnetic field in the RZ ranges from 5-7 MG [117] to 30 MG [118]. For the solar core, magnetic field bounds vary widely from 30 G [119] to 7 MG [120].

Based on the above bounds, we choose two profiles to simulate the magnetic field in the Sun. In the first model we implement the field profile given by [121] and add an RZ magnetic field

$$B_{\perp RZ}(r) = B_0 \operatorname{sech}[34.75(r/R_{\odot} - 0.25)]. \quad (3.9)$$

The profile is chosen such that  $B_{RZ}$  in the CZ is negligible compared to the CZ magnetic field and also becomes very small near the solar core. For the second model, we select a field profile which peaks in the solar core and is expressed as

$$B_{\perp}(r) = B_0 \operatorname{sech}(5r/R_{\odot}). \quad (3.10)$$

First we consider the neutrino spin precession as it propagates in the solar magnetic field neglecting the effect of matter and flavor mixing. The change in neutrino spin polarization in this case is described by the equation

$$\frac{d\mathbf{S}}{dr} = 2\mu_{\nu}\mathbf{S} \times \mathbf{B}_{\perp}(r), \quad (3.11)$$

where for  $B_{\perp}$  we apply the two magnetic field profiles in Eqs. (3.9), (3.10) and  $\mu_{\nu} \approx 10^{-11}\mu_B$ . As can be seen in Fig. 3.5, the change in neutrino spin polarization can be sufficient even with peak fields  $\sim 10^4$  G. The change in helicity of solar neutrinos can also affect the  $\nu - e$  scattering [122].

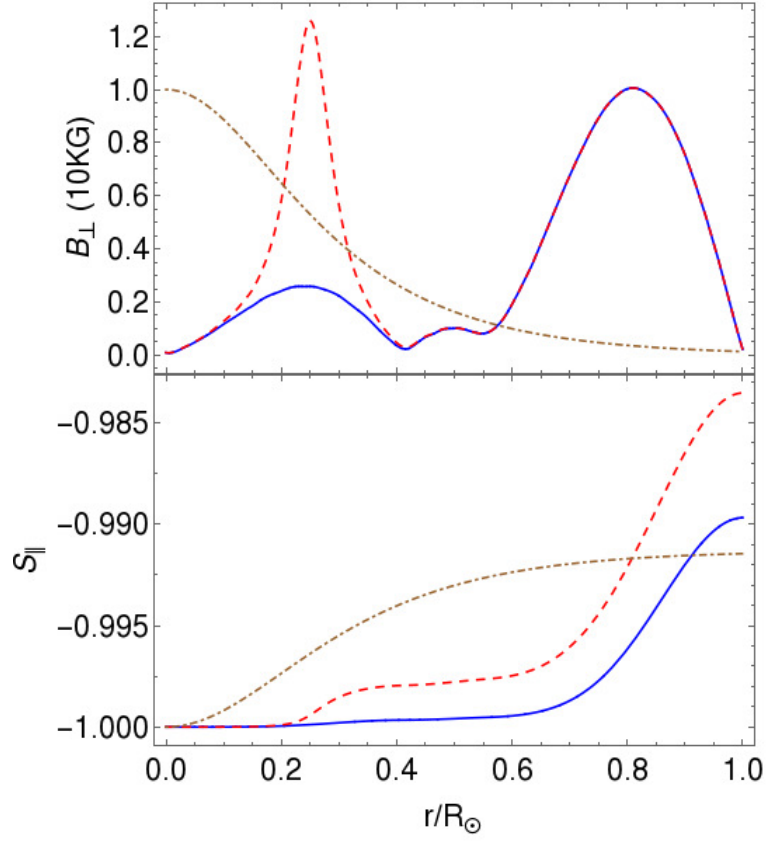


Figure 3.5: The longitudinal neutrino spin polarization  $S_{\parallel}$  as it propagates in the magnetic field of the Sun. The solid curve is the magnetic field obtained by solving solar MHD equations in [121]. The dashed curve is given by Eq. (3.9) and the dot-dashed curve by Eq. (3.10). The peak magnetic field for both models is taken to be  $\approx 10^4$  G.

Now if we include the matter potential term  $V$  which affects left and right helicity states differently, then the neutrino propagation can be described by a Schrödinger-like equation (Eq. (2.74))

$$i \frac{d}{dr} \begin{pmatrix} \nu_L \\ \nu_R \end{pmatrix} = \begin{pmatrix} V(x) & \mu_\nu B_\perp \\ \mu_\nu B_\perp & 0 \end{pmatrix} \begin{pmatrix} \nu_L \\ \nu_R \end{pmatrix}. \quad (3.12)$$

For the case of constant  $V$  and  $B_\perp$ , the change in neutrino helicity is expressed as [31]

$$P_{\nu_L \rightarrow \nu_R}(x) = \frac{(2\mu_\nu B_\perp)^2}{V^2 + (2\mu_\nu B_\perp)^2} \sin^2 \left( \frac{1}{2} \sqrt{V^2 + (2\mu_\nu B_\perp)^2} x \right). \quad (3.13)$$

Thus, matter potential is expected to further suppress the change in neutrino helicity in solar magnetic fields.

Now considering two neutrino flavors, we finally include the effects of neutrino masses and mixing angle  $\theta_{12}$ . In this case, the effective Hamiltonian becomes a  $4 \times 4$  matrix. For the case of Dirac neutrinos, the effective Hamiltonian in the  $(\nu_{eL}, \nu_{\mu L}, \nu_{eR}, \nu_{\mu R})^T$  basis is given by Eq. (2.99):

$$H_D = \begin{pmatrix} -\frac{\Delta m^2}{4E} \cos 2\theta_{12} + V_e & \frac{\Delta m^2}{4E} \sin 2\theta_{12} & \mu_{ee} B_\perp & \mu_{e\mu} B_\perp \\ \frac{\Delta m^2}{4E} \sin 2\theta_{12} & \frac{\Delta m^2}{4E} \cos \theta_{12} + V_\mu & \mu_{\mu e} B_\perp & \mu_{\mu\mu} B_\perp \\ \mu_{ee} B_\perp & \mu_{\mu e} B_\perp & -\frac{\Delta m^2}{4E} \cos 2\theta_{12} & \frac{\Delta m^2}{4E} \sin 2\theta_{12} \\ \mu_{e\mu} B_\perp & \mu_{\mu\mu} B_\perp & \frac{\Delta m^2}{4E} \sin 2\theta_{12} & \frac{\Delta m^2}{4E} \cos 2\theta_{12} \end{pmatrix}, \quad (3.14)$$

where  $V_e = \sqrt{2}G_F(n_e - n_n/2)$  and  $V_\mu = -G_F n_n/\sqrt{2}$  are matter potentials for left handed electron and muon neutrinos respectively,  $n_e$  and  $n_n$  denote the number densities of electrons and neutrons respectively and  $\Delta m^2 = \Delta m_{21}^2$  is the neutrino mass-squared difference. For the Majorana case the vanishing diagonal terms  $\mu_{ee}$  and  $\mu_{\mu\mu}$  result in the following Hamiltonian in the  $(\nu_{eL}, \nu_{\mu L}, \bar{\nu}_e, \bar{\nu}_\mu)^T$  basis (Eq. (2.103)):

$$H_M = \begin{pmatrix} -\frac{\Delta m^2}{4E} \cos 2\theta_{12} + V_e & \frac{\Delta m^2}{4E} \sin 2\theta_{12} & 0 & \mu_{e\mu} B_\perp \\ \frac{\Delta m^2}{4E} \sin 2\theta_{12} & \frac{\Delta m^2}{4E} \cos \theta_{12} + V_\mu & -\mu_{\mu e} B_\perp & 0 \\ 0 & -\mu_{\mu e} B_\perp & -\frac{\Delta m^2}{4E} \cos 2\theta_{12} - V_e & \frac{\Delta m^2}{4E} \sin 2\theta_{12} \\ \mu_{e\mu} B_\perp & 0 & \frac{\Delta m^2}{4E} \sin 2\theta_{12} & \frac{\Delta m^2}{4E} \cos 2\theta_{12} - V_\mu \end{pmatrix}. \quad (3.15)$$

Suppression due to the potential term in the two component case in Eq. (3.13) can now be lifted due to resonant transitions. The electron neutrinos produced in the Sun can undergo multiple resonances in the presence of a magnetic field. The usual MSW resonance  $\nu_{eL} \leftrightarrow \nu_{\mu L}$  takes place at the location  $x_{\text{MSW}}$

$$\left. \frac{\rho(x)Y_e}{m_n} \right|_{x=x_{\text{MSW}}} = \frac{\Delta m^2 \cos 2\theta_{12}}{2\sqrt{2}G_F E}. \quad (3.16)$$

In addition, there is spin-flavor resonance  $\nu_{eL} \leftrightarrow \nu_{\mu R}$  which always occurs before the MSW resonance. The location of the spin-flavor resonance is given by

$$\left. \frac{\rho(x)Y_e^{\text{eff}}}{m_n} \right|_{x=x_{\text{SFP}}} = \frac{\Delta m^2 \cos 2\theta_{12}}{2\sqrt{2}G_F E}, \quad (3.17)$$

where  $\rho(x)$  is matter density inside the Sun,  $m_n$  is the neutron mass,  $Y_e$  is the electron fraction and

$$Y_e^{\text{eff}} = \begin{cases} (3Y_e - 1)/2 & \text{for } \nu_{eL} \leftrightarrow \nu_{\mu R}, \\ (2Y_e - 1) & \text{for } \nu_{eL} \leftrightarrow \bar{\nu}_\mu. \end{cases} \quad (3.18)$$

E (MeV)	$\nu_{eL} \leftrightarrow \nu_{\mu R}$	$\nu_{eL} \leftrightarrow \bar{\nu}_\mu$
2.5	0.057	0.027
5.0	0.156	0.142
10.0	0.230	0.218
15.0	0.268	0.257

Table 3.1: The location of SFP resonance in the Sun (in units  $r/R_\odot$ ) for different neutrino energies.

The location of resonance for different neutrino energies are provided in [Table 3.1](#) using the electron density profile from the solar model BS2005 of Bahcall, Serenelli and Basu [[123](#)]. We have used  $\Delta m^2 = 7.4 \times 10^{-5} \text{ eV}^2$  and  $\theta_{12} = 33.8^\circ$  throughout the Chapter. For neutrinos with energy below 2 MeV, the resonant density required is too high to occur in the Sun. Thus only the high energy  ${}^8\text{B}$  neutrinos are expected to be affected by these effects.

The solutions of the neutrino evolution equation with spin-flavor Hamiltonian ([3.14](#)) and ([3.15](#)) are difficult to solve for arbitrary varying density and magnetic fields. However, analytical [[124](#)] and semi-analytic [[125](#)] solutions exist for different cases. In the next section, we will study the case of zero vacuum mixing which gives rise to equations admitting exact analytical solutions.

### 3.3 An analytical model for zero vacuum mixing

For the case of  $\theta_{12} = 0$ , only the SFP resonance can contribute to the neutrino transitions. In this case the effective Hamiltonian becomes a  $2 \times 2$  matrix in the channel  $\nu_{eL} \leftrightarrow \nu_{\mu R}/\bar{\nu}_{\mu}$ :

$$H = \begin{pmatrix} \frac{-\Delta m^2}{4E} + \frac{\delta V}{2} & \mu_{e\mu} B \\ \mu_{e\mu} B & \frac{\Delta m^2}{4E} - \frac{\delta V}{2} \end{pmatrix}, \quad (3.19)$$

where  $\delta V = \sqrt{2}G_F\rho Y_e^{\text{eff}}/m_N$ , with  $Y_e^{\text{eff}}$  defined by Eq. (3.18). As can be seen from Eq. (3.19), the main input required to study spin-flavor transitions is the profile of number density of electrons and neutrons, and the magnetic field along the neutrino trajectory. The electron number density in the solar model BS(2005) is shown in Fig. 3.6. However, for obtaining numerical solutions various approximations, are applied [65]. Here we use the approximation

$$n_e(r) = 100[1 - \tanh(5r/R_{\odot})]N_A \text{ cm}^{-3}, \quad (3.20)$$

where  $N_A$  is the Avogadro's number, which gives a reasonably good approximation apart from the region near the surface of the Sun.

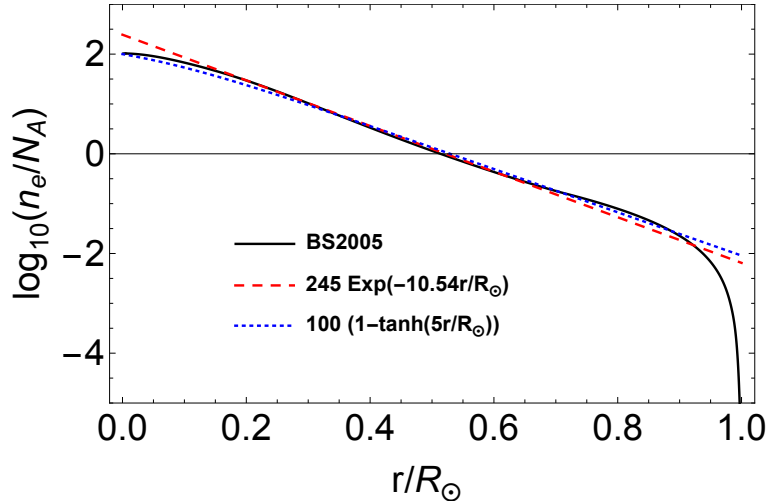


Figure 3.6: Electron number density variation vs. radial distance in the Sun. The *solid line* represents the solar model BS(2005) and the *dashed curves* are analytical approximations.

Now the equation for the neutrino flavor  $\nu_{eL}$  with Hamiltonian (3.19) becomes a second order ordinary differential equation given by

$$\frac{d^2\nu_{eL}}{dt^2} - \left( \frac{\mu\dot{B}}{\mu B} + i\xi \right) \frac{d\nu_{eL}}{dt} + \left( \phi^2 + i\frac{d\phi}{dt} + (\mu B)^2 - i\phi\frac{\mu\dot{B}}{\mu B} + \phi\xi \right) \nu_{eL} = 0, \quad (3.21)$$

where we have defined

$$\phi = -\frac{\Delta m^2}{4E} + \frac{1}{\sqrt{2}}G_F n_e, \quad (3.22)$$

$$\xi = \begin{cases} -\frac{1}{\sqrt{2}}G_F n_n & \text{for } \nu_{eL} \rightarrow \nu_{\mu R}, \\ -\sqrt{2}G_F n_n & \text{for } \nu_{eL} \rightarrow \bar{\nu}_{\mu}. \end{cases} \quad (3.23)$$

In general, it is possible to solve this equation numerically to obtain the survival probability of electron neutrinos. However for the case when magnetic field is given by Eq. (3.10) and density is expressed by Eq. (3.20), the set of equations reduces to the well-known Demkov-Kunike model, which has exact solutions [126, 127]. The analytical solution is provided by Eq. (B.15) and can be used to calculate the neutrino transition probability  $P(\nu_{eL} \rightarrow \bar{\nu}_{\mu R}; R_{\odot})$ . The resulting solution plotted in Fig. 3.7 depicts the difference for the two cases of Dirac and Majorana neutrinos. For sufficiently low magnetic fields, the difference in the transition probability of the two cases is not significant. However, for large magnetic field there can be a detectable difference in the Dirac and Majorana neutrinos.

If we assume that inside the Sun the transitions are driven dominantly by SFP resonance, and that outside the Sun the transitions are mainly due to the large vacuum mixing angle, then the probability for the electron neutrinos produced inside the Sun to reach the Earth's surface as electron antineutrinos is given by [108]

$$\begin{aligned} P(\nu_e \rightarrow \bar{\nu}_e) &= P(\nu_{eL} \rightarrow \bar{\nu}_{\mu R}; R_{\odot}) P(\bar{\nu}_{\mu R} \rightarrow \bar{\nu}_{eR}; R_{es}) \\ &= P(\nu_{eL} \rightarrow \bar{\nu}_{\mu R}; R_{\odot}) \sin^2 2\theta_{12} \sin^2 \left( \frac{\Delta m^2 R_{es}}{4E} \right), \end{aligned} \quad (3.24)$$

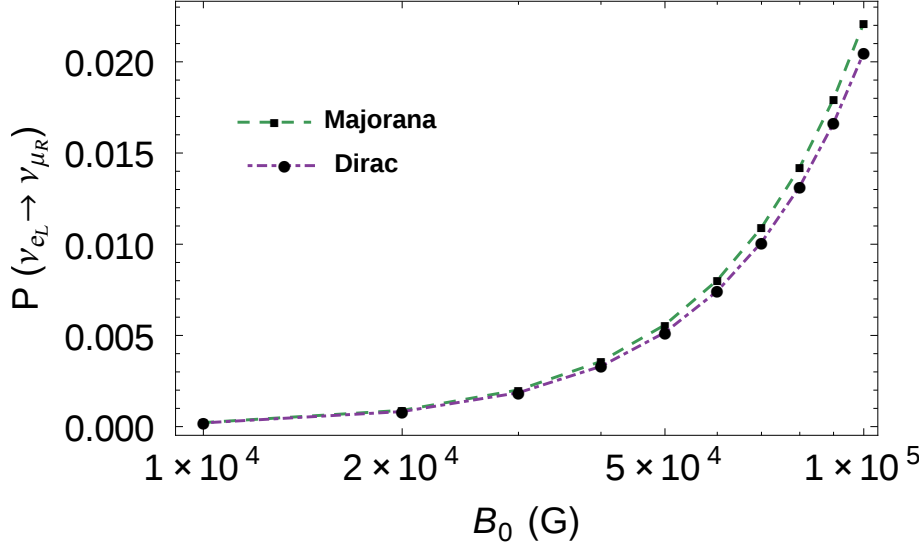


Figure 3.7: Transition probability of Dirac and Majorana neutrinos obtained from the solution of equation (3.21). Here the neutrinos are assumed to be produced at the center of the Sun with energy  $E = 10$  MeV.

where  $R_{es}$  is the average distance between Earth and Sun.

For the above model, the result from the Borexino experiment can be used to obtain bounds on the maximum magnetic field  $B_0$  at the center of the Sun. The Borexino experiment gives an upper limit on the neutrino transition probability for  ${}^8B$  neutrinos  $P_{\nu_e \rightarrow \bar{\nu}_e} < 1.3 \times 10^{-4}$  at 90% C.L. for  $E_{\bar{\nu}} > 1.8$  MeV [128].

Now the transition probability  $P(\nu_{eL} \rightarrow \bar{\nu}_{\mu R}; R_{\odot})$  in Eq. (3.24) is obtained from Eq. (B.15) by averaging over the  ${}^8B$  neutrino production region in the Sun [123]. Using this, we calculate the the mean probability in the energy region ( $2 < E < 15$ ) MeV with 1 MeV/bin. For Majorana neutrinos we obtain  $\langle P \rangle = 1.18 \times 10^{-4}$  for  $B_0 = 3 \times 10^4$  G and  $\langle P \rangle = 2.1 \times 10^{-4}$  for  $B_0 = 4 \times 10^4$  G. Whereas for the case of Dirac neutrinos we obtain  $\langle P \rangle = 1.0 \times 10^{-4}$  for  $B_0 = 3 \times 10^4$  G and  $\langle P \rangle = 1.8 \times 10^{-4}$  for  $B_0 = 4 \times 10^4$  G. Thus the consistency with the Borexino result requires  $B_0 \leq 3 \times 10^4$  G in both cases. Hence, this analysis presents us a useful bound on the magnetic field in the solar core. This bound lies in between the various other bounds discussed in the previous section. However, this limiting case obtained by substituting  $\theta_{12} = 0$  inside the solar region over estimates the transition probability by pushing the SFP resonance deeper into the solar interior where the

strength of the magnetic field is higher. Thus we expect the actual bound on the magnetic field to be higher in the full treatment with all the flavors taken into consideration.

For the case when magnetic field is given by Eq. (3.9) in the RZ of the Sun, such analytical solutions of Eq. (3.21) are not possible. In this case, since the magnetic field is significantly weaker at the SFP location, we do not expect significant transitions. Hence, the bounds on the RZ magnetic field will be comparatively weaker.

### 3.4 Including effects of $\theta_{12}$

Adding the effects of the vacuum mixing leads to the full Hamiltonian (3.14) and (3.15) for Dirac and Majorana neutrinos respectively. However, since there is no resonant production of  $\nu_{eR}/\bar{\nu}_e$ , we set its amplitude to zero which yields the effective  $3 \times 3$  Hamiltonian for the Majorana neutrinos

$$H_M = \begin{pmatrix} \frac{-\Delta m^2}{4E} \cos 2\theta_{12} + V_e & \frac{\Delta m^2}{4E} \sin 2\theta_{12} & \mu B_{\perp} \\ \frac{\Delta m^2}{4E} \sin 2\theta_{12} & \frac{\Delta m^2}{4E} \cos \theta_{12} + V_{\mu} & 0 \\ \mu B_{\perp} & 0 & \frac{\Delta m^2}{4E} \cos 2\theta_{12} - V_{\mu} \end{pmatrix}, \quad (3.25)$$

and a similar one for the Dirac neutrinos. In this case, we have two resonances described by Eqs. (3.16) and (3.17). However at the location of both resonances, the Hamiltonian is dominated by large off-diagonal term  $\Delta m^2 \sin 2\theta_{12}/4E$ . Thus merely fulfilling the SFP resonant condition in Eq. (3.17) is not sufficient to drive large transitions due to the magnetic field. In this case, it is more appropriate to go to mass eigenbasis where such large vacuum mixing terms are absent [113]. The Hamiltonian in the mass eigenbasis can be obtained by performing a rotation on the flavor eigenstates

$$H_M \rightarrow R_{12}^{\dagger} H_M R_{12}, \quad (3.26)$$

and diagonalizing the resultant matrix, where  $R_{12}$  is the rotation matrix in the (12) plane.

We obtain

$$H_M^D = \begin{pmatrix} \Delta_D & 0 & \mu B \cos \theta_D \\ 0 & -\Delta_D & \mu B \sin \theta_D \\ \mu B \cos \theta_D & \mu B \sin \theta_D & -\kappa_M \end{pmatrix}, \quad (3.27)$$

where

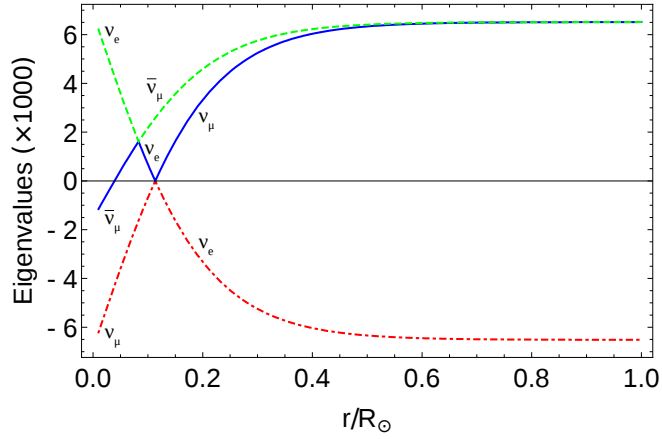
$$\Delta_D = \sqrt{\left(-\frac{\Delta m^2}{4E} \cos 2\theta_{12} + \frac{1}{\sqrt{2}} G_F n_e\right)^2 + \left(\frac{\Delta m^2}{4E} \sin 2\theta_{12}\right)^2}, \quad (3.28)$$

$$\theta_D = -\frac{1}{2} \tan^{-1} \left( \frac{\frac{\Delta m^2}{4E} \sin 2\theta_{12}}{-\frac{\Delta m^2}{4E} \cos 2\theta_{12} + \frac{1}{\sqrt{2}} G_F n_e} \right), \quad (3.29)$$

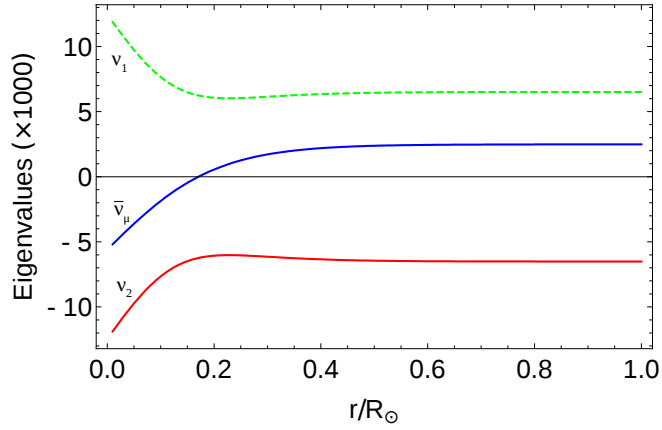
$$\kappa_M = -\frac{\Delta m^2}{4E} \cos 2\theta_{12} + \frac{1}{\sqrt{2}} G_F (n_e - 2n_n). \quad (3.30)$$

In Fig. 3.8 we plot the eigenvalues of the Majorana Hamiltonian Eqs. (3.25) and (3.27) in flavor and mass basis respectively. In the flavor basis, depicted in Fig. 3.8a, one can see the level crossing at two different points. The lower one corresponds to SFP resonance while the higher one is the MSW resonance. The electron neutrinos are produced predominantly in the heavier mass eigenstate (dashed curve in Fig. 3.8a). At the SFP crossing point, the transition between the neutrino states  $\nu_e \leftrightarrow \bar{\nu}_\mu$  is driven by the strength of the magnetic field at the location of the level crossing. Assuming the level crossing to be adiabatic, the  $\nu_e$  eigenstate is now represented by the solid curve in Fig. 3.8a while the dashed curve corresponds now to  $\bar{\nu}_\mu$ . The electron neutrino then goes through another resonance at the MSW crossing point. After this second level crossing, the  $\nu_e$  state now corresponds to the dot-dashed curve which is the lower mass eigenstate while  $\nu_\mu$  is the upper mass eigenstate (solid curve).

However, this notion of resonant flavor conversion is valid only for small mixing angles [129]. For large values of mixing angle, the mass eigenbasis describes the situation more accurately. Comparing Fig. 3.8a and 3.8b, it is seen that the level crossing which was present for the case  $\theta_{12} \approx 0$  is now absent. Again, if the electron neutrinos are produced



(a)



(b)

Figure 3.8: Eigenvalues of the Hamiltonian for  $E = 10$  MeV neutrinos: (a) in the flavor basis, Eq. (3.25) for  $\theta_{12} \approx 0$ . The two level *crossing points* correspond to SFP and MSW resonances. (b) in the mass eigenbasis, Eq. (3.27) for  $\theta_{12} = 33.8^\circ$ . The *dashed/dot-dashed lines* correspond to  $\nu_1/\nu_2$  respectively and the solid line represents  $\bar{\nu}_\mu$ . Here we have used  $B_0 = 10^6$  G and the eigenvalues are in dimensionless units.

in the heavier mass eigenstate (dashed curve in Fig. 3.8b), they now will not encounter any level crossing resonance such as those in Fig. 3.8a. Thus merely fulfilling the resonant conditions in Eqs. (3.16) and (3.17) is not sufficient for resonant conversion and these conditions are valid only for small mixing angle. A general condition for resonant conversion can also be derived which holds for both small and large mixing angles [113].

An examination of the neutrino transitions as it propagates in the Sun reveals further details about the neutrino evolution in this general case. Working with Hamiltonian (3.27) we can

see at the point of neutrino production near the solar core the diagonal terms are  $\Delta_D \sim 4 \times 10^{-12}$  eV for  $E = 10$  MeV, while the magnetic field term  $\mu B \sim 6 \times 10^{-16}$  eV for  $B \sim 10^4$  G. Thus there is a difference of about four orders of magnitude and the transitions will be absent. As the neutrino propagates to the lower density regions in the RZ, the eigenlevels come closer. At  $r \approx 0.2R_\odot$  we have  $\Delta_D \sim 2 \times 10^{-12}$  eV while the magnetic field now increases to about  $10^6$  G, thus  $\mu B \sim 6 \times 10^{-14}$  eV. There is still a difference of about an order of magnitude, however now there can be small  $\nu_{eL} \leftrightarrow \bar{\nu}_\mu$  transitions driven by the magnetic field as can be ascertained in Fig. 3.9. These conversions persist as long as the ratio  $\Delta_D/\mu B \sim 0.1$ . However beyond  $r = 0.4R_\odot$ , the magnetic field gradually falls off to values  $< 10^5$  G (see Fig. 3.5), and the corresponding transitions also die out. Thus after the partial conversion of the neutrinos  $\nu_e \rightarrow \bar{\nu}_\mu$  in the region  $r \approx (0.2 - 0.4)R_\odot$ , the neutrino reverts back to being predominantly in the eigenstate  $\nu_1$ . As the neutrinos propagate towards the CZ, they will again encounter an increasing magnetic field. However due to the strong bounds on the magnetic field in this region having peak field  $B_0 < 10^5$  G, the diagonal splitting terms  $\Delta_D \gg \mu B$  and there will be no significant transitions due to magnetic fields. Thus assuming the neutrinos are produced in the eigenstate  $\nu_1$  in the Sun, they will exit the Sun in the same eigenstate and buried magnetic field in the RZ having strength  $\sim 10^6$  G is not sufficient to cause any appreciable level crossing. Thus the transitions are suppressed to a great extent.

We can write the neutrino transition probability

$$P(\nu_{eL} \rightarrow \bar{\nu}_{\mu R}) = \sum_i P(\nu_{eL} \rightarrow \nu_i) P(\nu_i \rightarrow \bar{\nu}_{\mu R}), \quad (3.31)$$

where  $P(\nu_{eL} \rightarrow \nu_i)$  is the probability that the electron neutrino is produced in mass eigenstate  $\nu_i$  and  $P(\nu_i \rightarrow \bar{\nu}_{\mu R})$  is the probability of transition  $\nu_i \rightarrow \bar{\nu}_{\mu R}$  under the effect of magnetic field. Since the Hamiltonian in Eq. (3.27) for the Majorana neutrinos can be

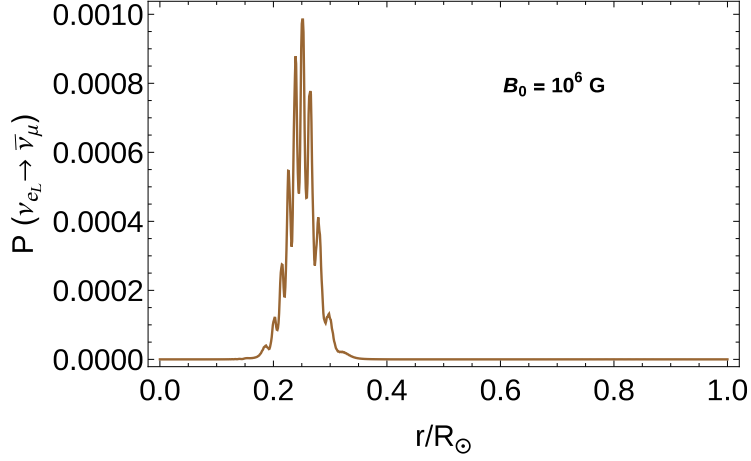


Figure 3.9: The variation of probability  $P(\nu_{eL} \rightarrow \bar{\nu}_{\mu R})$  with distance inside the Sun for maximum RZ magnetic field  $B_0 = 10^6$  G. The neutrinos are assumed to be produced at the center of the Sun and  $E = 10$  MeV.

effectively decoupled into two  $2 \times 2$  blocks, we can write

$$P(\nu_{eL} \rightarrow \bar{\nu}_{\mu R}) = \cos^2 \theta_D(r_i) P(\nu_1 \rightarrow \bar{\nu}_{\mu R}) + \sin^2 \theta_D(r_i) P(\nu_2 \rightarrow \bar{\nu}_{\mu R}), \quad (3.32)$$

where  $\theta_D(r_i)$  is the mixing angle at the neutrino production point  $r_i$ . The probabilities  $P(\nu_i \rightarrow \nu_{\mu R})$  can be evaluated numerically to give the total transition probability in Eq. (3.32).

### 3.5 Comparison with Borexino results

The most stringent constraints on the anti-neutrino flux are given by the Borexino experiment [128], which reported an upper limit of  $\phi_{\bar{\nu}_e} < 760 \text{ cm}^{-2} \text{ s}^{-1}$  on the  ${}^8B$  flux. For an undistorted  ${}^8B$  neutrino spectrum, the solar anti-neutrino flux at the surface of Earth is given by

$$\phi_{\bar{\nu}_e} = \phi_{\nu_e}({}^8B) P(\nu_e \rightarrow \bar{\nu}_e), \quad (3.33)$$

where the value of total  ${}^8B$  neutrino flux is  $\phi_{\nu_e}({}^8B) = 5.88 \times 10^6 \text{ cm}^{-2} \text{ s}^{-1}$  [128]. Thus Borexino placed an upper bound of  $P(\nu_e \rightarrow \bar{\nu}_e) < 1.3 \times 10^{-4}$ .

The solar electron neutrino transition probability  $P(\nu_e \rightarrow \bar{\nu}_e)$  at the Earth's surface can be calculated using Eq. (3.24), where  $P(\nu_{eL} \rightarrow \bar{\nu}_{\mu R}; R_\odot)$  is numerically evaluated using Eq. (3.32) and is averaged over the  ${}^8B$  neutrino production region in the Sun [123]. To put appropriate bounds on the solar magnetic field, we plot in Fig. 3.10 the probability  $P(\nu_e \rightarrow \bar{\nu}_e)$  against the peak magnetic field for the case of Majorana Hamiltonian (3.25). The two curves in Fig. 3.10 correspond to the two magnetic field profiles shown in Fig. 3.5, one peaking at the center of the Sun and other in the RZ, in accordance with the existing helioseismological bounds. In Fig. 3.10, we also show that the Borexino limit [128] intersects the two curves at points corresponding to the maximum allowed peak magnetic field. For the first case when the magnetic field peaks in the RZ, using the Borexino limit we obtain the value of peak magnetic field  $B_0 < 2.1 \times 10^8$  G. Thus the Borexino data is unable to constrain the existing bound of  $B_0 < 30$  MG in the solar RZ, which corresponds

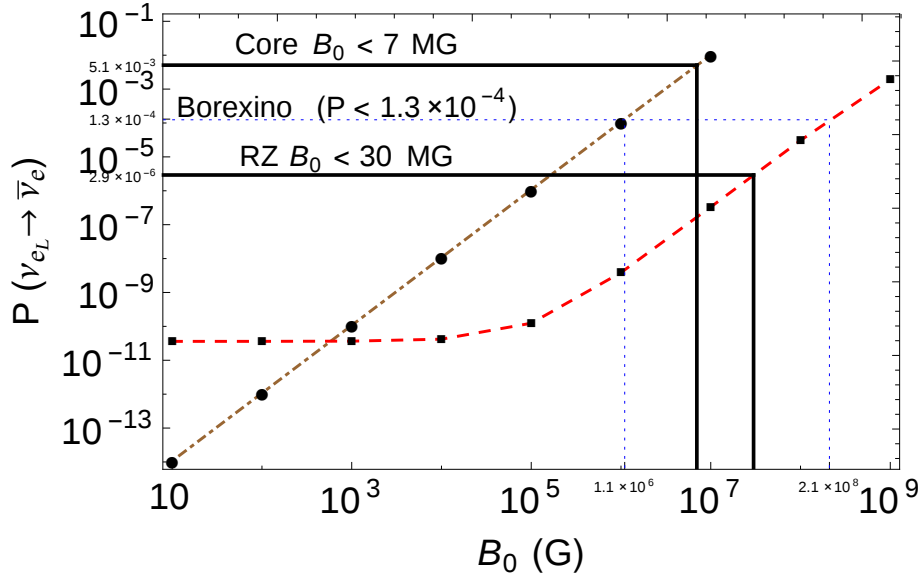


Figure 3.10: The probability of solar electron neutrino ( $E = 10$  MeV) to anti-neutrino conversion at the Earth's surface (Eq. (3.24)) and comparison with Borexino results. The *dashed(red) curve and dotdashed(brown) curve* show the probability  $P(\nu_e \rightarrow \bar{\nu}_e)$  calculated using the two field profiles marked with respective curves in Fig. 3.5. The *dotted(blue) line* signifies that the current upper bound  $P(\nu_e \rightarrow \bar{\nu}_e) < 1.3 \times 10^{-4}$  from the Borexino experiment corresponds to a bound of  $2.1 \times 10^8$  G on the RZ magnetic field and to a bound of  $1.1 \times 10^6$  G on the core magnetic field. The *solid(black) lines* mark the helioseismological bounds of 30 MG and 7 MG on the RZ and solar core magnetic fields respectively.

to the probability  $P(\nu_e \rightarrow \bar{\nu}_e) < 2.9 \times 10^{-6}$  and hence to an upper limit  $\phi_{\bar{\nu}_e} < 17 \text{ cm}^{-2} \text{ s}^{-1}$  of the anti-neutrino flux. This requires an improvement by almost two orders of magnitude in the sensitivity of  $\bar{\nu}_e$  detection. However, the same analysis with magnetic field peaking in the solar core provides very useful bounds which constrain some of the existing solar models. The Borexino limit in this case yields an upper bound of  $B_0 < 1.1 \times 10^6 \text{ G}$ , which is almost a factor of one-seventh of the current largest bound on the core magnetic field [120]. It is useful to compare this result with that obtained in Section 3.3, where we obtained much stronger bound of  $B_0 < 8 \times 10^4 \text{ G}$ . This demonstrates that the two component approximation used frequently (e.g. [130]) does not give the correct transition probability and it is more appropriate to take into account all possible channels in which the initially produced neutrino state may undergo resonant conversion.

Since the Borexino experiment continues to take data, it is natural to assume that future results will be able to place more stringent limits on the anti-neutrino flux. This in turn will be useful for placing stricter upper bounds on the solar magnetic field, especially in the solar core region where current helioseismological bounds vary widely in predictions.

## 3.6 Conclusions

In this Chapter, we have studied the phenomenon of neutrino spin-flavor oscillations in the Sun for neutrinos having sufficiently large magnetic moments  $\sim 10^{-11} \mu_B$ . We have constructed two models for solar magnetic field based on the current bounds on the magnetic field in different regions of the Sun. In the first model, one can have large magnetic field in the solar core and it tapers off with distance from the center. In the second model, we have a large magnetic field in the RZ which becomes negligible in the core region and in addition there is a CZ magnetic field, calculated in [121]. It was shown that even a magnetic field  $\sim 10^4 \text{ G}$  is sufficient to change the neutrino helicity as it comes out of the Sun.

We have also obtained a novel parametrization for the electron density profile in the Sun, which provides a better approximation compared to the usual exponential parametrization.

For the case of zero vacuum mixing and large magnetic field in the solar core, we obtain analytically exact solutions. This allows us to put strong bounds on the magnetic field in the solar core using results from the Borexino experiment. Also, the difference between the Dirac and Majorana neutrinos is significant only for magnetic fields  $\sim 10^5$  G or more. We then examined the effects for the realistic case of large vacuum mixing angle and found that it has an effect in suppressing the  $\nu_e \rightarrow \bar{\nu}_\mu$  transitions. The energy level diagrams distinctly demonstrate the difference between the two cases. Whereas in the case of small mixing angle we get enhanced transitions due to adiabatic level crossings. For the latter case of large vacuum mixing, the eigenstates of the Hamiltonian in the mass eigenbasis do not exhibit such crossing phenomenon. Thus the dominant terms are the diagonal terms and small transitions take place only in the RZ where the ratio of the two terms is  $\sim 0.1$ . Furthermore, the CZ fields do not affect the neutrino transitions. The Borexino results are then utilized to place appropriate bounds on the two models of solar magnetic field. It is found that whereas the Borexino bounds are too weak to place any upper limit on the RZ magnetic field, for the solar core magnetic field we are able to place an upper bound  $B_0 < 1.1 \times 10^6$  G. This is significant improvement over the existing bounds coming from helioseismology results.

Based on the above results it can be seen that while the sub-leading effects on solar neutrinos due to spin-flavor transitions are likely to be very small for  $\mu_\nu \sim 10^{-11} \mu_B$ , with improved sensitivity, the future experiments will be able to place even stronger constraints on the neutrino magnetic moment as well as solar magnetic field. Thus the phenomenon of spin-flavor oscillations gives important information about the solar interior independent of helioseismological observations.





---

## CHAPTER 4

---

# Neutrino propagation in magnetic fields and geometric phases

---

In this Chapter, we show that neutrino spin and spin-flavor transitions involve non vanishing geometric phases. The geometric character of neutrino spin rotation is explored by studying the neutrino spin trajectory in the projective Hilbert space representation and its relation to the geometric phase. Analytical expressions are derived for noncyclic geometric phases. Several calculations are performed for different cases of rotating and non rotating magnetic fields in the context of solar neutrinos and neutrinos produced inside neutron stars. Also the effects of adiabaticity, critical magnetic fields and cross boundary effects in the case of neutrinos emanating out of neutron stars are examined. The variation of geometric phase with magnetic field parameters is shown and its phenomenological implications are discussed.

First we give a general introduction of the pure state geometric phase [131]. Then detailed calculations are done, which show the emergence of geometric phase as the neutrinos propagate in magnetic fields. This Chapter is based on Refs. [99] and [100].

## 4.1 Introduction

The concept of geometric phase emerges from the idea that the phase factor acquired by the wavefunction of a quantum system undergoing evolution has a part that is dynamical and a part that is path dependent or geometric in nature. Berry in his seminal paper [132] showed that for systems undergoing cyclic, adiabatic evolution this path-dependent geometric phase can have observable consequences. The phenomena of geometric phase emerges in a wide range of classical and quantum systems and dates back to the work of Pancharatnam [133] who demonstrated that when a polarized light is passed through a series of polarizers such that initial polarization is finally restored, the final polarized state acquires an additional phase. This additional phase is equal to half the solid angle subtended by the curve representing the polarization states on a Poincaré sphere. The geometric phase since then has been experimentally observed in a wide range of systems such as molecular physics [134], neutron spin rotation [135], photon propagation in helically wound optical fiber [136], and is a source of numerous investigations in physics [137]. In the field of particle physics, in addition to neutrinos, the importance of geometric phase has been explored in the context of super-symmetric quantum mechanics [138], CPT (Charge conjugation, Parity and Time reversal) violation in meson systems [139], and axion-photon mixing [140].

The geometric phase is an example of the phenomenon called holonomy in which some variables fail to return to their initial value when other variables or parameters characterizing the system undergo a cyclic evolution. A simple case of classical holonomy is the parallel transport of a vector around a closed circuit on a curved surface. The parallel transport of vector can be accomplished by requiring that it moves in such a way that its magnitude remains constant and that it does not rotate locally about an axis perpendicular to the surface. As a result of this parallel transport the vector comes back to its initial position rotated by *an angle* which depends only the path traced by the vector and is purely

geometric quantity. For example, consider the case of vector parallel transport around a closed curve  $C$  on a sphere. In this case the angle holonomy obtained is equal to the solid angle subtended by  $C$  at the center of the sphere (Fig. 4.1).

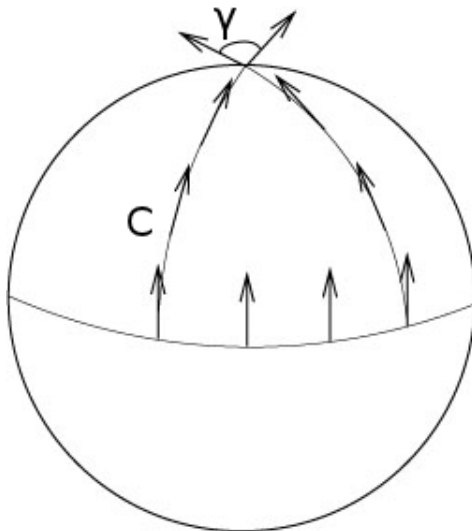


Figure 4.1: Parallel transport on the surface of a sphere. The vector, initially located at the north pole, is parallel-transported along the path  $C$ . As it returns to initial position, it gets rotated by an amount  $\gamma$  that depends on the path  $C$  traversed by the vector.

The concept of parallel transport and holonomy associated with the curve can be extended to quantum regime. In quantum mechanics the state of a system is represented by the vector  $|\psi(\mathbf{x})\rangle \in \mathcal{H}$ , where  $\mathcal{H}$  denotes the Hilbert space and  $\mathbf{x} = (x_1, x_2, \dots)$  denotes the set of parameters governing the system. The rule for parallel transport of  $|\psi(\mathbf{x})\rangle$  along a curve in the parameter space  $\mathbf{x}$  is obtained by two conditions: (i) the length of  $|\psi(\mathbf{x})\rangle$  is preserved and (ii)  $|\psi(\mathbf{x})\rangle$  and  $|\psi(\mathbf{x} + d\mathbf{x})\rangle$  have the same phase i.e.  $\langle \psi(\mathbf{x}) | \psi(\mathbf{x} + d\mathbf{x}) \rangle$  is real and positive. Expanding  $\langle \psi(\mathbf{x}) | \psi(\mathbf{x} + d\mathbf{x}) \rangle$  in Taylor series, we get

$$\langle \psi(\mathbf{x}) | \psi(\mathbf{x} + d\mathbf{x}) \rangle = \langle \psi(\mathbf{x}) | \psi(\mathbf{x}) \rangle + \langle \psi(\mathbf{x}) | \nabla_{\mathbf{x}} | \psi(\mathbf{x}) \rangle \cdot d\mathbf{x} + O(dx^2). \quad (4.1)$$

Thus the above two conditions imply

$$\Im \langle \psi | d\psi \rangle = 0. \quad (4.2)$$

However, if  $|\psi\rangle$  is parallel-transported along a closed curve  $C$  in the parameter space and comes back with a changed phase i.e.

$$\langle \psi_{\text{initial}} | \psi_{\text{final}} \rangle = e^{i\gamma[C]}, \quad (4.3)$$

then this phase change  $\gamma[C]$  arises due to holonomy and is the geometric phase associated with  $C$ . Quantum mechanically, adiabatic change provides the simplest way to parallel transport the vectors over the parameter space. The resulting geometric phase is acquired because of the underlying curvature of the parameter space.

### 4.1.1 Adiabaticity and Berry's Phase

In quantum mechanics the notion of adiabaticity arises whenever the parameters governing a system change sufficiently slowly with time. For such systems using adiabatic approximation [141, 142], the solutions of the Schrödinger equation can be approximated by that of stationary eigenstates of the instantaneous Hamiltonian. For example, if the system is initially in the  $n$ th eigenstate of the slowly changing Hamiltonian  $\hat{H}(t)$  then the eigenvalue equation

$$\hat{H}(t) |n(t)\rangle = E_n(t) |n(t)\rangle, \quad (4.4)$$

can be solved at each instant of time to give the eigenstate  $|n(t)\rangle$  corresponding to energy eigenvalue  $E_n$ , so that the system remains in the  $n$ th eigenstate.

Consider an adiabatically varying Hamiltonian, whose parameters return to their initial value after time  $\tau$  so that  $\hat{H}(t + \tau) = \hat{H}(t)$ . If  $|\psi(0)\rangle$  is the initial eigenstate of  $\hat{H}$  then adiabatic evolution ensures that after time  $\tau$  system remains in the same eigenstate i.e.

$$|\psi(\tau)\rangle = e^{i\alpha} |\psi(0)\rangle, \quad (4.5)$$

where  $\alpha$  is the phase acquired during the evolution. Let us first consider the simple case of time-independent system (having arbitrary periodicity), for which the eigenstates of the Hamiltonian are given by

$$|\psi(\tau)\rangle = e^{-iE\tau} |\psi\rangle, \quad (4.6)$$

where  $|\psi\rangle$  is the solution of time-independent Schrödinger equation corresponding to energy eigenvalue  $E$ . In this case the phase acquired by the eigenstate is just the dynamical phase i.e.  $\alpha = \gamma_d$ , where  $\gamma_d = -E\tau$ . Thus for the general case of time-dependent Hamiltonians one might expect that the phase acquired by the eigenstates for the cyclic evolution is just the generalization of the dynamical phase i.e.

$$\alpha = - \int_0^\tau E(t) dt = \gamma_d \quad (4.7)$$

However, it was shown by Berry [132] that for this case  $\alpha = \gamma_d + \gamma(C)$ , where  $\gamma(C)$  is a non-integrable phase factor that depends on the path  $C$  traversed by the state  $|\psi\rangle$  in the parameter space. While,  $\gamma_d$  gives the information about the duration of evolution of the system,  $\gamma(C)$  gives information about the geometry of the circuit  $C$  in the parameter space. In terminology of the last section,  $\gamma_d$  arises due to local rotation of the state vector, while  $\gamma[C]$  is the holonomy due to parallel transport of the vector around  $C$ .

To this end, we consider the Hamiltonian of a system  $\hat{H} = \hat{H}(x(t))$  depending on a set of slowly varying parameters  $x = (x_1, x_2, \dots)$ . Assuming the energy spectrum of Hamiltonian to be discrete and non degenerate for all  $t$ , we can construct a basis set  $\{|n(t)\rangle\}$  consisting of normalized eigenvectors of  $\hat{H}$ . In the adiabatic approximation, if system is initially defined by the state  $|\psi(x(0))\rangle = |n(x(0))\rangle$  then at time  $t$  it continuously goes over to the state  $|n(x(t))\rangle$ , apart from phase factors. We make an ansatz

$$|\psi(x(t))\rangle = e^{i\gamma_n} e^{-i \int_0^t E(t') dt'} |n(x(t))\rangle, \quad (4.8)$$

where, the second phase factor is the dynamical phase and  $\gamma_n$  is some additional phase.

Substitution in Schrödinger equation

$$i \frac{d}{dt} |\psi(\mathbf{x}(t))\rangle = \hat{H}(\mathbf{x}(t)) |\psi(\mathbf{x}(t))\rangle, \quad (4.9)$$

and using the adiabatic approximation, we get [143]

$$\gamma_n(t) = i \int_0^t \left\langle n(\mathbf{x}(t)) \left| \frac{d}{dt} \right| n(\mathbf{x}(t)) \right\rangle dt. \quad (4.10)$$

However, since the eigenvectors are defined upto a phase factor, under the transformation

$$|n(\mathbf{x}(t))\rangle \rightarrow e^{i\gamma_n(t)} |n(\mathbf{x}(t))\rangle, \quad (4.11)$$

we have,

$$\langle n | n \rangle' = \langle n | n \rangle + i\dot{\gamma}_n(t) = 0. \quad (4.12)$$

Thus we can write

$$|\psi(\mathbf{x}(t))\rangle = e^{-i \int_0^t E(t') dt'} |n(\mathbf{x}(0))\rangle', \quad (4.13)$$

such that  $\dot{\gamma}_n(t) = 0$ . Thus we can always chose the phase of the eigenvector according to Eq. (4.12) at all the times such that the factor  $\dot{\gamma}_n = 0$ . However, Berry showed that this condition cannot be simultaneously realized over the whole parameter space. In particular if we consider cyclic evolution in the space of parameters then the phase factor  $\gamma_n$  becomes invariant under phase transformations. To see this we write

$$\begin{aligned} \gamma_n(t) &= i \int_0^t \left\langle n(\mathbf{x}(t)) \left| \frac{d}{dt} \right| n(\mathbf{x}(t)) \right\rangle = i \int_0^t \langle n(\mathbf{x}(t)) | \nabla_{\mathbf{x}} | n(\mathbf{x}(t)) \rangle \cdot \frac{d\mathbf{x}}{dt} dt \\ &= i \int_{\mathbf{x}_i(0)}^{\mathbf{x}_i(t)} \langle n(\mathbf{x}(t)) | \nabla_{\mathbf{x}} | n(\mathbf{x}(t)) \rangle \cdot d\mathbf{x}. \end{aligned} \quad (4.14)$$

Under a cyclic evolution in the parameter space  $C : [0, \tau] \rightarrow [x_i(0), x_i(\tau)]$  we get

$$\gamma_n[C] = \oint_C \mathbf{A}_n(\mathbf{x}) \cdot d\mathbf{x}, \quad (4.15)$$

where  $\mathbf{A}_n(\mathbf{x}) = i \langle n(\mathbf{x}(t)) | \nabla_{\mathbf{x}} | n(\mathbf{x}(t)) \rangle$ . Now if we choose to redefine the phase of the eigenstate

$$|n(\mathbf{x}(t))\rangle \rightarrow e^{i\zeta(\mathbf{x})} |\psi(\mathbf{x}(t))\rangle, \quad (4.16)$$

then

$$\mathbf{A}_n(\mathbf{x}) \rightarrow \mathbf{A}_n(\mathbf{x}) - i\nabla_{\mathbf{x}}\zeta(\mathbf{x}). \quad (4.17)$$

If the parameter space is three-dimensional then we can write

$$\gamma_n[C] = \int_S \nabla_{\mathbf{x}} \times \mathbf{A}_n(\mathbf{x}) \cdot d\mathbf{S}, \quad (4.18)$$

where  $S$  is the surface bounded by the closed curve  $C$ . Thus the transformation (4.17) leaves the geometric phase invariant. Thus the geometric phase is non-integrable and non-local.

If we define vector field  $\mathbf{V}_n(\mathbf{x}) = \nabla_{\mathbf{x}} \times \mathbf{A}_n(\mathbf{x})$ , then the geometric phase can be seen as flux of the field  $\mathbf{V}_n$  through the surface  $S$

$$\gamma_n[C] = \int_S \mathbf{V}_n(\mathbf{x}) \cdot d\mathbf{S}. \quad (4.19)$$

In higher-dimensional parameter space, the geometric phase  $\gamma[C]$  has an appropriate generalization in terms of integral of a curvature two-form over a surface bounded by  $C$  [144, 145].

### 4.1.2 Example- Spin precession in a magnetic field

A simple illustrative example where non-trivial Berry phase arises is that of spin precession in a magnetic field. For a spin  $1/2$  particle in a magnetic field, the Hamiltonian is given by

$$H = -\frac{\mu}{2}\boldsymbol{\sigma} \cdot \mathbf{B}. \quad (4.20)$$

Consider the magnetic field rotating in the x-y plane at an angle  $\theta_0$  from the z axis

$$B(t) = B(\sin \theta_0 \cos \phi(t), \sin \theta_0 \sin \phi(t), \cos \theta_0). \quad (4.21)$$

The energy eigenvalues are  $E_{\pm} = \pm\mu B/2$  and corresponding eigenvectors  $|\pm\rangle$  can be calculated. The geometric phase associated with  $|+\rangle$  is then given by [143]

$$\gamma_+[C] = -\pi(1 - \cos \theta_0) = -\frac{1}{2}\Omega[C], \quad (4.22)$$

where  $\Omega[C]$  is the solid angle subtended by the curve  $C$  at the center of the sphere. The point  $B = 0$  represents a point of degeneracy where the energy eigenvalues cross and the adiabatic condition breaks down. So the closed circuit must not include the point of degeneracy. To see the nature of degeneracy, consider the vector field

$$\mathbf{V}_n = -j\frac{\hat{B}}{B^2}, \quad (4.23)$$

which represents a magnetic monopole of strength  $j$  at the origin in the parameter space. According to Eq. (4.19) the geometric phase is given by

$$\gamma_n[C] = -j\Omega[C]. \quad (4.24)$$

The resemblance of Eqs. (4.22) and (4.24) shows that the point of degeneracy appears as a magnetic monopole. The vector field may be thought of as radiating from an effective

magnetic monopole of strength  $j$  at the origin of the parameter space. The effect of the degeneracy is felt by a closed loop at a distance from the degeneracy and the Berry phase is the flux associated with this monopole through the surface bounded by this closed loop.

### 4.1.3 Aharonov- Anandan phase

The notion of geometric phase was extended by Aharonov-Anandan [146] for any general cyclic motion without regard to adiabaticity. According to their prescription, one can split the total phase into dynamical and geometric parts by considering the evolution of eigenvectors in the state space, rather than the parameter space. The geometric phase can then be defined as the difference between the total and dynamical phase.

Let  $\mathcal{H}$  denote the Hilbert space consisting a set of possible states of a quantum system (assumed to be normalized). Since two vectors  $|\psi\rangle, e^{i\phi}|\psi\rangle \in \mathcal{H}$  differing only by the phase factor correspond to the same physical state, we define a projection map

$$\begin{aligned} \pi : \mathcal{H} &\rightarrow \mathcal{P}(\mathcal{H}), \\ \pi(e^{i\alpha}|\psi\rangle) &= \pi(|\psi\rangle) \in \mathcal{P}(\mathcal{H}) \quad \forall \alpha \in \mathbb{R} \text{ and } |\psi\rangle \in \mathcal{H}. \end{aligned} \quad (4.25)$$

$\mathcal{P}(\mathcal{H})$  is known as projective Hilbert space. If the evolution  $|\psi(t)\rangle$  traces out a curve  $\mathcal{C}$  in  $\mathcal{H}$  such that

$$|\psi(\tau)\rangle = e^{i\phi}|\psi(0)\rangle, \quad (4.26)$$

then the corresponding curve  $\mathcal{C} = \pi(\mathcal{C})$  in the projective Hilbert space  $\mathcal{P}(\mathcal{H})$  is closed (Fig. 4.2).

There can be infinitely many curves in  $\mathcal{H}$  which project to a given closed curve  $\mathcal{C}$  in  $\mathcal{P}(\mathcal{H})$ . So we ask a reverse question: given a closed curve  $\mathcal{C}$  in  $\mathcal{P}$ , can we select a curve in  $\mathcal{H}$  for

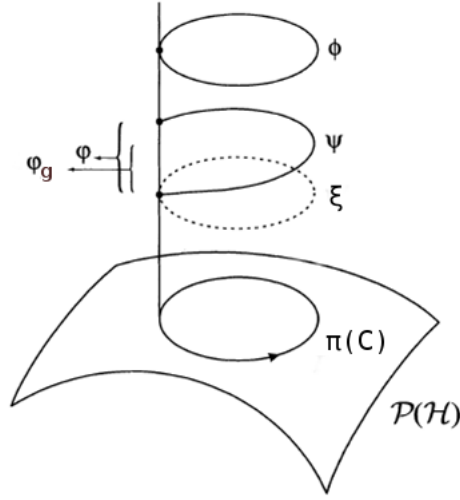


Figure 4.2: Cyclic evolution of vector in projective Hilbert state  $\mathcal{P}(\mathcal{H})$ . A closed curve  $\mathcal{C} = \pi(\mathcal{C})$  in  $\mathcal{P}(\mathcal{H})$  can have infinitely many lifts in  $\mathcal{H}$  which may or may not be closed. This is called principal fiber bundle picture of the state space. The bundle space  $\mathcal{H}$  consists of three parts: the base manifold  $\mathcal{P}(\mathcal{H})$ , the fiber which is the group  $U(1)$  attached to each point of base manifold and the map  $\pi : \mathcal{H} \rightarrow \mathcal{P}(\mathcal{H})$ . A closed curve in the bundle space begins and ends on the same fiber. (Figure taken from Ref. [147]).

which dynamical and geometric part can be separated. To achieve this, we define

$$|\psi(t)\rangle = e^{if(t)} |\xi(t)\rangle, \quad (4.27)$$

such that  $f(\tau) - f(0) = \phi$ . From Eq. (4.26) it follows that  $|\xi(t)\rangle$  is smooth single-valued function in  $\mathcal{H}$  with  $|\xi(\tau)\rangle = |\xi(0)\rangle$ . Under Schrödinger evolution we have

$$\begin{aligned} i \frac{d|\psi(t)\rangle}{dt} &= H |\psi(t)\rangle, \\ i \frac{d|\xi(t)\rangle}{dt} &= (H + \dot{f}) |\xi(t)\rangle, \\ \frac{df}{dt} &= i \left\langle \xi \left| \frac{d}{dt} \right| \xi \right\rangle - \langle \xi | H | \xi \rangle. \end{aligned} \quad (4.28)$$

Integrating, we get the total phase

$$\phi = \phi_d + \phi_g, \quad (4.29)$$

where

$$\phi_d = - \int_0^\tau \langle \xi | H | \xi \rangle dt = \int_0^\tau \langle \psi | H | \psi \rangle dt \quad (4.30)$$

is the dynamical phase and

$$\phi_g[\mathcal{C}] = i \int_0^\tau \left\langle \xi \left| \frac{d}{dt} \right| \xi \right\rangle dt = \oint_{\mathcal{C}} \langle \xi | d | \xi \rangle \quad (4.31)$$

is the geometric phase. Now, one can choose the same  $|\xi(t)\rangle$  for infinitely many curves  $\mathcal{C} \in \mathcal{H}$ , which project to the given curve  $\mathcal{C} = \pi(\mathcal{C}) \in \mathcal{P}(\mathcal{H})$ , by an appropriate choice of  $f(t)$ . Thus this definition of  $\phi_g$  depends only on the curve in the projective Hilbert space  $\mathcal{P}(\mathcal{H})$  and is independent of the total phase  $\phi$  and the Hamiltonian producing the motion. Also, since the state  $|\psi\rangle$  need not be an eigenstate of  $H$ , hence adiabaticity and cyclic evolution of  $H(t)$  are not required. Further,  $\phi_g$  is independent of parameter  $t$  of  $\mathcal{C}$  (reparametrization invariant) and is gauge invariant. To prove the gauge invariance of  $\phi_g$ , we transform  $|\xi(t)\rangle \rightarrow e^{i\alpha(t)} |\xi(t)\rangle$ , then the geometric phase transforms as

$$\phi_g[\mathcal{C}] = i \oint_{\mathcal{C}} \left\langle \xi \left| \frac{d}{dt} \right| \xi \right\rangle dt - [\alpha(\tau) - \alpha(0)]. \quad (4.32)$$

Since  $|\xi(t)\rangle$  is single-valued, therefore  $\alpha(\tau) = \alpha(0)$ . Thus geometric phase is invariant under gauge transformation.

#### 4.1.4 Noncyclic Geometric Phase

The definition of non-adiabatic geometric phase (Eq. 4.31) requires cyclicity in the state space  $\mathcal{P}(\mathcal{H})$ . However, in a general evolution the state vector may not return to the same fiber in the bundle space giving rise to an open curve in  $\mathcal{P}(\mathcal{H})$ . Samuel and Bhandari [148] considered such a case of noncyclic evolution and used Panchratanam's idea to compare the phase on two different fibers of the principal fiber bundle. They showed that in this case the geometric phase is proportional to the surface area enclosed by the curve in  $\mathcal{P}(\mathcal{H})$

which is composed of two parts: the open curve  $\mathcal{C} = \{\pi(|\xi(s)\rangle) \in \mathcal{P}(\mathcal{H}) | s \in [s_1, s_2] \subset \mathbb{R}\}$  describing the evolution from the initial point  $|\xi(s_1)\rangle$  to the final point  $|\xi(s_2)\rangle$ , and a geodesic curve in  $\mathcal{P}(\mathcal{H})$  joining  $\pi(|\xi(s_2)\rangle)$  to  $\pi(|\xi(s_1)\rangle)$ .

Even though the geodesic closure approach gives an elegant and robust definition of geometric phase, the calculations of geodesic can be tedious and in some cases may lead to inconsistent results [149]. An equivalent approach to calculate the geometric phase for any general nonadiabatic, noncyclic evolution has been developed by Mukunda and Simon [150]. Their treatment is based entirely on kinematics, and the geometric phase is defined as a property of curves in the Hilbert space. If  $\mathcal{C}$  is any one-parameter smooth curve of unit vectors  $|\psi(s)\rangle \in \mathcal{H}$ , where  $s \in [s_1, s_2] \subset \mathbb{R}$ , then the geometric phase associated with the corresponding curve  $\mathcal{C} \in \mathcal{P}(\mathcal{H})$  is defined by the functional

$$\phi_g[\mathcal{C}] = \arg \langle \psi(s_1) | \psi(s_2) \rangle - \Im \int_{s_1}^{s_2} ds \langle \psi(s) | \dot{\psi}(s) \rangle, \quad (4.33)$$

where  $|\dot{\psi}(s)\rangle$  denotes the derivative with respect to  $s$ . The two terms on the right-hand side of Eq. (4.33) are, respectively the total and dynamical phase associated with the curve  $\mathcal{C}$ , and the difference between the two gives the geometric phase along  $\mathcal{C}$ . The geometric phase defined this way is both gauge and reparametrization invariant. To check the gauge invariance of  $\phi_g$ , consider a local gauge transformation  $|\psi(s)\rangle \rightarrow e^{i\alpha(s)} |\psi(s)\rangle$ , then

$$\begin{aligned} \phi_g[\mathcal{C}] &\rightarrow (\alpha(s_2) - \alpha(s_1)) + \arg \langle \psi(s_1) | \psi(s_2) \rangle - \Im \int_{s_1}^{s_2} ds \left( \langle \psi(s) | \dot{\psi}(s) \rangle + i\dot{\alpha}(s) \right) \\ &= \arg \langle \psi(s_1) | \psi(s_2) \rangle - \Im \int_{s_1}^{s_2} ds \langle \psi(s) | \dot{\psi}(s) \rangle. \end{aligned} \quad (4.34)$$

The geometric phase in  $\phi_g[\mathcal{C}]$  is only defined modulo  $2\pi$ , because of the form of total phase in Eq. (4.33). Also, in case the vectors  $|\psi(s_1)\rangle$  and  $|\psi(s_2)\rangle$  are orthogonal both the total phase and hence  $\phi_g[\mathcal{C}]$  are undefined.

## 4.2 Neutrino propagation in magnetic fields

The emergence of geometric phase in the context of neutrino oscillations has been explored by many authors in various settings [151–165]. In the present work we analyze the noncyclic geometric phases that arise due to neutrino oscillations in magnetic fields and matter. In particular, we first perform explicit calculations for the geometric phases that arise due to spin and spin-flavor precession of neutrinos propagating in a medium with constant density and uniformly twisting magnetic fields. We then study the case of geometric phase acquired by neutrinos produced inside and emanating out of a neutron star, with realistic density and magnetic field profiles. We also study the condition of adiabaticity, the effects of magnetic field rotation and cross boundary effects on geometric phases and neutrino helicity transitions.

In the quasiclassical approach, neutrino spin evolution in an electromagnetic field is described by the generalized Bargmann-Michel-Telegdi equation [166]. For the system  $|\nu\rangle = (\nu_R, \nu_L)^T$  with two helicity components of neutrinos propagating in the presence of magnetic field  $\vec{B}$  in matter, the effective Hamiltonian is given by [75] (see also Eq. (2.74))

$$H = (\vec{\sigma} \cdot \vec{n}) \left( \frac{\Delta m^2 A}{4E} - \frac{\Delta V}{2} \right) - \mu \vec{\sigma} \cdot \left[ \vec{B} - \left( 1 + \frac{1}{\gamma} \right) (\vec{B} \cdot \vec{n}) \vec{n} \right], \quad (4.35)$$

where  $\vec{n}$  is the direction of propagation of the neutrino,  $\vec{\sigma}$  are Pauli spin matrices,  $\Delta V = V_L - V_R$  ( $V_L, V_R$  being potentials due to coherent forward scattering of the neutrinos off matter particles [21] for left- and right-handed neutrinos respectively),  $\Delta m^2 = m_R^2 - m_L^2$ ,  $A$  is a function of neutrino mixing angle  $\theta$ , and  $E$  is the neutrino energy. In Eq. (4.35) the terms proportional to identity matrix are omitted.

Assuming the neutrinos to be propagating along the z-direction, the evolution of the state  $|\nu\rangle$  can be described by the Schrödinger-like equation [74]

$$i\frac{\partial |\nu(t)\rangle}{\partial t} = H(t) |\nu(t)\rangle. \quad (4.36)$$

Since the longitudinal component of the magnetic field in Eq. (4.36) is suppressed by a factor of  $1/\gamma$ , for relativistic neutrinos this term can be neglected. Also, we consider the magnetic field rotating clockwise about the neutrino direction in the transverse plane  $B_{\perp} = Be^{i\phi}$ . The evolution equation (4.36) can now be rewritten as

$$i\frac{\partial}{\partial z} \begin{pmatrix} \nu_R \\ \nu_L \end{pmatrix} = - \begin{pmatrix} V(z)/2 & \mu B(z)e^{-i\phi(z)} \\ \mu B(z)e^{i\phi(z)} & -V(z)/2 \end{pmatrix} \begin{pmatrix} \nu_R \\ \nu_L \end{pmatrix}, \quad (4.37)$$

where

$$V = \Delta V - \frac{\Delta m^2 A}{2E}, \quad (4.38)$$

and the distance  $z$  along the neutrino trajectory is approximated with time  $t$ .

Transforming to the rotating frame of the field, and using

$$|\nu\rangle = U |\psi\rangle = \exp(-i\sigma_3\phi/2) |\psi\rangle, \quad (4.39)$$

we get an evolution equation in the rotating frame,

$$\begin{aligned} i\frac{\partial |\psi\rangle}{\partial z} &= (U^{-1}HU - iU^{-1}\frac{dU}{dz}) |\psi\rangle \\ &= -\frac{1}{2} [(V + \dot{\phi})\sigma_3 + (2\mu B)\sigma_1] |\psi\rangle, \end{aligned} \quad (4.40)$$

where  $\dot{\phi} = d\phi/dz$ . For the case of neutrino propagation in matter with constant density and in a magnetic field of constant strength and uniform twist, i.e., constant  $V$ ,  $B$ , and  $\dot{\phi}$ ,

Eq. (4.40) can be integrated analytically and we obtain

$$\begin{pmatrix} \psi_R(z) \\ \psi_L(z) \end{pmatrix} = \exp \left[ \frac{i}{2} \left( (V + \dot{\phi})\sigma_3 + 2\mu B\sigma_1 \right) z \right] \begin{pmatrix} \psi_R(0) \\ \psi_L(0) \end{pmatrix}. \quad (4.41)$$

Using properties of Pauli matrices this can be written as

$$\begin{pmatrix} \psi_R(z) \\ \psi_L(z) \end{pmatrix} = \left[ \cos \left( \frac{\delta E_m z}{2} \right) + \frac{i}{\delta E_m} \left( (V + \dot{\phi})\sigma_3 + 2\mu B\sigma_1 \right) \sin \left( \frac{\delta E_m z}{2} \right) \right] \begin{pmatrix} \psi_R(0) \\ \psi_L(0) \end{pmatrix}, \quad (4.42)$$

where

$$\delta E_m = \sqrt{(V + \dot{\phi})^2 + (2\mu B)^2} \quad (4.43)$$

gives the energy splitting of the eigenstates. If a neutrino is initially created in the left-helicity state, i.e.,  $|\nu(0)\rangle = (0 \ 1)^T$ , then after traveling a distance  $z$  in the magnetic field, the neutrino eigenstate will be an admixture of left- and right-handed components:

$$|\nu(z)\rangle = \begin{pmatrix} ie^{-i\phi(z)/2} \sin 2\theta_m \sin \left( \frac{\delta E_m z}{2} \right) \\ e^{i\phi(z)/2} \left( \cos \left( \frac{\delta E_m z}{2} \right) - i \cos 2\theta_m \sin \left( \frac{\delta E_m z}{2} \right) \right) \end{pmatrix}. \quad (4.44)$$

Here, we have taken the reference direction as  $\phi(0) = 0$  and  $\theta_m$  denotes the mixing angle between  $\psi_R$  and  $\psi_L$ ,

$$\tan 2\theta_m = \frac{2\mu B}{V + \dot{\phi}}. \quad (4.45)$$

If a beam of left-handed neutrinos starts at  $z = 0$ , the transition probability at a distance  $z$  is given by

$$P(\nu_L \rightarrow \nu_R; z) = |\nu_R(z)|^2 = \sin^2 2\theta_m \sin^2 \left( \frac{\delta E_m z}{2} \right). \quad (4.46)$$

Thus neutrino propagation in magnetic fields results in an oscillation in the  $\nu_L - \nu_R$  basis with a length scale of  $2\pi/\delta E_m$ . For  $\theta_m = \pi/4$  the mixing is maximal and the amplitude of the transition probability becomes unity. Eq. (4.45) gives the condition for resonant

$\nu_R \leftrightarrow \nu_L$  conversion

$$\begin{aligned}
 & V + \dot{\phi} = 0, \\
 \text{or} \quad & \Delta V - \frac{\Delta m^2}{2E} A + \dot{\phi} = 0.
 \end{aligned} \tag{4.47}$$

The effects of the variation of the twisting field on the transition probability has been explored in detail in [167].

### 4.3 Bloch sphere representation of neutrino spin rotation and noncyclic geometric phases

The dynamics of the neutrino spin rotation in a magnetic field can be described by spin-polarization vector  $\mathbf{n} = \langle \nu | \boldsymbol{\sigma} | \nu \rangle$ . In the two component formalism the equation describing the dynamics of  $\mathbf{n}$  is equivalent to a Schrödinger-like equation (4.37), and is given by [168]

$$\frac{d\mathbf{n}}{dz} = \mathbf{n} \times \mathbf{B}_{\text{eff}}, \tag{4.48}$$

where  $\mathbf{B}_{\text{eff}} = \sqrt{V^2 + (2\mu B)^2}(\sin \chi \cos \phi, \sin \chi \sin \phi, \cos \chi)$ ;  $\chi = \tan^{-1}(2\mu B/V)$ . The path of the effective magnetic field  $\mathbf{B}_{\text{eff}}$  describes a circle around the z axis in the parameter space, which is the unit two-sphere  $S^2$ . For the case of a medium with a uniformly twisting magnetic field and constant density as discussed in the previous section, Eq. (4.48) can be solved analytically, and the resulting solution  $\mathbf{n}(z)$  can be plotted in the Bloch sphere representation. In this representation, a given neutrino state  $|\nu\rangle$  corresponds to a point on  $S^2$  and is determined by the unit vector  $\mathbf{n}$ . The orthogonal states  $|\nu_L\rangle$  and  $|\nu_R\rangle$  correspond to two antipodal points on  $S^2$ .

To solve Eq. (4.48), we define a vector  $\mathbf{n}_R = \mathbf{n} \cdot \mathbf{R}$ , where  $\mathbf{R}$  is the rotation matrix

$$\mathbf{R} = \begin{pmatrix} \cos \phi & \sin \phi & 0 \\ -\sin \phi & \cos \phi & 0 \\ 0 & 0 & 1 \end{pmatrix}. \quad (4.49)$$

Substituting this in Eq. (4.48) we obtain a time-independent differential equation for  $\mathbf{n}_R$ , which can be integrated to give the solution for Eq. (4.48) as the superposition of two rotations,

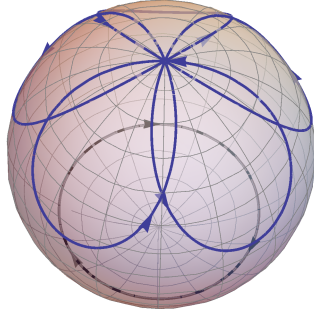
$$\mathbf{n}(z) = \mathbf{R}^T \cdot \mathbf{R}_1 \cdot \mathbf{n}(0), \quad (4.50)$$

where  $\mathbf{R}_1$  is given by

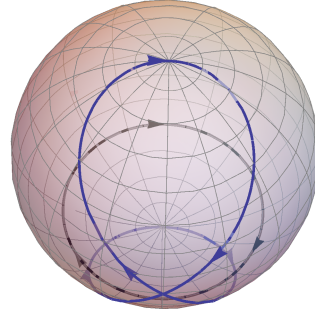
$$\mathbf{R}_1 = \begin{pmatrix} \sin^2 2\theta_m + \cos^2 2\theta_m \cos \phi_p & \cos 2\theta_m \sin \phi_p & \frac{1}{2} \sin 2\theta_m (1 - \cos \phi_p) \\ -\cos 2\theta_m \sin \phi_p & \cos \phi_p & \sin 2\theta_m \sin \phi_p \\ \frac{1}{2} \sin 2\theta_m (1 - \cos \phi_p) & -\sin 2\theta_m \sin \phi_p & \cos^2 2\theta_m + \sin^2 2\theta_m \cos \phi_p \end{pmatrix}, \quad (4.51)$$

where we have defined the precession phase as  $\phi_p = \delta E_m z$ , such that  $\phi_p$  varies from 0 to  $2\pi$  during one oscillation length.

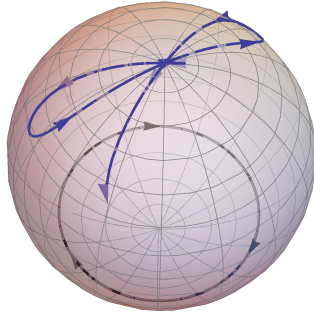
The matrix  $\mathbf{R}_1$  represents a precession about the direction of  $\mathbf{B}_{\text{eff}}$  at an angle  $2\theta_m$  and at a rate  $\dot{\phi}_p$  while  $\mathbf{R}$  represents a precession about the direction of propagation of the neutrino at a rate,  $\dot{\phi}$ . These two precessions combine to give the evolution of the spin-polarization vector  $\mathbf{n}$ , which may be plotted on the Bloch sphere. The curve traced by the vector  $\mathbf{n}$  on the Bloch sphere, as the magnetic field rotates by  $2\pi$ , is noncyclic in general. However, for the special case when the two precession rates  $\dot{\phi}_p$  and  $\dot{\phi}$  are commensurable i.e.  $\dot{\phi}_p = k\dot{\phi}$  for some  $k \in \mathbb{Q}$ , the evolution becomes cyclic. Different cases for cyclic and noncyclic evolution are shown in Fig. 4.3 for the case of spin precession  $\nu_{eL} \rightarrow \nu_{eR}$  of left-handed electron neutrinos produced in the Sun and propagating outwards under the influence of matter and magnetic fields. As a first order calculation we assume a constant density and magnetic field profile for the Sun and parametrize the rotation frequency of the magnetic



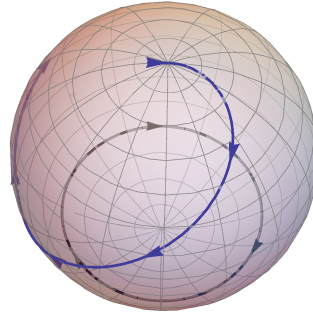
(a)  $\dot{\phi}_p = 5\dot{\phi}$



(b)  $V = -\dot{\phi}$



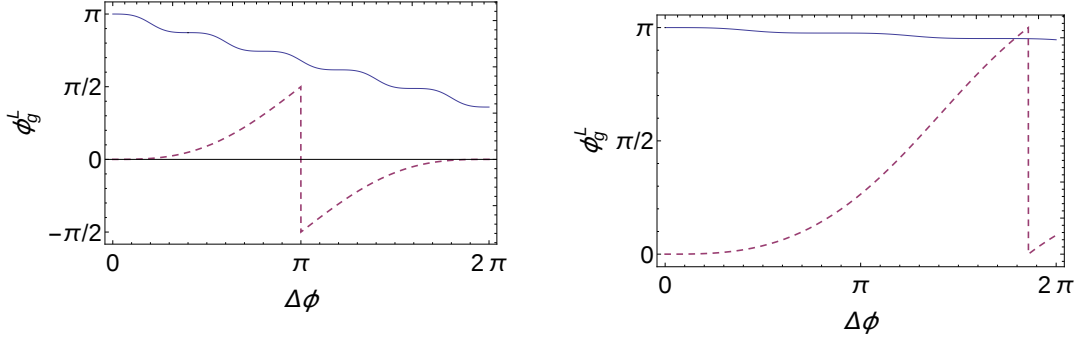
(c)  $\dot{\phi} = 100$



(d)  $\dot{\phi} = -200$

Figure 4.3: Bloch sphere representation of neutrino spin rotation. Initially the neutrinos are produced in the left helicity state which corresponds to a point on the pole of the sphere. Under the effect of matter and magnetic field, neutrinos undergo spin-precession  $\nu_{eL} \rightarrow \nu_{eR}$  and neutrino spin-vector  $\mathbf{n}$  traces out cyclic [(a) and (b)] and noncyclic curves [(c) and (d)] on the Bloch sphere depending on the relative values of  $\dot{\phi}_p$  and the parameters of  $\mathbf{B}_{\text{eff}}$ . The circular curve describes the path of  $\mathbf{B}_{\text{eff}}$ . The rotation frequency is in units of  $\pi/R$ , and the positive and negative signs of  $\dot{\phi}$  correspond to clockwise and anticlockwise rotation of the magnetic field about the neutrino direction respectively. We used the following parameters: electron number density  $n_e = 10^{24} \text{g/cm}^3$ , neutron number density  $n_n = n_e/6$ , matter potential  $V = \sqrt{2}G_F(n_e - n_n/2)$ , and magnetic field strength  $B = 10^6 \text{ G}$ .

field as  $\dot{\phi} = \pi/fR$ , where  $R$  is the radius of the Sun.



(a) Cyclic geometric phase: Solid curve corresponds to the cyclic case  $\dot{\phi}_p = 5\dot{\phi}$  and the dotted curve corresponds to the resonant condition  $V = -\dot{\phi}$  (b) Noncyclic geometric phase for the cases  $\dot{\phi} = 100$  (solid curve) and  $\dot{\phi} = -200$  (dotted curve)

Figure 4.4: Geometric phases associated with the curves in the Bloch sphere for neutrino spin-precession  $\nu_{eL} \rightarrow \nu_{eR}$ .

The area enclosed by the trajectory traced out by neutrino spin rotation in projective Hilbert space, which in this case is Bloch sphere  $S^2$ , is related to the geometric phases acquired by the neutrino state during the evolution. If a neutrino is initially created in the left-helicity state, i.e.,  $|\nu(0)\rangle = (0 \ 1)^T$ , then after traveling a distance  $z$  in the magnetic field the neutrino eigenstate will be a mixture of left- and right-handed components  $|\nu(z)\rangle = (\nu_R(z) \ \nu_L(z))^T$ . The geometric phase associated with the curve  $\mathcal{C}$  traced by the state  $|\nu(z)\rangle$  on the Bloch sphere is then given by

$$\phi_g^L[\mathcal{C}] = \arg \langle \nu(0) | \nu(z) \rangle - \Im \int_0^z \langle \nu(z') | \frac{d}{dz'} | \nu(z') \rangle dz'. \quad (4.52)$$

Using Eq. (4.44), we get the following expressions for the geometric phase:

$$\phi_g^L[\mathcal{C}] = -\arctan \left( \cos 2\theta_m \tan \frac{\phi_p}{2} \right) + \frac{\phi_p}{2} \cos 2\theta_m + \frac{\Delta\phi}{2} \sin^2 2\theta_m \left( 1 - \frac{\sin \phi_p}{\phi_p} \right), \quad (4.53)$$

where  $\Delta\phi = \phi(z) - \phi(0)$ . Similarly if a neutrino is produced initially in the right-helicity state, the geometric phase acquired is

$$\phi_g^R = -\phi_g^L. \quad (4.54)$$

Hence the spin and spin-flavor evolution of neutrino helicity states involve nonzero geometric phases. These expressions for geometric phases are valid regardless of whether the neutrino propagation is adiabatic or not, unlike the case of the Berry phase which requires the propagation to be adiabatic.

Two particular cases clearly bring out the relation between the geometric phase and area enclosed by neutrino spin trajectory on the Bloch sphere. In the cyclic limit, as the neutrino spin-vector  $\mathbf{n}$  returns to its initial position i.e.  $\phi_p = 2\pi$ , the geometric phase for each cycle is given by Eq. (4.53) as

$$\phi_g^L[\mathcal{C}]|_{cyc} = -\pi(1 - \cos 2\theta_m) + \frac{\Delta\phi}{2} \sin^2 2\theta_m. \quad (4.55)$$

This result is particularly easy to visualize in the rotating frame of the magnetic field where  $\Delta\phi = 0$ . In this frame the geometric phase reduces to the famous value  $-\pi(1 - \cos 2\theta_m)$ , which is equal to  $-\frac{1}{2}$  of the solid angle subtended, by the neutrino spin rotation trajectory on the Bloch sphere, at the center of the sphere. Another interesting case is that of resonance condition (4.47), for which Eq. (4.55) gives the geometric phase:

$$\phi_g^L[\mathcal{C}]|_{res} = 0. \quad (4.56)$$

This is expected since the resonance condition corresponds to the case when the neutrino trajectory traces out a great circle in the  $x - z$  plane in the rotating frame. This is akin to parallel transport of a vector along a geodesic, which does not give rise to holonomy. The corresponding curve in Fig. 4.3b encloses no net oriented area, and thus has zero geometric phase.

For the case of noncyclic evolutions the geometric phase can be interpreted in terms of a solid angle subtended by the neutrino spin rotation curve obtained by geodesic closure on the Bloch sphere. In Fig. 4.4, we plot the variation of the geometric phase with the relative phase shift of the magnetic field for the case of neutrino spin precession  $\nu_{eL} \rightarrow \nu_{eR}$ .

Next we will study the neutrino spin and spin-flavor evolution in the case of a neutron star with realistic density and magnetic field profiles. We will examine various cases both inside and outside the neutron star and analyze the quantitative difference in geometric phases in different scenarios.

## 4.4 Neutrino Propagation in Neutron Stars

When stars run out of nuclear fuel at the end of their lives, the core of the star collapses under its own gravity resulting in a supernova explosion. Neutron stars (NSs) are the compact objects that are formed as final remnants of the core collapse supernova of stars with a mass of about 8 – 20 times the mass of the Sun. NSs contain some of the most extreme astrophysical environments where the interior densities can be  $\sim 5 - 10$  times the nuclear saturation density ( $\approx 2.8 \times 10^{14} \text{ g/cm}^3$ ) and where magnetic fields from the surface to the interiors can vary from  $10^{15}$  to  $10^{18}$  G [169, 170]. Although NSs are primarily composed of neutrons, there is also a small fraction of protons, electrons, and other nuclei. In the interior where density exceeds nuclear saturation density, exotic particles such as deconfined quarks, stable hyperon matter, and superfluid pion condensate may appear [171, 172].

Neutrinos play an important role in the formation and subsequent cooling of NSs. During the first few seconds of the supernova collapse a large number of neutrinos diffuse through the resulting proto-NS, which leads to a rapid drop in temperature by a factor of  $\sim 100$ . After about a minute, the NS becomes transparent to neutrinos resulting in a further drop in temperatures. The main process by which the neutrinos are produced in the NS cores is so-called direct Urca process  $n \rightarrow p + e^- + \bar{\nu}_e, p + e^- \rightarrow n + \nu_e$  [172, 173]. However, the direct Urca process requires a certain energy threshold below which the neutrino emission occurs via modified Urca process  $n + (n, p) \rightarrow p + (n, p) + e^- + \bar{\nu}_e, p + (n, p) \rightarrow n + (n, p) + e^+ + \nu_e$  [174]. There are several other mechanisms by which neutrinos are produced in the NSs and help in the NS cooling (see [175] for a detailed review).

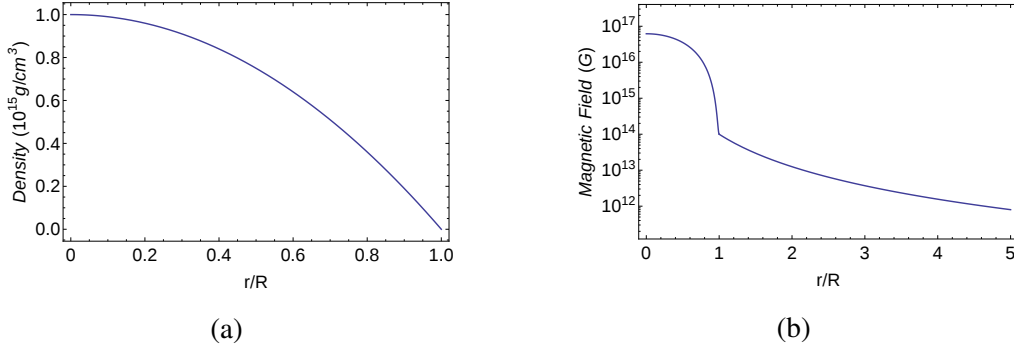


Figure 4.5: (a) Density and (b) magnetic field profiles of the neutron star. Magnetic field is plotted in log scale.

In the following we study the spin-flavor evolution of the neutrinos produced in the core region of the NS. For definiteness we consider only the left-handed electron neutrinos produced below the resonance region and calculate the acquired geometric phase as they propagate in the interior regions of the NS and finally come out of it. We also study the effect of magnetic field rotation on the geometric phases and the probabilities of the spin and spin-flavor conversion. These calculations require the knowledge of the density and magnetic field profiles in the interior and outer regions of the NS. The knowledge of the exact density profile of NS depends strongly on the equation of state for which many models have been proposed (see [176] for a recent review). However, without going into details of the models, we assume a simplistic density profile where the density decreases quadratically from the center

$$\rho Y_e^{\text{eff}} = \begin{cases} \rho_0 + \rho_1 r^2, & \text{for } r \leq R \\ 0 & \text{for } r > R \end{cases}, \quad (4.57)$$

where  $R$  is the radius and  $\rho_0$  is the central density of the NS. The values of radius and central density are taken as  $R = 10$  km and  $\rho_0 = 10^{15}$  g/cm<sup>3</sup>. The typical surface density of the NS is  $\sim 10^9$  g/cm<sup>3</sup> which determines the value of  $\rho_1$ . The magnetic field profile in

the interior [177] and outer [178] regions of the NS are taken as

$$B(r) = \begin{cases} B_s + B_c \left( 1 - \exp \left( -\beta (\rho/\rho_s)^\gamma \right) \right) & \text{for } r \leq R \\ B_s (R/r)^3 & \text{for } r > R \end{cases}, \quad (4.58)$$

where  $\beta = 0.005$ ,  $\gamma = 2$ ,  $B_c = 10^{18}$  G,  $B_s = 10^{14}$  G, and  $\rho_s$  is the nuclear saturation density. The density and magnetic field profiles for the NS are plotted in Fig. 4.5.

#### 4.4.1 Adiabaticity and Geometric phases

The Hamiltonian for the neutrino spin-flavor evolution equation (4.37) can be written as

$$H = -\frac{1}{2} \boldsymbol{\sigma} \cdot \mathbf{B}_{\text{eff}}(z), \quad (4.59)$$

where

$$\mathbf{B}_{\text{eff}} = |B_{\text{eff}}| (\sin \chi(z) \cos \phi(z), \sin \chi(z) \sin \phi(z), \cos \chi(z)), \quad (4.60)$$

$$|B_{\text{eff}}| = \sqrt{V(z)^2 + (2\mu B(z))^2}, \quad (4.61)$$

$$\chi(z) = \tan^{-1} \left( \frac{2\mu B(z)}{V(z)} \right), \quad (4.62)$$

$$V = \frac{\sqrt{2} G_F \rho Y_e^{\text{eff}}}{m_N} - \frac{\Delta m^2}{2E} \cos 2\theta. \quad (4.63)$$

Formally, the solution of Eq. (4.36) with Hamiltonian (4.59) is given by the evolution matrix

$$S(z, z_0) = \mathcal{P} \exp \left( -\frac{i}{2} \int_{z_0}^z (V(z') \sigma_3 + 2\mu B(z') \sigma_1) dz' \right), \quad (4.64)$$

where  $\mathcal{P}$  is the path ordering operator. However, in the limit of adiabatic approximation the state of the system is given by one of the instantaneous eigenstates of the Hamiltonian (4.59). The eigenstates, representing the spin polarization along and opposite to the

direction of  $\mathbf{B}_{\text{eff}}$  are given by

$$|\psi_+\rangle = \begin{pmatrix} \cos \chi(z)/2 \\ e^{i\phi(z)} \sin \chi(z)/2 \end{pmatrix}, \quad (4.65)$$

$$|\psi_-\rangle = \begin{pmatrix} e^{-i\phi(z)} \sin \chi(z)/2 \\ -\cos \chi(z)/2 \end{pmatrix}, \quad (4.66)$$

corresponding to the eigenvalues  $\mp |B_{\text{eff}}|/2$ . If the initial spin polarization of the neutrino is along the direction of magnetic field then the state of the system is represented by  $|\psi_+\rangle$ , and the adiabatic condition is given by

$$\left| \frac{\langle \psi_+ | \dot{\psi}_- \rangle}{E_+ - E_-} \right| \ll 1, \quad (4.67)$$

which is equivalent to  $\sqrt{\dot{\chi}^2 + (\dot{\phi} \sin \chi)^2}/2 \ll |B_{\text{eff}}|$ . We define the adiabaticity parameter

$$\gamma = \frac{|B_{\text{eff}}|}{\sqrt{\dot{\chi}^2 + (\dot{\phi} \sin \chi)^2}}, \quad (4.68)$$

so the adiabaticity condition (4.67) is equivalent to  $\gamma \gg 1$ . We now calculate  $\gamma$  for regions both inside and outside the NS. We find that, while in the inside region the adiabaticity holds for practically all values of  $\dot{\phi}$ , in the outside region of NS the range over which the adiabatic solution is valid is restricted and depends on the values of  $\dot{\phi}$ . The larger the value of  $\dot{\phi}$ , the smaller is the region over which the adiabatic approximation is valid. For typical values of  $\dot{\phi}$ , the range over which adiabaticity holds is roughly 20 – 30 times the radius of the NS as shown in Fig. 4.6.

In this case the magnetic field (4.60) traces out an open curve  $C_R$  in the parameter space  $R^3$ . Under adiabatic evolution the noncyclic geometric phase associated with the curve  $C_R$ , for the case of neutrino with initial spin polarization along the direction of magnetic

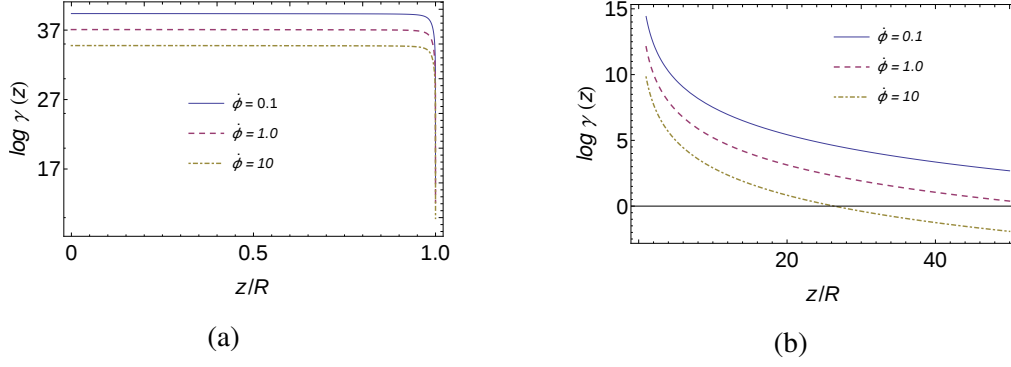


Figure 4.6:  $\log \gamma(z)$  as a function of distance (a) inside and (b) outside the NS. The adiabaticity condition  $\gamma \gg 1$  is satisfied for all values of  $\dot{\phi}$  while for the outside regions adiabaticity holds only in a limited region.

field, is given by the generalization of Berry's phase [149]

$$\phi_g[C_R] = \arg \langle \psi_+(0) | \psi_+(z) \rangle - \Im \int_0^z d\mathbf{R} \cdot \langle \psi_+(\mathbf{R}) | \nabla_{\mathbf{R}} | \psi_+(\mathbf{R}) \rangle, \quad (4.69)$$

where  $\mathbf{R}$  represents the magnetic field (4.60). Using Eq. (4.65) we calculate the geometric phase as

$$\phi_g^+[C_R] = \tan^{-1} \left( \frac{\sin \Delta\phi(z) \tan(\chi(z)/2) \tan(\chi(0)/2)}{1 + \cos \Delta\phi(z) \tan(\chi(z)/2) \tan(\chi(0)/2)} \right) - \frac{\Delta\phi(z)}{2} (1 - \cos \chi(z)). \quad (4.70)$$

While for the other eigenstate the geometric phase is  $\phi_g^-[C_R] = -\phi_g^+[C_R]$ .

Since the definition (4.69) assumes adiabaticity, the expression (4.70) is valid only when the adiabatic condition (4.67) is satisfied. When the nonadiabatic effects arise, one has to resort to more general methods such as that of geodesic closure to calculate geometric phases. However, we are only interested in the qualitative features of the geometric phases that arise due to neutrino spin and spin-flavor oscillations in the NS environment. Since in the inside region of the NS, the matter effects strongly dominate over the magnetic field, the area of the curve traced by  $\mathbf{B}_{\text{eff}}$  is negligible, and hence the associated geometric phase is vanishingly small. As the neutrinos come out of the NS, matter effects vanish and now neutrino eigenstates develop a significant geometric phase as shown in Fig. 4.7.

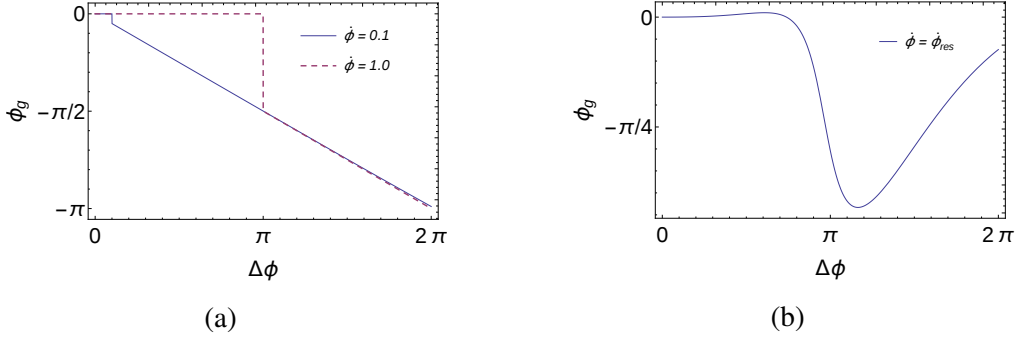


Figure 4.7: Geometric phases neutrino propagation in NS. In (a) the flat portion of the curve corresponds to neutrino propagation inside the NS, where the geometric phase is almost zero. In (b)  $\dot{\phi}_{\text{res}}$  corresponds to the resonant condition  $V = -\dot{\phi}$ .

#### 4.4.2 Transition probabilities and cross boundary effect

In this section we calculate the spin and spin-flavor transition probabilities as the neutrinos propagate in NS's under adiabatic conditions. Considering the case of left-handed electron neutrinos produced near the center of the NS, the adiabatic survival probability is given by [4, 178]

$$P(\nu_L \rightarrow \nu_L)(z) = \frac{1}{2} \left( 1 + \cos \theta_{\text{eff}}(z_0) \cos \theta_{\text{eff}}(z) + \sin \theta_{\text{eff}}(z_0) \sin \theta_{\text{eff}}(z) \cos \zeta(z) \right), \quad (4.71)$$

where

$$\theta_{\text{eff}}(z) = \tan^{-1} \left( \frac{2\mu B}{V + \dot{\phi}} \right), \quad (4.72)$$

$$\zeta(z) = \int_{z_0}^z dz' \sqrt{(V + \dot{\phi})^2 + (2\mu B)^2}. \quad (4.73)$$

For the neutrino propagation inside the NS, for the given density and magnetic field profile  $V \gg 2\mu B$ , and hence  $\theta_{\text{eff}} \approx 0$ , so according to Eq. (4.71):  $P(\nu_L \rightarrow \nu_L) \approx 1$ . Thus there are almost no spin or spin-flavor transitions inside the NS. However, for the outside case the situation is more interesting and there are appreciable transitions as shown in Fig. 4.8. After about  $200R$  half of the left-handed neutrinos produced inside the NS are converted into the right-handed neutrinos.

For the case of neutrino propagation in a medium of constant density and uniformly twisting magnetic fields, one can define a critical magnetic field, which is the magnetic field required for the oscillation amplitudes  $\nu_L \rightarrow \nu_R$  to be close to unity and is given by [178]

$$B_{\text{cr}}[G] = 43 \left( \frac{\mu_B}{\mu} \right) \left| \left( \frac{\Delta m^2}{1eV^2} \right) \left( \frac{MeV}{E} \right) \cos 2\theta - 2.5 \times 10^{-31} \left( \frac{n_{\text{eff}}}{\text{cm}^{-3}} \right) + 0.4 \left( \frac{\dot{\phi}}{m} \right) \right|. \quad (4.74)$$

By calculating  $B_{\text{cr}}$  for different situations, we can get rough estimates of the magnetic field required for appreciable neutrino transitions. In the interior regions of the neutron star,  $\rho \approx 10^{15} \text{ g/cm}^3$  gives  $n_{\text{eff}} \approx 6 \times 10^{38} \text{ cm}^{-3}$ , hence for neutrinos with energy  $E = 1 \text{ MeV}$ , Eq. (4.74) gives  $B_{\text{cr}} \approx 6 \times 10^{20} \text{ G}$ . Since  $B_{\text{cr}} \gg B$  in the interior of the neutron star, the transitions are negligible, as also shown by the probability argument above. Even in the outermost crust of the star,  $n_{\text{eff}} \approx 10^{33} \text{ cm}^{-3}$ , and  $B_{\text{cr}} \approx 10^{15} \text{ G}$ , which is greater than the magnetic fields prevailing in those regions. So we expect very weak neutrino transitions inside the neutron stars in the case of neutrinos produced below the resonance regions. For the regions just outside the neutron star density suddenly drops to zero, so there is a sharp decrease in the critical magnetic field required for the helicity transitions. For 1 MeV neutrinos, Eq. (4.74) gives  $B_{\text{cr}} = 10^8 \text{ G}$ . Since the magnetic field just outside the neutron star is  $\sim 10^{14} \text{ G} (\gg B_{\text{cr}})$ , as the neutrinos cross the surface of the NS, there are rapid helicity transitions that are termed as cross boundary effects [178].

Since the magnetic field outside the NS falls off as  $1/r^3$ , the range over which the magnetic field exceeds critical magnetic field is given by  $r_{\text{cr}} = R(B/B_{\text{cr}})^{1/3} \approx 100R$ . As can be seen in Fig.4.8, the oscillation amplitude reduces as we go away from the NS and almost vanishes for  $r > 200R$  in the case for nonrotating fields. If we consider the effect of field rotation then according to Eq. (4.74) the critical magnetic field required to sustain oscillations increases. For  $\dot{\phi} = 10$ , the  $B_{\text{cr}} \approx 6 \times 10^8 \text{ G}$ . Thus the range over which oscillation amplitudes are finite decreases to  $\approx 50R$ .

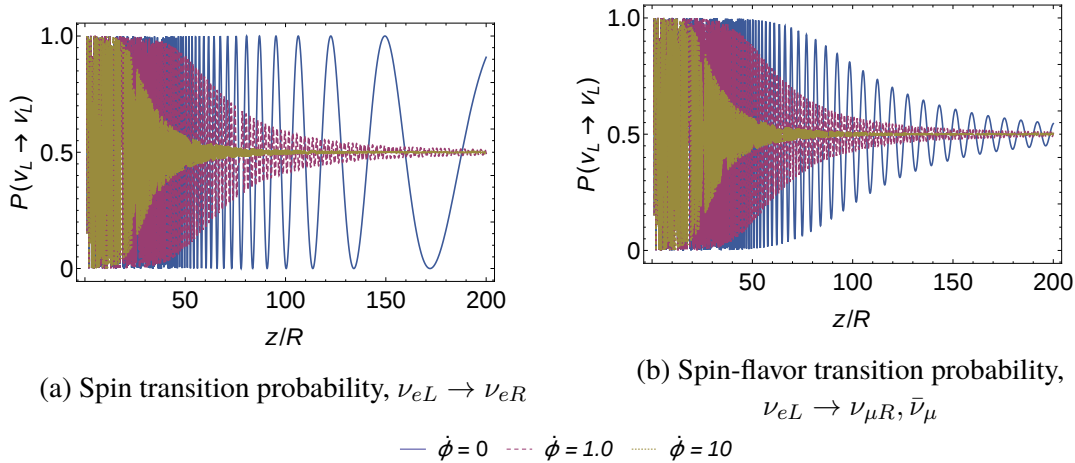


Figure 4.8: Neutrino survival probability of spin and spin-flavor precession for various values of the rotation frequency. Nonzero values of  $\dot{\phi}$  lead to suppression of transitions and the probability converges to one-half at a faster rate compared to the case when  $\dot{\phi} = 0$ . For the case of spin transitions in nonrotating magnetic fields the probability does not converge to 0.5 but instead approaches 1 in the limit  $z \gg R$ . This is because for this case  $\cos \theta_{\text{eff}} = 0$  and the oscillatory term in Eq. (4.71) converges to 1 in the limit  $z \gg R$ .

## 4.5 Possible methods of geometric phase detection

The usual method of geometric phase detection employs experiments wherein a beam is split into two parts, both parts undergo evolution along different paths in parameter space, and then they are made to interfere. The resulting interference pattern bears the signature of the geometric phase. However, these types of experiments are not feasible in case of neutrinos due to their small interaction cross section that renders them practically impossible to maneuver.

Another approach, which has become popular in recent years, is that of quantum simulation. In this approach quantum systems that cannot be accessed experimentally are simulated using a controllable physical system underlying the same mathematical model [179]. The possibility of studying neutrino systems by quantum simulation has been explored in [162, 180]. In [162] it was proposed to detect the neutrino geometric phases using the nuclear magnetic resonance (NMR) setup with a controllable range of parameters. Here we propose an analogous NMR experiment where parameters can be varied to simulate the

environment of neutrino oscillations in magnetic fields. The Hamiltonian for a standard NMR experiment is given by [181]

$$H = -\frac{\omega_0}{2} [\cos \theta \sigma_z + \sin \theta (\sigma_x \cos \omega t + \sigma_y \sin \omega t)], \quad (4.75)$$

where  $\omega_0$  is the Larmor precession frequency of the spins,  $2\theta$  is the angle between the magnetic field direction and the quantization axis, and  $\omega$  is the frequency of the circularly polarized magnetic field. Comparing Eq. (4.75) with the Hamiltonian (4.37) for neutrinos we get the following values for the NMR parameters:

$$\omega_0 = \sqrt{V^2 + (2\mu B)^2}, \quad (4.76)$$

$$\theta = \tan^{-1} \left( \frac{2\mu B}{\sqrt{V^2 + (2\mu B)^2}} \right), \quad (4.77)$$

$$\omega = \dot{\phi}. \quad (4.78)$$

For example, the neutrino oscillation environment outside the NS can be simulated using the following range of parameters:  $\omega_0/2\pi \in (10^6 - 10^3)$  MHz,  $\theta \approx \pi/5$ , and  $\omega/2\pi \in (1.5 - 150)$  kHz. In this way, the geometric phases that arise in neutrino systems can be inferred from those obtained in NMR experiments with a suitably chosen range of parameters.

## 4.6 Conclusions

In this work, we have studied the noncyclic geometric phases associated with neutrino spin and spin-flavor transitions. The dynamics of neutrino spin rotation was examined in the Bloch sphere representation, which clearly brings out the geometric nature of this phenomena. The geometric phase acquired by a neutrino state was shown to be related to the area enclosed by the curve traced by a neutrino spin vector. For the case of cyclic evolution, it was shown that the expressions reduce to the usual Aharonov-Anandan phase

for spin precession in a magnetic field. As a particular case, we analyzed the geometric phases acquired by the solar neutrinos as they propagate outwards under the effect of matter and magnetic fields of the Sun.

Further, we analyzed the situation of neutrinos produced in the NS, propagating outwards under the effect of matter and magnetic fields. We have obtained analytical expressions of the noncyclic geometric phases in the adiabatic approximation and studied their behavior both inside and outside the NS for various cases. We have also studied the transition probability and the cross boundary effects and showed that at a distance of about 200 times the radius of a NS, the initial flux of left-handed neutrinos produced inside the NS is depleted to half of its original value. We would like to point out that we considered only the case of neutrinos produced below resonance regions. However, there might arise situations where there may be significant resonant effects due to both matter and magnetic fields, and it would be interesting to explore these effects in the context of geometric phases.

The emergence of geometric phases in neutrino spin and spin-flavor evolution highlights an important geometric aspect of this phenomena. Even though at present there seems to be no method to detect such phases directly in the current experiments, alternative methods such as quantum simulation have been proposed to detect such phases. The present calculations bring out an essentially geometric character manifest in the neutrino spin rotation and is well worth exploring further.





---

**Mixed state geometric phase for neutrino oscillations**

---

The geometric picture of neutrino oscillations offers a unique way to study the quantum mechanics of this phenomenon. In this picture, the propagation of a neutrino beam is described by a density matrix evolving in a state space with non-trivial geometry. We derive explicit expressions of the mixed state geometric phase which arise during such an evolution for both two and three flavor neutrino oscillations. We show that, in the case of two flavor neutrino oscillations, the geometric phase is independent of the Majorana phase and it can be used as a measure of coherence of the neutrino beam.

This chapter is based on Ref. [182].

## **5.1 Introduction**

The success of the theory of neutrino oscillations has led to many studies exploring the intricacies associated with this phenomenon. In the standard plane wave treatment, the neutrino flavor oscillations arise due to mixing and interference between massive neutrino states. A pictorial way to represent neutrino oscillations is in terms of precession of spin-polarization vector in presence of an effective magnetic field [183, 184]. In particular,

for the case of two-flavor oscillations, the polarization vector becomes three-dimensional and its precession can be easily visualized in both constant and time varying magnetic fields, the magnitude and direction of the magnetic field being specified by the Hamiltonian governing neutrino propagation.

Quantum mechanically, such a precession can be understood in terms of evolution of the state vector in the system's Hilbert space. Such an evolution in the state space with non-trivial geometry gives rise to geometric phase. Let  $\mathcal{H}$  denote the Hilbert space and  $\mathcal{N}$  denote the set of normalized states in  $\mathcal{H}$ . The two vectors  $|\psi_1\rangle, |\psi_2\rangle \in \mathcal{N}$  represent the same physical state if  $|\psi_2\rangle = e^{i\phi} |\psi_1\rangle$  where  $\phi$  is real. The set of physical states is called the projective Hilbert space and is the ray space:  $\mathcal{P} = \mathcal{N}/U(1)$ . If  $\mathcal{H}$  has complex dimension  $n$ , then  $\mathcal{P}$  is a complex projective space of dimension  $n - 1$ ,  $\mathcal{P} = \mathbb{C}P^{n-1}$ . The projection map  $\pi : \mathcal{N} \rightarrow \mathcal{P}$  maps each vector in  $\mathcal{N}$  to its corresponding ray. The above construction defines the principle fibre bundle picture of the state space [144]. The bundle space  $\mathcal{N}$  consists of three parts: the base manifold  $\mathcal{P}$ , the fibre which is group  $U(1)$  element attached to each point of the base manifold, and the map  $\pi : \mathcal{N} \rightarrow \mathcal{P}$ . Now consider the evolution of a normalized state  $|\psi(t)\rangle : t \in [0, \tau]$ . Let the evolution is governed by Schrödinger equation, so that the unitary evolution  $|\psi(0)\rangle \rightarrow |\psi(t)\rangle = \mathcal{U}(t) |\psi(0)\rangle$  traces a curve  $\mathcal{C}$  in  $\mathcal{N}$ . The projection  $\pi : |\psi(t)\rangle \rightarrow |\psi(t)\rangle \langle \psi(t)|$  gives the corresponding curve  $\pi(\mathcal{C}) = \mathcal{C}$  in  $\mathcal{P}$ . The evolution is cyclic if the curve  $\mathcal{C}$  is closed i.e.  $|\psi(\tau)\rangle \langle \psi(\tau)| = |\psi(0)\rangle \langle \psi(0)|$ . In this case the corresponding curve  $\mathcal{C}$  in the bundle space begins and ends on the same fibre such that  $|\psi(\tau)\rangle = e^{i\phi_T} |\psi(0)\rangle$ , where  $\phi_T$  is the total phase acquired by the state during cyclic evolution. Now, there can be infinitely many curves in  $\mathcal{N}$  which project to a given closed curve  $\mathcal{C}$  in  $\mathcal{P}$ . It was shown in [146] that given a curve  $\mathcal{C}$  in  $\mathcal{P}$ , we can define a functional of  $\mathcal{C}$  called geometric phase which is independent of  $\phi_T$  and the curve  $\mathcal{C}$  in the bundle space. The geometric phase is simply obtained by subtracting the dynamical phase from the total phase:

$$\phi_G = \arg\{\langle \psi(0) | \mathcal{U}(\tau) | \psi(0) \rangle\} + i \int_0^\tau dt \langle \psi(0) | \mathcal{U}^\dagger(t) \dot{\mathcal{U}}(t) | \psi(0) \rangle. \quad (5.1)$$

It can be shown that  $\phi_G$  defined above is (i) gauge invariant i.e. invariant under local phase transformations of  $|\psi\rangle$  and (ii) reparametrization invariant i.e. independent of parameter  $t$  of  $\mathcal{C}$ . Thus  $\phi_G$  is independent of the dynamics of  $|\psi(t)\rangle$  and is a geometric property of the curve  $\mathcal{C}$  in  $\mathcal{P}$ . Also since  $|\psi(t)\rangle$  need not be an eigenstate of the Hamiltonian  $H(t)$ , hence the condition of adiabaticity and cyclicity of  $H(t)$  are not required. Thus Eq. (5.1) generalizes the adiabatic Berry phase [132] to non-adiabatic situations. The definition of geometric phase has further been generalized to include non-cyclic and non-unitary evolution [148, 150, 185, 186], which has found numerous applications in physics [134, 187].

Returning to two flavor neutrino oscillations, the Hilbert space in this case is the two dimensional complex space  $\mathcal{H} = \mathbb{C}^2$ . The space of normalized states is the unit sphere  $\mathcal{N} = S^3$ . Thus the projective Hilbert space is the complex projective line  $CP^1 = S^3/U(1)$  which is the Bloch Sphere  $S^2$ . The pure neutrino states correspond to points on the surface of the Bloch sphere. For the case of neutrino oscillations in vacuum or in a medium with constant density, the cyclic evolution of neutrino eigenstates produces a closed curve on  $S^2$ . The resulting geometric phase is equal to the standard expression of one half the solid angle subtended by the closed curve at the centre of the sphere [100].

In the context of neutrinos various authors have derived explicit expressions of geometric phase in different settings, for example, neutrino oscillations in vacuum [156, 157, 159, 160], neutrino oscillations in medium with or without dissipation [154, 155, 158, 161–163, 165], neutrino spin-flavor oscillations [99, 100, 152, 153] and neutrino self-interactions [164]. In all of the above cases the neutrino eigenstate undergoing evolution is considered as a pure state which can be expressed as a coherent superposition of different neutrino states. However, it has been shown that a neutrino produced in a charged-current interaction cannot be described by a pure state [188]. The neutrinos produced in such a process are described by an incoherent superposition which is essentially a mixed state.

In this present work we calculate the mixed state geometric phase for the case of neutrino

oscillations in vacuum using the gauge invariant formulation [189]. We show that our expression of the mixed-state geometric phase generalizes the previously obtained expressions by various authors for both two and three flavor neutrino oscillations. In Section 2, we describe the mixed state geometric phase for unitary evolution. In Section 3, we consider the two flavor case and derive explicit expression of mixed state geometric phase. We also compare the obtained expression of geometric phase with that of quantum coherence. In Section 4, we extend our calculation to three flavor neutrino oscillations and finally conclude in Section 5.

## 5.2 Mixed state geometric phase

The mixed states are mathematically represented by density matrices which are convex sum of pure states projection operators. The notion of geometric phase for mixed state was first proposed by Uhlmann [190] using a procedure known as purification, in which the mixed state density matrix of the system is written as partial trace of a pure state density matrix of an extended system consisting of the given system and an ancilla. An alternative definition of the mixed state geometric phase is given by Sjöqvist *et. al.* [191] which is a direct generalization of the pure state geometric phase. While Uhlmann's formulation of geometric phase is based on purely mathematical ground, the definition by Sjöqvist *et. al.* has a physical interpretation in the context of quantum interferometry [147, 191–193]. For a given unitary evolution, the above two approaches in general yield different results for the mixed state geometric phase. However, both of them reduce to the same expression for the case of pure states [194, 195]. In this chapter we follow the approach formulated by Sjöqvist *et. al.* and its subsequent gauge invariant generalization [189], since its physical implications are more transparent in the context of neutrino oscillations.

Consider a mixed state density matrix undergoing a unitary evolution  $\rho(0) \rightarrow \rho(t) = \mathcal{U}(t)\rho(0)\mathcal{U}^\dagger(t)$  which produces a curve  $\Gamma : t \in [0, \tau]$  in the space of density operators. Let

initial density matrix has the diagonal form

$$\rho(0) = \sum_{k=1}^N w_k |k\rangle \langle k|, \quad (5.2)$$

where  $N$  is the dimension of the Hilbert space. Then unitarily evolved density matrix can be expressed as

$$\rho(t) = \sum_{k=1}^N w_k |k(t)\rangle \langle k(t)|, \quad (5.3)$$

where  $|k(t)\rangle = \mathcal{U}(t) |k\rangle$ . The phase shift acquired by  $\rho(t)$  relative to  $\rho(0)$  is given by [191]

$$\gamma_T = \arg \left\{ \text{Tr}[\mathcal{U}(\tau)\rho(0)] \right\} = \arg \left\{ \sum_{k=1}^N w_k \langle k|k(\tau)\rangle \right\}. \quad (5.4)$$

The above formula can be verified by analyzing the interference pattern in a Mach-Zehnder interferometer where the input beam is the mixed state (5.2). After splitting the beam, one arm of the interferometer is exposed to a variable  $U(1)$  phase shift  $e^{i\chi}$  and the other arm to the unitary operator  $\mathcal{U}(t)$ . On recombining the two beams, the output intensity shows the following interference profile [191]:

$$I = 2(1 + |\text{Tr}[\mathcal{U}(t)\rho(0)]| \cos(\chi - \arg \text{Tr}[\mathcal{U}(t)\rho(0)])). \quad (5.5)$$

The above interference pattern clearly shows that Eq. (5.4) correctly describes the relative phase shifts between  $\rho(0)$  and  $\rho(t)$ . In addition, several experimental tests have confirmed the validity of Eq. (5.4) (see [193] for references).

The dynamical phase for the mixed state can be defined as the time integral of the average of Hamiltonian  $H(t)$

$$\begin{aligned} \gamma_D &= - \int_0^\tau dt \text{Tr}[\rho(t)H(t)] \\ &= -i \int_0^\tau dt \text{Tr}[\rho(0)\mathcal{U}(t)^\dagger \dot{\mathcal{U}}(t)], \end{aligned} \quad (5.6)$$

where  $\tau$  is the total time period. The geometric phase in this case, however, cannot be simply obtained by subtracting accumulated phase (5.6) from the total relative phase (5.4) due to the weight factors appearing in the two terms. To circumvent the issue, one defines the notion of parallel transport in which the dynamical phase (5.6) vanishes identically and thus the phase acquired by the mixed state during evolution is purely geometric. This can be done by requiring  $\rho(t)$  and  $\rho(t + dt)$  to be *in phase*, which leads to the condition [191]

$$\text{Tr}[\rho(t)\dot{\mathcal{U}}(t)\mathcal{U}(t)^\dagger] = 0. \quad (5.7)$$

However, the condition (5.7) is not sufficient and a stronger condition is required, in which each eigenstate of the density matrix is parallel transported [191]:

$$\langle k|\mathcal{U}(t)^\dagger\dot{\mathcal{U}}(t)|k\rangle = 0, \quad k = 1, 2, \dots, N. \quad (5.8)$$

It has been shown that one can incorporate the above conditions in a gauge invariant functional which depends only on the curve  $\Gamma$  and has the following form [189]:

$$\gamma_G = \arg \left\{ \sum_k w_k \langle k|k(\tau)\rangle \exp \left( - \int_0^\tau dt \langle k(t)|\dot{k}(t)\rangle \right) \right\}. \quad (5.9)$$

It can be seen that imposing the parallel transport conditions (5.8), the above expression reduces to the total phase (5.4). Also, for the case of pure states undergoing cyclic evolution, Eq. (5.9) reduces to the geometric phase (5.1). Thus Eq. (5.9) provides a gauge invariant expression for the mixed state geometric phase.

### 5.3 Two flavor neutrino oscillations

The case of two flavor neutrino oscillations gives us a useful toy model to study the important quantum mechanical features of the phenomenon. In this case the space of mixed

states is the unit ball in  $\mathbb{R}^3$ , also called as Bloch ball. Pure neutrino states lie on the extremal points of the Bloch ball, which correspond to the Bloch sphere  $S^2$ . Thus a general mixed state can be represented as a point in the interior of the Bloch sphere. As the neutrinos undergo flavor oscillations, the unitary evolution of the mixed state traces a curve on a spherical shell with radius equal to length of the initial polarization vector. Due to non-trivial geometry of the underlying state space the above curve gives rise to geometric phase which can be calculated using Eq. (5.9).

To this end, we consider a beam of neutrinos characterized by the following density matrix in the flavor basis

$$\hat{\rho} = \sum_{\alpha=e,\mu} w_{\alpha} |\nu_{\alpha}\rangle \langle \nu_{\alpha}|, \quad (5.10)$$

where  $w_{\alpha}$  is the initial statistical weight of the flavor state  $|\nu_{\alpha}\rangle$ , such that  $\sum_{\alpha} w_{\alpha} = 1$ . The density matrix (5.10) describes an incoherent mixture of different neutrino flavors, which are generated in a single or multiple weak interaction processes [4, 188]. The flavor states are related to mass eigenstates via unitary transformation

$$|\nu_{\alpha}\rangle = \sum_{i=1,2} U_{\alpha i}^* |\nu_i\rangle, \quad (5.11)$$

where  $U$  is called mixing matrix. For vacuum oscillations,  $|\nu_i\rangle$  are the eigenstates of the propagation Hamiltonian with energy eigenvalue  $E_i = \sqrt{p_i^2 + m_i^2}$ , where  $p_i$  and  $m_i$  represent the momentum and mass of the  $i$ th mass eigenstate. The mixing matrix, for the case of two flavor oscillations in vacuum, can be expressed as

$$U = \begin{pmatrix} \cos \theta & e^{i\phi} \sin \theta \\ -e^{-i\phi} \sin \theta & \cos \theta \end{pmatrix}, \quad (5.12)$$

where  $\theta$  is the vacuum mixing angle and  $\phi$  is the Majorana phase. In the standard plane wave approximation, the Schrödinger evolution of the mass eigenstates is given by

$$|\nu_i(x, t)\rangle = e^{-iE_i t + ip_i x} |\nu_i\rangle, \quad (5.13)$$

where the space-time interval  $(x, t)$  is the separation between the propagation and production point, and we have written  $|\nu_i(0, 0)\rangle$  as  $|\nu_i\rangle$  for brevity. For the case of *ultra-relativistic* neutrinos, one can employ the approximation  $x \approx t$ , under which Eq. (5.13) becomes

$$|\nu_i(t)\rangle = e^{-im_i^2 t/2E} |\nu_i\rangle, \quad (5.14)$$

where  $E$  represents the neutrino energy obtained after neglecting the mass contributions. Thus the time evolution of the flavor states (5.11) can be written as

$$|\nu_\alpha(t)\rangle = \sum_i U_{\alpha i}^* e^{-im_i^2 t/2E} |\nu_i\rangle. \quad (5.15)$$

The amplitude of  $\nu_\alpha \rightarrow \nu_\beta$  transition can now be obtained using Eq. (5.11) and Eq. (5.15)

$$\psi_{\alpha\beta}(t) = \langle \nu_\beta | \nu_\alpha(t) \rangle = \sum_i U_{\alpha i}^* U_{\beta i} e^{-im_i^2 t/2E}. \quad (5.16)$$

The initial state of the neutrino beam is described by the density matrix

$$\rho(0) = \begin{pmatrix} w_e & 0 \\ 0 & w_\mu \end{pmatrix}. \quad (5.17)$$

As the beam propagates in space, the state undergoes a unitary evolution  $\rho(t) = \mathcal{U}(t)\rho(0)\mathcal{U}(t)^\dagger$ , where  $\mathcal{U}(t)$  is the unitary evolution operator given by

$$\mathcal{U}(t) = \begin{pmatrix} \psi_{ee}(t) & \psi_{\mu e}(t) \\ \psi_{e\mu}(t) & \psi_{\mu\mu}(t) \end{pmatrix}. \quad (5.18)$$

The density matrix at time  $t$  can be written using Eq. (5.17) and Eq. (5.18)

$$\rho(t) = \begin{pmatrix} w_e |\psi_{ee}(t)|^2 + w_\mu |\psi_{\mu e}(t)|^2 & (w_e - w_\mu) \psi_{ee}(t) \psi_{e\mu}^*(t) \\ (w_e - w_\mu) \psi_{ee}^*(t) \psi_{e\mu}(t) & w_e |\psi_{e\mu}(t)|^2 + w_\mu |\psi_{\mu\mu}(t)|^2 \end{pmatrix}, \quad (5.19)$$

where we have used the unitarity relation

$$\psi_{ee} \psi_{e\mu}^* = -\psi_{\mu e} \psi_{\mu\mu}^*. \quad (5.20)$$

The explicit form of the transition amplitudes can be obtained using Eq. (5.12) and Eq. (5.16) :

$$\begin{aligned} \psi_{ee}(t) &= e^{i\omega_p t/2} \cos^2 \theta + e^{-i\omega_p t/2} \sin^2 \theta, \\ \psi_{e\mu}(t) &= -e^{-i\phi} (e^{i\omega_p t/2} - e^{-i\omega_p t/2}) \sin \theta \cos \theta, \\ \psi_{\mu e}(t) &= -e^{i\phi} (e^{i\omega_p t/2} - e^{-i\omega_p t/2}) \sin \theta \cos \theta, \\ \psi_{\mu\mu}(t) &= e^{i\omega_p t/2} \sin^2 \theta + e^{-i\omega_p t/2} \cos^2 \theta, \end{aligned} \quad (5.21)$$

where  $\omega_p = \Delta m^2 / 2E$ ,  $\Delta m^2 = m_2^2 - m_1^2$  being the mass-squared difference.  $\omega_p$  can be physically interpreted as a precession frequency. To see this, consider the neutrino Hamiltonian in the flavor basis

$$H_f = \frac{\Delta m^2}{4E} \begin{pmatrix} -\cos 2\theta & e^{i\phi} \sin 2\theta \\ e^{-i\phi} \sin 2\theta & \cos 2\theta \end{pmatrix} = \frac{\omega_p}{2} \mathbf{B} \cdot \boldsymbol{\sigma}, \quad (5.22)$$

where  $\mathbf{B} = (\sin 2\theta \cos \phi, -\sin \theta \sin \phi, -\cos 2\theta)$  and  $\boldsymbol{\sigma}$  are the Pauli matrices. An equivalent way to express Eq. (5.21) is in the following form [196]:

$$\rho(t) = \frac{1}{2} (1 + \mathbf{P}(t) \cdot \boldsymbol{\sigma}), \quad (5.23)$$

where  $\mathbf{P} = (P_x, P_y, P_z)$  is called polarization vector. The evolution of density matrix is given by von Neumann equation:

$$i\frac{d\rho}{dt} = [H_f, \rho]. \quad (5.24)$$

For the given Hamiltonian (5.22) and density matrix (5.23), we obtain

$$\frac{d\mathbf{P}}{dt} = \omega_p(\mathbf{B} \times \mathbf{P}). \quad (5.25)$$

The geometric interpretation of neutrino oscillations can now be clearly seen from Eq. (5.22) and Eq. (5.25). Specifically, Eq. (5.25) represents the precession of polarization vector  $\mathbf{P}$  around a magnetic field  $\mathbf{B}$ , with precession frequency  $\omega_p$ . The initial value of polarization vector can be obtained by comparing Eq. (5.17) and Eq. (5.23),  $\mathbf{P}(0) = (0, 0, w_e - w_\mu)$ . For the case of pure neutrino states  $w_e = 1(0)$  and  $w_\mu = 0(1)$ . In this case we have  $P_z = \pm 1$ . Thus the neutrino states correspond to points on the unit sphere  $S^2$ ,  $|\nu_e\rangle$  and  $|\nu_\mu\rangle$  being the antipodal points. In addition, Eq. (5.25) shows that for constant  $\mathbf{B}$ , the length of the polarization vector remains unchanged. Thus the precession of the polarization vector will trace a curve on the Bloch sphere. The geometric phase associated with this curve has been calculated for both cyclic [156] and non-cyclic [157] cases.

Now, the general incoherent mixture of neutrino flavor states is described by polarization vector with length less than unity. However, Eq. (5.25) still remains applicable, which implies that during precession the initial length, given by  $P_z(0) = w_e - w_\mu$ , remains unchanged. The precession of the component  $P_z(t)$ , which is related to the transition probabilities, can be obtained by comparing Eq. (5.19) and Eq. (5.23)

$$P_z(t) = (w_e - w_\mu) \left( -1 + 2|\psi_{ee}(t)|^2 \right). \quad (5.26)$$

The precession equations for  $P_x(t)$  and  $P_y(t)$  can be obtained in a similar manner. Geometrically, the precession can be visualized as being described by a cone of length  $P_z(0)$

with axis along  $\mathbf{B}$  and opening angle  $2\theta$ . Thus such a precession will trace a curve  $\Gamma$  on a spherical shell with radius  $P_z(0)$ . To evaluate geometric phase in this case, we first note that the initial density matrix (5.17) is diagonal, so its eigenvectors are simply given by :

$$|e_1\rangle = \begin{pmatrix} 1 \\ 0 \end{pmatrix}, |e_2\rangle = \begin{pmatrix} 0 \\ 1 \end{pmatrix}. \quad (5.27)$$

The eigenvectors of density matrix (5.19) can now be obtained using  $|e_i(t)\rangle = \mathcal{U}(t) |e_i\rangle$ ;  $i = 1, 2$ , which gives

$$|e_1(t)\rangle = \begin{pmatrix} \psi_{ee}(t) \\ \psi_{e\mu}(t) \end{pmatrix}, |e_2(t)\rangle = \begin{pmatrix} \psi_{\mu e}(t) \\ \psi_{\mu\mu}(t) \end{pmatrix}. \quad (5.28)$$

Now using expression (5.9), we obtain the following form for the geometric phase:

$$\begin{aligned} \gamma_G = \arg \left\{ w_e \psi_{ee}(\tau) \exp \left( - \int_0^\tau dt (\psi_{ee}^*(t) \dot{\psi}_{ee}(t) + \psi_{e\mu}^*(t) \dot{\psi}_{e\mu}(t)) \right) \right. \\ \left. + w_\mu \psi_{\mu\mu}(\tau) \exp \left( - \int_0^\tau dt (\psi_{\mu e}^*(t) \dot{\psi}_{\mu e}(t) + \psi_{\mu\mu}^*(t) \dot{\psi}_{\mu\mu}(t)) \right) \right\}. \quad (5.29) \end{aligned}$$

Substituting the explicit values of probability amplitudes from Eq. (5.21), we obtain

$$\begin{aligned} \gamma_G = \arg \left\{ w_e (e^{i\omega_p\tau/2} \cos^2 \theta + e^{-i\omega_p\tau/2} \sin^2 \theta) e^{-i\omega_p\tau \cos 2\theta/2} \right. \\ \left. + w_\mu (e^{i\omega_p\tau/2} \sin^2 \theta + e^{-i\omega_p\tau/2} \cos^2 \theta) e^{i\omega_p\tau \cos 2\theta/2} \right\}. \quad (5.30) \end{aligned}$$

Finally after rearranging the terms, we can write this equation as

$$\gamma_G = \tan^{-1} \left( \frac{(w_e - w_\mu) \left( - \tan(\omega_p\tau \cos 2\theta/2) + \cos 2\theta \tan(\omega_p\tau/2) \right)}{1 + \cos 2\theta \tan(\omega_p\tau/2) \tan(\omega_p\tau \cos 2\theta/2)} \right). \quad (5.31)$$

The above expression constitutes the central result of the chapter. An important point to observe in Eq. (5.31) is that it is independent of the Majorana phase  $\phi$ . Thus the mixed state geometric phase for two flavor neutrino oscillations does not distinguish between Dirac and Majorana neutrinos. Since the geometric phase depends only on the curve  $\Gamma$ ,

during the evolution both Dirac and Majorana neutrino flavor states trace the same curve in the space of density operators, despite having different evolutions in the Hilbert space.

It can be shown that for pure neutrino states the geometric phase (5.31) reduces to earlier obtained results by various authors.

(i) *Noncyclic geometric phase.* Consider the evolution of state  $|\nu_e\rangle$ , for which  $w_e = 1$  and  $w_\mu = 0$ . Substituting these weight factors in (5.31), we obtain

$$\gamma_G^P = -\frac{\omega_p \tau}{2} \cos 2\theta + \tan^{-1} \left( \cos 2\theta \tan \frac{\omega_p \tau}{2} \right). \quad (5.32)$$

This is the noncyclic geometric phase for the pure flavor state  $|\nu_e\rangle$  as obtained in Ref. [157].

(ii) *Aharonov-Anandan phase.* Let us now consider the cyclic evolution of the mixed state which corresponds to  $\tau = 2\pi/\omega_p$ . In this case (5.31) becomes

$$\gamma_G^{AA} = \tan^{-1} \left( (w_e - w_\mu) \tan (\Omega/2) \right), \quad (5.33)$$

where  $\Omega = 2\pi(1 - \cos \theta)$  is the solid angle subtended by the curve  $\Gamma$  at the centre of the sphere. For the pure neutrino states, we obtain the expression

$$\gamma_G^{AA} = \pm\pi(1 - \cos \theta), \quad (5.34)$$

where positive and negative signs correspond to  $|\nu_e\rangle$  and  $|\nu_\mu\rangle$  respectively. The expression (5.34) is the Aharonov-Anandan phase obtained in Ref. [156].

(iii) *Neutrino propagation in non-dissipative matter.* In presence of a medium, the neutrino oscillation parameters are modified due to coherent forward scattering of the neutrinos with the background particles. If the medium has constant density, the modification is of the form :  $\theta \rightarrow \theta_m$  and  $\Delta m^2 \rightarrow \Delta m_m^2$ , where  $\theta_m$  and  $\Delta m_m^2$  are mixing angle and mass-squared difference in the medium. The cyclic geometric phase (5.34) in this case

becomes

$$\gamma_G^{AA} = \pm\pi(1 - \cos\theta_m) = \pm\pi \left[ 1 - \frac{\cos\theta - V}{\sqrt{1 - 2V\cos\theta + V^2}} \right], \quad (5.35)$$

where  $V = 2EV_{cc}/\Delta m^2$ ,  $V_{cc}$  being the charged-current potential. Thus we obtain the result derived in Ref. [161] for neutrino geometric phase in dissipation-less matter.

### 5.3.1 Geometric phase versus quantum coherence

The study of coherence properties of neutrino beams can offer useful insights about the neutrino propagation in a medium [197, 198]. The form of Eq. (5.31) shows explicit dependence of geometric phase on the quantity  $w_e - w_\mu$ , which is the relative amount of  $\nu_e$  and  $\nu_\mu$  neutrinos present in the beam. For a maximally incoherent beam in which  $w_e = w_\mu$ , the geometric phase (5.31) vanishes. Thus the expression (5.31) carries the information about the coherence content of the neutrino beam. Recently, quantum coherence in neutrino oscillations has been studied using tools from quantum information theory [199], wherein coherence is quantified using the  $l_1$ -norm:

$$C(\rho) = \frac{1}{d-1} \sum_{\substack{k,j \\ k \neq j}} |\rho_{k,j}|, \quad (5.36)$$

where  $\hat{\rho}$  is  $d \times d$  representation of the density matrix of the system in a given basis. In our case, using the expression (5.19) for the density matrix, we have

$$\begin{aligned} C(\rho) &= 2|(w_e - w_\mu)| |\psi_{ee}\psi_{e\mu}| \\ &= 2|(w_e - w_\mu)| |\sin 2\theta \sin(\omega_p t/2)| \\ &= |(1 - \sin^2 2\theta \sin^2(\omega_p t/2))^{1/2}|. \end{aligned} \quad (5.37)$$

Comparing Eq. (5.37) with the expression of geometric phase (5.19), we see that both the quantities are sensitive to the factor  $w_e - w_\mu$ , which defines the coherence content of the neutrino beam. In Figure 5.1 we plot the two quantities as a function of  $w_e - w_\mu$  for

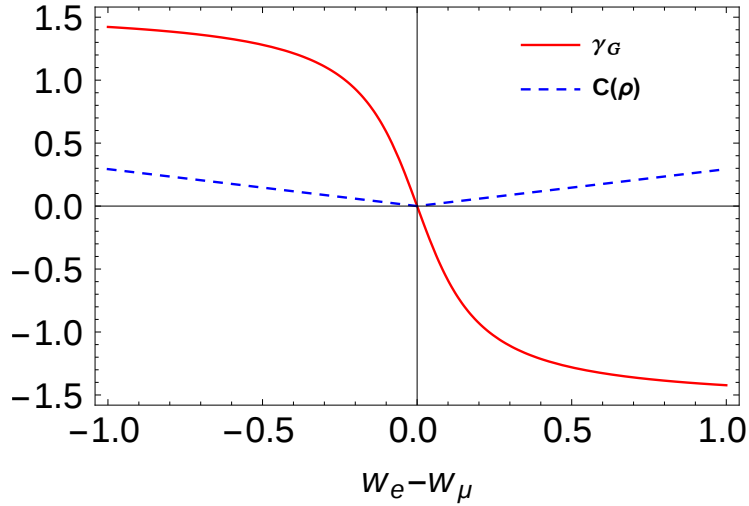


Figure 5.1: Comparison of mixed state geometric phase (5.31) and quantum coherence (5.37) with respect to coherence parameter  $w_e - w_\mu$ . The neutrino oscillation parameters are taken as:  $\Delta m^2 = 2.5 \times 10^{-3} \text{ eV}^2$ ,  $\theta = 48.6^\circ$ ,  $L/E = 520 \text{ (km/GeV)}$ .

typical oscillation parameters. It can be clearly seen that as the neutrino beam becomes more coherent, both geometric phase (5.31) and quantum coherence (5.37) reach their respective maximum values. Also, for completely incoherent beam they both vanish. Thus both quantities contain information about the *quantumness* of the neutrino beam and can be considered as a measure of coherence for two-flavor neutrino oscillations.

## 5.4 Three flavor oscillations

Let us now consider the case of three flavor neutrino oscillations. In this case the geometric picture of neutrino oscillations involves precession of an eight dimensional polarization vector around a magnetic field [6]. The space of density operators corresponds to  $SU(3)/(U(1) \times U(1))$ , when the density matrix has non-degenerate eigenvalues [200]. Even though pictorial representation is too complicated to visualize for three flavor oscillations, most of the mathematical expressions admit a straightforward generalization of the results in the preceding section.

The neutrino beam is described by initial density matrix

$$\rho(0) = \text{Diag}(w_e, w_\mu, w_\tau). \quad (5.38)$$

The evolution of neutrino flavor states is governed by the unitary operator

$$\mathcal{U}(t) = \begin{pmatrix} \psi_{ee}(t) & \psi_{\mu e}(t) & \psi_{\tau e}(t) \\ \psi_{e\mu}(t) & \psi_{\mu\mu}(t) & \psi_{\tau\mu}(t) \\ \psi_{e\tau}(t) & \psi_{\mu\tau}(t) & \psi_{\tau\tau}(t) \end{pmatrix}, \quad (5.39)$$

where the transition amplitudes are given by

$$\psi_{\alpha\beta}(t) = \sum_i U_{\alpha i}^* U_{\beta i} e^{-iE_i t}, \quad (5.40)$$

where  $E_i = m_i^2/2E$ ;  $i = 1, 2, 3$ . For the mixing matrix  $U$ , we assume the standard Dirac parametrization with three mixing angles  $\theta_{12}$ ,  $\theta_{13}$ ,  $\theta_{23}$  and a CP (charge-conjugation and parity)-violating phase  $\delta$  (Eq.(1.65)). The time evolved density matrix  $\rho(t) = \mathcal{U}(t)\rho(0)\mathcal{U}^\dagger(t)$  can now be written as

$$\rho(t) = \sum_{\alpha=e,\mu,\tau} w_\alpha \begin{pmatrix} \psi_{\alpha e}(t) \\ \psi_{\alpha\mu}(t) \\ \psi_{\alpha\tau}(t) \end{pmatrix} \begin{pmatrix} \psi_{\alpha e}^*(t) & \psi_{\alpha\mu}^*(t) & \psi_{\alpha\tau}^*(t) \end{pmatrix}, \quad (5.41)$$

where  $|e_\alpha\rangle = (\psi_{\alpha e} \ \psi_{\alpha\mu} \ \psi_{\alpha\tau})^T$ ,  $\alpha = e, \mu, \tau$  are the eigenvectors of  $\rho$ . The geometric phase can now be obtained from Eq. (5.9):

$$\gamma_G = \arg \left\{ \sum_{\alpha=e,\mu,\tau} w_\alpha \psi_{\alpha\alpha}(\tau) \exp \left( - \int_0^\tau dt \sum_{\beta=e,\mu,\tau} \psi_{\alpha\beta}^*(t) \dot{\psi}_{\alpha\beta}(t) \right) \right\}, \quad (5.42)$$

which is a simple generalization of Eq. (5.29). However it is too complicated to write Eq. (5.42) in a form analogous to Eq. (5.31). A relatively simpler expression can be obtained for pure states. Let us consider the geometric phase for  $|\nu_e\rangle$ , for which Eq. (5.42) reduce

to

$$\gamma_G^P = \arg \left\{ \psi_{ee}(\tau) \exp \left( - \int_0^\tau dt \sum_{\beta=e,\mu,\tau} \psi_{e\beta}^*(t) \dot{\psi}_{e\beta}(t) \right) \right\}. \quad (5.43)$$

Substituting  $\psi_{\alpha\beta}$  from Eq. (5.40), we obtain the following expression:

$$\begin{aligned} \gamma_G^P = \tan^{-1} & \frac{\cos 2\theta_{12} \cos^2 \theta_{13} \sin \xi\tau - \sin^2 \theta_{13} \sin ((2q-1)\xi\tau)}{\cos^2 \theta_{13} \cos \xi\tau + \sin^2 \theta_{13} \cos ((2q-1)\xi\tau)} \\ & + (2 \sin^2 \theta_{12} \cos^2 \theta_{13} + 2q \sin^2 \theta_{13} - 1) \xi\tau, \end{aligned} \quad (5.44)$$

where  $\xi = (E_2 - E_1)/2 = \Delta m_{21}^2/4E$  and  $q = (E_3 - E_1)/(E_2 - E_1) = \Delta m_{31}^2/\Delta m_{21}^2$ .

The above expression matches the pure state geometric phase for  $|\nu_e\rangle$  derived in Ref. [157].

Note that Eq. (5.44) is independent of the CP-violating phase  $\delta$ . However, it can be shown that the pure state geometric phases for  $|\nu_\mu\rangle$  and  $|\nu_\tau\rangle$  include non-trivial dependence on  $\delta$ .

## 5.5 Conclusions

Neutrino oscillations represent a phenomenon in which quantum mechanical effects are observed at long distance scales. This provides us the opportunity to study the quantum mechanical features of this system such as geometric phase and quantum coherence in a unique manner. In particular, the appearance of geometric phases in neutrino oscillations have been pointed out in several previous studies. However, all of them consider the case of pure neutrino states, which cannot be realized in a typical scenario.

In this work, we consider the more general case of an incoherent beam of neutrinos, and derive the expressions for geometric phase in both two flavor and three flavor models. We discussed the geometry of the state space of neutrino oscillations and its connection with the appearance of a geometric phase. For two flavor oscillations, the geometric phase is shown to be independent of the Majorana phase, however for three flavor oscillations the geometric phase shows non-trivial dependence on the Dirac CP-violating phase. We also

show that our results generalize the previously obtained expressions of the pure state geometric phase for neutrino oscillations in vacuum and in non-dissipative matter. In addition, the comparison between geometric phase and information-theoretic quantum coherence is also highlighted.



---

**Summary and Outlook**

---

Over the past several years the phenomenon of neutrino oscillations has been firmly established on experimental grounds. The basic parameters of neutrino oscillations have been determined to a satisfactory precision. However, several challenges still remain which can only be settled by further experiments. Some of these include determination of neutrino mass hierarchy, precise measurement of Dirac CP violating phase, more stringent bounds on the neutrino magnetic moments and the absolute neutrino masses, and the determination of Dirac or Majorana nature of neutrino. The present theoretical effort is to complement the experimentation by pointing out new features of the theory and their possible implications in the phenomenon of neutrino oscillations.

In this Thesis, we studied some of these features in the context of neutrino flavor and spin-flavor oscillations. In Chapter 2 we studied the electromagnetic properties of the neutrinos. We showed that the Dirac and Majorana neutrinos exhibit differences with respect to their electromagnetic character. It was shown that existence of finite neutrino mass imply the presence of non-zero magnetic moment. We also discussed the present experimental bounds in the neutrino magnetic moments and the viability of the theoretical models for generating large magnetic moments  $\sim 10^{-11}\mu_B$ . We then studied the interaction of

neutrino magnetic moments with classical background electromagnetic fields and derived the Hamiltonian for Dirac and Majorana neutrinos in case of two-neutrino mixing. In this case it is possible for neutrinos to undergo spin-flavor oscillations in which both the spin-flip and flavor change of neutrinos occur simultaneously. It was shown that the neutrino spin-flavor oscillations gives rise to the possibility of resonance in two new channels, in addition to the usual MSW resonance, which is termed as SFP (spin-flavor precession) resonance.

Neutrino spin-flavor oscillations may play an important role in the solar interiors where magnetic fields may be sufficiently large to cause appreciable neutrino transitions. Thus neutrinos may act as messenger of information about the solar magnetic fields. We explored this idea in sufficient detail in Chapter 3. For this purpose we constructed analytical models for the solar magnetic field in all the three regions of the Sun, based on the current bounds from helioseismology. These bounds vary widely in magnitude especially in the solar core where they range from 30 G to 7 MG. We thus constructed two models: in the first model the magnetic field peaks in the core and then tapers off with distance, and in the second model the magnetic field is negligible in the core and peaks in the radiative zone (RZ) of the Sun. We also obtained a novel parametrization for the electron density profile in the Sun, which provides a better approximation compared to the usual exponential parametrization. We considered the case of Majorana neutrinos and evaluated the flux of electron antineutrinos reaching the surface of Earth due to the transitions  $\nu_{eL} \rightarrow \bar{\nu}_{\mu R} \rightarrow \bar{\nu}_e$  for both the models of solar magnetic fields. These results are obtained by numerically evaluating the coupled neutrino spin-flavor equations and averaging over the  ${}^8B$  neutrino production region in the Sun. The results from the Borexino experiment are then utilized to place bounds on the two models of solar magnetic field. It is found that whereas the Borexino bounds are too weak to place any upper limit on the RZ magnetic field, for the solar core magnetic field we are able to place an upper bound  $B_0 < 1.1 \times 10^6 \text{G}$ , which is an improvement by a factor of almost one-seventh of the current largest helioseismological bound.

The study of quantum mechanical aspects of neutrino flavor and spin-flavor oscillations brings important new insights about the nature of this phenomenon. For example, the neutrino propagation in a magnetic field and matter can be understood by studying the trajectory of the neutrino spin-polarization vector in the projective Hilbert space of the system. This is the theme we study in Chapter 4. The evolution of the neutrino state consisting of two helicity components  $(\nu_L, \nu_R)^T$  in the presence of an effective magnetic field can be studied in the Bloch sphere representation. In this representation, any neutrino state  $|\nu\rangle$  corresponds to a point on the Bloch sphere  $S^2$  and the orthogonal states  $|\nu_L\rangle$  and  $|\nu_R\rangle$  correspond to two antipodal points on  $S^2$ . We first studied the case of spin precession  $\nu_{eL} \rightarrow \nu_{eR}$  of the left-handed electron neutrinos produced in the Sun and propagating outwards under the influence of matter and magnetic fields. In this case the neutrino spin-polarization traces out cyclic and noncyclic curves on the Bloch sphere for different parameters of the Hamiltonian. Such an evolution in quantum mechanics is known to give rise to geometric phase due to non-trivial geometry of the system's projective Hilbert space. We derive analytical expressions for the non-adiabatic and non-cyclic geometric phases and show that the area enclosed by the trajectory traced out by the spin-polarization vector is related to the geometric phases acquired by the neutrino state during the evolution. We also show that for resonant transition  $\nu_{eL} \leftrightarrow \nu_{eR}$  the geometric phase vanishes, since in this case the spin-polarization vector traces out a great circle on  $S^2$ . We then studied the neutrino spin transitions for neutrinos produced in the extreme environments such as neutron stars (NS). For these calculations we used realistic density and magnetic field profiles both in the interior and outer regions of the NS. We showed that while inside the NS the neutrino propagation is highly adiabatic, as the neutrinos come out of the NS the non-adiabatic effects start to become more important as the distance from the surface increases. In the interior region of the NS, the matter effects strongly dominate over the magnetic field, thus the area of the curve traced by spin-polarization vector is negligible, and hence the associated geometric phase is vanishingly small. As the neutrinos come out of the NS, matter effects vanish and neutrino eigenstates develop a significant adiabatic geometric

phase. In addition, we also studied the transition probability and the cross boundary effects and showed that at a distance of about 200 times the radius of a NS, the initial flux of left-handed neutrinos produced inside the NS is depleted to half of its original value.

In Chapter 5 we return to the usual case of neutrino flavor oscillations. The geometric picture of neutrino oscillations offers a unique way to study the quantum mechanics of this phenomenon. In this picture, the propagation of a neutrino beam is described by a density matrix evolving in a state space with non-trivial geometry. Such an evolution is known to give rise to geometric phases in neutrino oscillations, which have been pointed out in several previous studies. However, all of them consider the case of pure neutrino states, which cannot be realized during neutrino production in a charged-current reaction. In this Chapter, we consider the more general case of an incoherent beam of neutrinos, and derive the expressions for geometric phase in both two flavor and three flavor models. We also discuss the geometry of the state space of neutrino oscillations and its connection with the appearance of a geometric phase. For two flavor oscillations, the geometric phase is shown to be independent of the Majorana phase, however for three flavor oscillations the geometric phase shows non-trivial dependence on the Dirac CP-violating phase. In addition, for the case of two flavor neutrino oscillations the geometric phase can be used as a measure of coherence of the neutrino beam. We also show that our results are a generalization of previously obtained expressions of the pure state geometric phase for neutrino oscillations in vacuum and in non-dissipative matter.

In this Thesis we put forward some new ideas and consolidated some of the existing results. The study of neutrino electromagnetic properties can reveal important aspects of neutrinos such as their CP properties and their Dirac or Majorana nature. On the other hand, the study of geometric aspects has divulged important new features of the theory of neutrino oscillations. In this Thesis, we studied a combination these two ideas. Some of the ideas we pursued in this thesis can be expanded in various directions. For example, the geometric nature of neutrino spin-flavor oscillations can be studied in the presence of

random magnetic fields and in dissipative environments, the significance of the CP violating phase on the three flavor neutrino spin-flavor oscillations can be explored in greater detail, the effects of the state space geometry on the neutrino wave-packets and resulting decoherence can also be examined.



---

## Neutrino oscillations, wave packets and decoherence

---

### Introduction

The phenomena of neutrino mixing and oscillations has been firmly established on experimental grounds [201, 202]. The oscillation probability between three different neutrino flavors is characterized by mixing angles and mass squared differences which have been measured in various neutrino experiments [203]. In the standard plane wave treatment of neutrino oscillations, the analytic expression for flavor oscillation probability is derived using certain assumptions. In this appendix we explain these assumptions in detail and show that some of the assumptions cannot be justified. Then we show that in a more general approach involving wave packets, these assumptions are no longer required. In addition, the wave packet approach gives additional insights such as effects of kinematic decoherence and neutrino localization uncertainty on the oscillation probability etc.

The wave packet treatment of neutrinos was first carried out by Nussinov [204] in the context of solar neutrinos. Subsequently detailed analysis of neutrino oscillation have been carried out using plane wave, wave packet and various quantum field theory based formalism [4, 205–208] and an experimental determination of the neutrino wave packet

size has been reported in [209].

This appendix is based on Ref. [210].

## Plane wave treatment of neutrino oscillations

The typical neutrino production and detection processes have the following form:

$$\begin{aligned} W^+ &\rightarrow \bar{l}_\alpha + \nu_\alpha \\ \nu_\beta &\rightarrow W^+ + l_\beta \end{aligned}$$

Neutrinos in flavor state  $|\nu_\alpha\rangle$  are produced in charged current interactions, involving a  $W$  boson, along with charged antilepton  $\bar{l}_\alpha$ . The propagation of neutrinos produced in the flavor state  $|\nu_\alpha\rangle$  is described by the eigenstates of the propagation Hamiltonian called mass eigenstates. The flavor and mass eigenstates are related by the following unitary transformation

$$|\nu_\alpha\rangle = \sum_j U_{\alpha j}^* |\nu_j\rangle. \quad (\text{A.1})$$

Now as the neutrinos propagate from their production point to the detector, they may undergo flavor transformation  $\nu_\alpha \rightarrow \nu_\beta$  and be detected in the flavor state  $|\nu_\beta\rangle$ . This phenomenon of neutrino flavor transformation during propagation is called neutrino oscillation.

If the neutrino mass eigenstates evolve as plane waves, then in the Schrödinger picture we can write:

$$|\nu_j(\mathbf{x}, t)\rangle = e^{-iE_j t + i\mathbf{p}_j \cdot \mathbf{x}} |\nu_j(0)\rangle, \quad (\text{A.2})$$

where  $E_j$  and  $\mathbf{p}_j$  represent the energy and momentum of the  $j$ th mass eigenstate. Using Eq.(A.1) we get neutrino propagation in flavor basis

$$|\nu_\alpha(\mathbf{x}, t)\rangle = \sum_j U_{\alpha j}^* e^{-iE_j t + i\mathbf{p}_j \cdot \mathbf{x}} |\nu_j(0)\rangle \quad (\text{A.3})$$

For neutrinos produced in the state  $|\nu_\alpha\rangle$  at  $(\mathbf{x} = 0, t = 0)$ , the amplitude of flavor transition to state  $|\nu_\beta\rangle$  at  $(\mathbf{x}, t)$  is given by

$$\begin{aligned} \mathcal{A}_{\nu_\alpha \rightarrow \nu_\beta}(\mathbf{x}, t) &= \langle \nu_\beta | \nu_\alpha(\mathbf{x}, t) \rangle \\ &= \sum_{j,k} \langle \nu_k(0) | U_{\alpha j}^* e^{-iE_j t + i\mathbf{p}_j \cdot \mathbf{x}} U_{\beta k} | \nu_j(0) \rangle \\ &= \sum_j U_{\alpha j}^* U_{\beta j} e^{-iE_j t + i\mathbf{p}_j \cdot \mathbf{x}}, \end{aligned} \quad (\text{A.4})$$

where we have used the normalization of mass eigenstates:  $\langle \nu_j | \nu_k \rangle = \delta_{jk}$ . The flavor transition probability is then given by

$$\begin{aligned} \mathcal{P}_{\nu_\alpha \rightarrow \nu_\beta}(\mathbf{x}, t) &= |\mathcal{A}_{\nu_\alpha \rightarrow \nu_\beta}(\mathbf{x}, t)|^2 \\ &= \sum_{j,k} U_{\alpha j}^* U_{\beta j} U_{\alpha k} U_{\beta k}^* e^{-i(\phi_j - \phi_k)}, \end{aligned} \quad (\text{A.5})$$

where  $\phi_j = E_j t - \mathbf{p}_j \cdot \mathbf{x}$ .

Now, let the distance between the source and detector is  $L$ . For macroscopic values of  $L$ , we can assume that the momenta of the neutrino mass eigenstates are aligned along  $\mathbf{x}$ . In this one dimensional approximation, the standard expression of transition probability, which matches well with the experiments, is given by [4]

$$\begin{aligned} \mathcal{P}_{\nu_\alpha \rightarrow \nu_\beta}(L, E) &= \sum_{j,k} U_{\alpha j}^* U_{\beta j} U_{\alpha k} U_{\beta k}^* \exp\left(-i \frac{\Delta m_{jk}^2 L}{2E}\right) \\ &= \sum_{j,k} U_{\alpha j}^* U_{\beta j} U_{\alpha k} U_{\beta k}^* \exp\left(-2\pi i \frac{L}{L_{\text{osc}}^{jk}}\right), \end{aligned} \quad (\text{A.6})$$

where  $L_{\text{osc}}^{jk} = 4\pi E / \Delta m_{jk}^2$  is called the vacuum oscillation length,  $\Delta m_{jk}^2 = m_j^2 - m_k^2$  and  $E$  is the neutrino energy.

There are two ways by which one can derive the oscillation phase of (A.6) from Eq. A.5. In the first method, we make the following two assumptions: (a) The transition probability expression (A.6) involve only the distance of propagation  $L$  and does not involve time. Since neutrinos travel almost at the speed of light, we make approximation that the neutrino propagation time  $t = L$ , thus

$$\phi_j = (E_j - p_j)L = \frac{(E_j^2 - p_j^2)L}{E_j + p_j} \approx \frac{m_j^2}{2E_j}L, \quad (\text{A.7})$$

(b) The mass eigenstates have equal energy  $E_j = E_k = E$ , so that

$$\phi_j - \phi_k \approx \frac{m_j^2 - m_k^2}{2E}L = \frac{\Delta m_{jk}^2}{2E}L. \quad (\text{A.8})$$

Using the above two assumptions in Eq. (A.5) gives us the desired result (A.6). However, even though we obtain the correct expression, it is difficult to justify these assumptions. Firstly, the assumption (a) implies a point like behavior of the particles, which is contrary to the plane wave treatment used in the derivation. Also, the assumption (b) is unrealistic since it ignores the neutrino mass contributions and hence cannot be justified.

There is an other set of assumptions through which one can obtain the standard oscillation probability expression from Eq. (A.5). The oscillation phase is  $\phi_j = \sqrt{p_j^2 + m_j^2}t_j - p_j x$ .

Expanding  $\phi_j$  around an average momentum  $p$  and an average mass  $m$ , we get

$$\begin{aligned}
\phi_j &= \sqrt{(p + \delta p_j)^2 + (m^2 + \delta m_j)^2} t_j - (p + \delta p_j)L \\
&\approx \sqrt{p^2 + m^2 + 2p\delta p_j + \delta m_j^2} t_j - (p + \delta p_j)L \\
&\approx E \left( 1 + \frac{2p\delta p_j + \delta m_j^2}{E^2} \right)^{1/2} t_j - (p + \delta p_j)L \\
&\approx Et_j + \frac{1}{2E} (2p\delta p_j + \delta m_j^2) t_j - (p + \delta p_j)L \\
&= (Et - pL) + \frac{\delta m_j^2}{2E} t + (vt - L)\delta p_j + e\delta t_j,
\end{aligned} \tag{A.9}$$

where propagation time of each mass eigenstate is expanded around an average value  $t_j = t + \delta t_j$ , and  $E = \sqrt{p^2 + m^2}$  and  $v = p/E$  are average energy and velocity respectively. If we now make the following assumptions: (a) Equal time prescription:  $\delta t_j = 0$  i.e. interference only takes place for equal times for different mass eigenstates and (b) classical propagation condition:  $vt - L = 0$ . Then the phase difference becomes

$$\phi_j - \phi_k = \frac{\delta m_{jk}^2 L}{2Ev} = \frac{\delta m_{jk}^2 L}{2p}. \tag{A.10}$$

Again, since the plane waves are delocalized in space-time, these assumptions cannot be justified and a more realistic treatment involving wave packets is required.

## Intermediate wave packet model

It is clear from above discussion that the plane wave description contains many ad-hoc assumptions and does not provide the complete understanding of neutrino oscillations. In addition, the plane wave treatment seems unreasonable since both neutrino production and detection are localized processes which also involve the uncertainty in the energy-momentum of neutrinos. Many of these issues can be resolved using intermediate wave

packet model, in which each propagating neutrino mass eigenstate is modeled as a wave packet.

For definiteness, we assume that the mass eigenstate wave packets in momentum space have the following Gaussian form

$$\psi_j(\mathbf{p}, \mathbf{p}_j, \sigma_{pP}) = \frac{1}{(\sqrt{2\pi}\sigma_{pP})^{3/2}} \exp\left(-\frac{(\mathbf{p} - \langle \mathbf{p}_j \rangle)^2}{4\sigma_{pP}^2}\right), \quad (\text{A.11})$$

where  $\sigma_{pP}$  is the momentum width of each mass eigenstate in the production process and is same along all three directions and  $\langle \mathbf{p}_j \rangle$  is the average momentum of the  $j$ th mass eigenstate. In coordinate space representation, the wave packets are given by

$$\psi_j(\mathbf{x}, t) = \int \frac{d\mathbf{p}}{(2\pi)^{3/2}} \psi_j(\mathbf{p}, \mathbf{p}_j, \sigma_{pP}) e^{i\mathbf{p}\cdot\mathbf{x} - iE_j(\mathbf{p})t}. \quad (\text{A.12})$$

We assume that the Gaussian wave packets are sharply peaked around the average momentum  $\langle \mathbf{p}_j \rangle$ , so we can Taylor expand  $E_j(\mathbf{p})$  as

$$E_j(\mathbf{p}) \approx E_j(\langle \mathbf{p}_j \rangle) + \left. \frac{\partial E_j}{\partial \mathbf{p}} \right|_{\mathbf{p}=\langle \mathbf{p}_j \rangle} (\mathbf{p} - \langle \mathbf{p}_j \rangle). \quad (\text{A.13})$$

We write

$$E_j(\langle \mathbf{p}_j \rangle) = \sqrt{\langle \mathbf{p}_j \rangle^2 + m_j^2} = \langle E_j \rangle, \quad (\text{A.14})$$

$$\left. \frac{\partial E_j}{\partial \mathbf{p}} \right|_{\mathbf{p}=\langle \mathbf{p}_j \rangle} = \frac{\langle \mathbf{p}_j \rangle}{\langle E_j \rangle} = \mathbf{v}_j, \quad (\text{A.15})$$

where  $\mathbf{v}_j$  is the group velocity of each wave packet. The coordinate space wave packet then becomes

$$\begin{aligned}\psi_j(\mathbf{x}, t) &= \int \frac{d\mathbf{p}}{(2\pi)^{3/2}} \frac{1}{(\sqrt{2\pi}\sigma_{pP})^{3/2}} \exp\left[-\frac{(\mathbf{p} - \langle\mathbf{p}_j\rangle)^2}{4\sigma_{pP}^2}\right] \times \\ &\quad \exp\left[i\mathbf{p} \cdot \mathbf{x} - i(\langle E_j\rangle t + \mathbf{v}_j \cdot (\mathbf{p} - \langle\mathbf{p}_j\rangle)^2)\right] \\ &= \frac{1}{(\sqrt{2\pi}\sigma_{xP})^{3/2}} \exp\left[i(\langle\mathbf{p}_j\rangle \cdot \mathbf{x} - \langle E_j\rangle t) - \frac{(\mathbf{x} - \mathbf{v}_j t)^2}{4\sigma_{xP}^2}\right],\end{aligned}\quad (\text{A.16})$$

where  $\sigma_{xP} = 1/2\sigma_{pP}$  is the width of wave packet in the coordinate space. The neutrino flavor state in coordinate space representation is given by

$$|\nu_\alpha(\mathbf{x}, t)\rangle = \sum_j U_{\alpha j}^* \psi_j(\mathbf{x}, t) |\nu_j(0)\rangle. \quad (\text{A.17})$$

Comparing this with Eq. (A.3) elucidates the difference between the plane wave and wave packet formalism. Now consider the detection process in which a neutrino is detected in flavor state  $|\nu_\beta\rangle$  at a distance  $L$  and after time  $t$  from the point of production. The detected neutrino is described by the wave packet [211]

$$|\nu_\beta\rangle = \sum_j U_{\beta j}^* \int d\mathbf{p} \psi_j(\mathbf{p}, \mathbf{p}_j, \sigma_{pD}) |\nu_j(\mathbf{p})\rangle. \quad (\text{A.18})$$

Here  $\sigma_{pD}$  represents the momentum width of wave packets in detection process. The average momenta  $\mathbf{p}_j$  of the mass eigenstates of detected neutrinos is assumed to be same as that of incoming wave packets in Eq. (A.11). Also the state  $|\nu_\beta\rangle$  does not evolve in time as it does not represent propagating neutrinos. If the neutrinos are detected at distance  $L$  from the production point, the coordinate space wave function of detected neutrino is given by

$$|\nu_\beta(\mathbf{x} - \mathbf{L})\rangle = \frac{1}{(\sqrt{2\pi}\sigma_{xD})^{3/2}} \exp\left[i\langle\mathbf{p}_j\rangle \cdot (\mathbf{x} - \mathbf{L}) - \frac{(\mathbf{x} - \mathbf{L})^2}{4\sigma_{xD}^2}\right], \quad (\text{A.19})$$

where  $\sigma_{xD} = 1/\sigma_{pD}$ . The transition amplitude is then given by

$$\begin{aligned} \mathcal{A}_{\nu_\alpha \rightarrow \nu_\beta}(\mathbf{L}, t) &= \int d\mathbf{x} \langle \nu_\beta(\mathbf{x} - \mathbf{L}) | \nu_\alpha(\mathbf{x}, t) \rangle \\ &= \sqrt{\frac{2\sigma_{xP}\sigma_{xD}}{\sigma_x^2}} \sum_j U_{\alpha j}^* U_{\beta j} \exp \left[ i(\langle \mathbf{p}_j \rangle) \cdot \mathbf{L} - \langle E_j \rangle t - \frac{(\mathbf{L} - \mathbf{v}_j t)^2}{4\sigma_x^2} \right], \end{aligned} \quad (\text{A.20})$$

where  $\sigma_x^2 = \sigma_{xP}^2 + \sigma_{xD}^2$  is the effective width which depends on both production and detection processes. In a typical neutrino experiment, the distance  $L$  between the source and detector is fixed whereas time  $t$  is not measured. The quantity that is measured in experiments is the transition probability at a fixed distance, obtained by averaging over time

$$\mathcal{P}_{\nu_\alpha \rightarrow \nu_\beta}(\mathbf{L}) = \int_0^\infty \left| \mathcal{A}_{\nu_\alpha \rightarrow \nu_\beta}(\mathbf{L}, t) \right|^2 dt. \quad (\text{A.21})$$

After integrating and imposing the normalization condition  $\sum_\beta \mathcal{P}(\nu_\alpha \rightarrow \nu_\beta) = 1$ , we obtain

$$\begin{aligned} \mathcal{P}_{\nu_\alpha \rightarrow \nu_\beta}(\mathbf{L}) &= \sum_{j,k} U_{\alpha j}^* U_{\beta j} U_{\alpha k} U_{\beta k}^* \exp \left[ -i \left( (\langle E_j \rangle - \langle E_k \rangle) \frac{\mathbf{v}_j + \mathbf{v}_k}{v_j^2 + v_k^2} - (\langle \mathbf{p}_j \rangle - \langle \mathbf{p}_k \rangle) \right) \cdot \mathbf{L} \right] \\ &\quad \exp \left[ -\frac{((\mathbf{v}_j - \mathbf{v}_k) \cdot \mathbf{L})^2}{4\sigma_x^2(v_j^2 + v_k^2)} - \frac{(\langle E_j \rangle - \langle E_k \rangle)^2}{4\sigma_p^2(v_j^2 + v_k^2)} \right]. \end{aligned} \quad (\text{A.22})$$

In this expression the first exponential is the interference term which generates oscillations between different neutrino flavors whereas the second exponential contains damping terms which sets conditions for oscillations to be observed. To simplify and compare this expression with the standard plane wave transition probability (A.6), we make following approximations. We first Taylor expand the average momenta  $\langle \mathbf{p}_i \rangle$  around  $m_i = 0$

$$\langle \mathbf{p}_i \rangle = \mathbf{p} + \left. \frac{\partial \langle \mathbf{p}_i \rangle}{\partial m_i^2} \right|_{m_i=0} m_i^2 = \mathbf{p} - \boldsymbol{\xi} \frac{m_i^2}{2E}, \quad (\text{A.23})$$

where  $\mathbf{p}$  and  $E$  are the average momentum and energy of the massless neutrino,  $|\mathbf{p}| = E$  and

$$\frac{\boldsymbol{\xi}}{2E} = - \left. \frac{\partial \langle \mathbf{p}_i \rangle}{\partial m_i^2} \right|_{m_i=0}. \quad (\text{A.24})$$

Similarly for average energy and velocity we obtain

$$\begin{aligned} \langle E_i \rangle &= \sqrt{\langle \mathbf{p}_i \rangle^2 + m_i^2} \approx |\langle \mathbf{p}_i \rangle| + \frac{m_i^2}{2|\langle \mathbf{p}_i \rangle|} \\ &\approx E + \left( 1 - \frac{\mathbf{p} \cdot \boldsymbol{\xi}}{E} \right) \frac{m_i^2}{2E}, \end{aligned} \quad (\text{A.25})$$

and

$$\mathbf{v}_i = \frac{\langle \mathbf{p}_i \rangle}{\langle E_i \rangle} \approx \frac{\mathbf{p}}{E} - \left[ \frac{\mathbf{p}}{E} \left( 1 - \frac{\mathbf{p} \cdot \boldsymbol{\xi}}{E} \right) + \boldsymbol{\xi} \right] \frac{m_i^2}{2E^2}. \quad (\text{A.26})$$

The absolute value of velocity is

$$v_i \approx 1 - \frac{m_i^2}{2E^2}. \quad (\text{A.27})$$

For  $N$  neutrino mass eigenstates the average of the mean momentum  $\langle \mathbf{p}_i \rangle$  is

$$\bar{\mathbf{p}} = \frac{1}{N} \sum_{i=1}^N \langle \mathbf{p}_i \rangle = \mathbf{p} - \boldsymbol{\xi} \frac{\bar{m}^2}{2E}, \quad (\text{A.28})$$

where  $\bar{m}^2 = \sum_{i=1}^N m_i^2 / N$ . Eq. (A.28) implies that momenta of different massive eigenstates are not collinear. To find the deviation from collinearity of  $\bar{\mathbf{p}}$  and  $\mathbf{L}$ , we estimate

$$\frac{\bar{\mathbf{p}}}{|\bar{\mathbf{p}}|} = \frac{\mathbf{L}}{L} + \boldsymbol{\epsilon}_L. \quad (\text{A.29})$$

Since the magnitudes of both sides of this equation must be unity, we have

$$\mathbf{L} \cdot \boldsymbol{\epsilon}_L = -\frac{1}{2} |\boldsymbol{\epsilon}_L|^2 L. \quad (\text{A.30})$$

From Eqs. (A.28) and (A.26), to zero order in neutrino mass we have

$$\mathbf{p} \approx E \left( \frac{\mathbf{L}}{L} + \boldsymbol{\epsilon}_L \right), \quad \mathbf{v}_i \approx \frac{\mathbf{L}}{L} + \boldsymbol{\epsilon}_L. \quad (\text{A.31})$$

Now we use above approximations to analyze the probability expression obtained in Eq. (A.22). Let us first consider the interference term in (A.22). We have to first order in  $|\boldsymbol{\epsilon}_L|$

$$(\langle \mathbf{p}_j \rangle - \langle \mathbf{p}_k \rangle) \cdot \mathbf{L} \approx - \frac{\Delta m_{jk}^2}{2E} \boldsymbol{\xi} \cdot \mathbf{L}, \quad (\text{A.32})$$

$$\langle E_j \rangle - \langle E_k \rangle \approx \left( 1 - \frac{\mathbf{p} \cdot \boldsymbol{\xi}}{E} \right) \frac{\Delta m_{jk}^2}{2E} = \left( 1 - \frac{\boldsymbol{\xi} \cdot \mathbf{L}}{L} - \boldsymbol{\xi} \cdot \boldsymbol{\epsilon}_L \right) \frac{\Delta m_{jk}^2}{2E}, \quad (\text{A.33})$$

$$\frac{(\mathbf{v}_j + \mathbf{v}_k)}{v_j^2 + v_k^2} \cdot \mathbf{L} \approx \left( \frac{\mathbf{L}}{L} + \boldsymbol{\epsilon}_L \right) \cdot \mathbf{L} = L. \quad (\text{A.34})$$

Thus the interference term is

$$\exp \left[ -i \left( (\langle E_j \rangle - \langle E_k \rangle) \frac{\mathbf{v}_j + \mathbf{v}_k}{v_j^2 + v_k^2} - (\langle \mathbf{p}_j \rangle - \langle \mathbf{p}_k \rangle) \right) \cdot \mathbf{L} \right] \approx \exp \left[ -i \frac{\Delta m_{jk}^2 L}{2E} (1 - \boldsymbol{\xi} \cdot \boldsymbol{\epsilon}_L) \right]. \quad (\text{A.35})$$

In the collinear limit  $\boldsymbol{\xi} \cdot \boldsymbol{\epsilon}_L \rightarrow 0$ , we recover the standard oscillation phase  $\exp(-i\Delta m_{jk}^2 L/2E)$ .

Now consider the first term in second exponential in Eq. (A.22) given by

$$\exp \left[ - \frac{((\mathbf{v}_j - \mathbf{v}_k) \cdot \mathbf{L})^2}{4\sigma_x^2(v_j^2 + v_k^2)} \right], \quad (\text{A.36})$$

This term shows that different massive neutrino wave packets travel with different group velocities, so for sufficiently large distances the wave packets may separate and will not be detected coherently. In this case, only one of the massive neutrino contributes to the detection. Thus interference effects due to coherence of wave packets is lost and oscillations will not be observed. This phenomenon is called decoherence in neutrino oscillation. The distance beyond which decoherence effects start to become important is called coherence length, which we can easily derive using the above approximations. We have from Eqs.

(A.26) and (A.27)

$$\begin{aligned}
(\mathbf{v}_j - \mathbf{v}_k) \cdot \mathbf{L} &\approx -\frac{\Delta m_{jk}^2}{2E^2} \left[ \frac{\mathbf{p}}{E} \left( 1 - \frac{\mathbf{p} \cdot \boldsymbol{\xi}}{E} \right) + \boldsymbol{\xi} \right] \cdot \mathbf{L} \\
&= -\frac{\Delta m_{jk}^2 L}{2E^2} \left[ 1 - (\boldsymbol{\xi} \cdot \boldsymbol{\epsilon}_L)L + \left( 1 - \frac{\mathbf{L} \cdot \boldsymbol{\xi}}{L} \right) \frac{\boldsymbol{\epsilon}_L \cdot \mathbf{L}}{L} \right], \tag{A.37}
\end{aligned}$$

and  $\sqrt{v_j^2 + v_k^2} \approx \sqrt{2}$ .

Thus to first order in  $|\epsilon_L|$ , we get

$$\exp \left[ -\frac{((\mathbf{v}_j - \mathbf{v}_k) \cdot \mathbf{L})^2}{4\sigma_x^2(v_j^2 + v_k^2)} \right] \approx \exp \left[ -\left( \frac{\Delta m_{jk}^2 L}{4\sqrt{2}E^2\sigma_x} (1 - (\boldsymbol{\xi} \cdot \boldsymbol{\epsilon}_L)L) \right)^2 \right]. \tag{A.38}$$

In the collinear limit  $\boldsymbol{\xi} \cdot \boldsymbol{\epsilon}_L \rightarrow 0$ , we get the decoherence term  $\exp(-(L/L_{\text{coh}}^{jk})^2)$ , where the coherence length is

$$L_{\text{coh}}^{jk} = \frac{4\sqrt{2}E^2\sigma_x}{|\Delta m_{jk}^2|}. \tag{A.39}$$

The final term in Eq. (A.22) does not depend on distance  $L$  and is called localization term.

It can be approximated as following

$$\begin{aligned}
\frac{(\langle E_j \rangle - \langle E_k \rangle)^2}{4\sigma_p^2(v_j^2 + v_k^2)} &\approx \left[ \frac{\Delta m_{jk}^2}{4\sqrt{2}E\sigma_p} \left( 1 - \boldsymbol{\xi} \cdot \boldsymbol{\epsilon}_L - \frac{\boldsymbol{\xi} \cdot \mathbf{L}}{L} \right) \right]^2 \\
&\approx 2\pi^2 \left( 1 - \frac{\boldsymbol{\xi} \cdot \mathbf{L}}{L} \right)^2 \left( \frac{\sigma_x}{L_{\text{osc}}^{jk}} \right)^2, \tag{A.40}
\end{aligned}$$

where we have used Eq. (A.35) to derive the oscillation length to first order in  $|\epsilon_L|$ :

$$L_{\text{osc}}^{jk} = (1 - \boldsymbol{\xi} \cdot \boldsymbol{\epsilon}_L)^{-1} \frac{4\pi E}{\Delta m_{jk}^2} \stackrel{\boldsymbol{\xi} \cdot \boldsymbol{\epsilon}_L \rightarrow 0}{\approx} \frac{4\pi E}{\Delta m_{jk}^2} \tag{A.41}$$

$L_{\text{osc}}^{jk} = 4\pi E(1 - \boldsymbol{\xi} \cdot \boldsymbol{\epsilon}_L)^{-1}/\Delta m_{jk}^2$ . This term implies that to observe the oscillations  $\sigma_x \ll L_{\text{osc}}^{jk}$  i.e. the production and detection processes must be localized in regions much smaller than the oscillation length. Using the above approximations the transition probability in

Eq. (A.22) becomes:

$$\mathcal{P}_{\nu_\alpha \rightarrow \nu_\beta}(\mathbf{L}) = \sum_{j,k} U_{\alpha j}^* U_{\beta j} U_{\alpha k} U_{\beta k}^* \exp \left[ -2\pi i \frac{L}{L_{\text{osc}}^{jk}} - \left( \frac{L}{L_{\text{coh}}^{jk}} \right)^2 - 2\pi^2 \left( 1 - \frac{\boldsymbol{\xi} \cdot \mathbf{L}}{L} \right)^2 \left( \frac{\sigma_x}{L_{\text{osc}}^{jk}} \right)^2 \right]. \quad (\text{A.42})$$

It can be clearly seen that for  $L \ll L_{\text{coh}}^{jk}$  and  $\sigma_x \ll L_{\text{osc}}^{jk}$ , the wave packet effects are negligible and we get back the standard plane wave result (A.6). However the wave packet formalism provides us additional insights about the role of neutrino production and detection processes in oscillation experiments. From Eq. (A.39), we see that coherence length  $L_{\text{coh}}^{jk}$  is proportional to  $\sigma_x = \sqrt{\sigma_{xP}^2 + \sigma_{xD}^2}$ . It means that a precise measurement of the neutrino momentum (or energy) during detection, which implies a small  $\sigma_{pP}$  and hence a large  $\sigma_{xD}$ , will lead to a large coherence length given by  $L_{\text{coh}}^{jk} \simeq 4\sqrt{2}\sigma_{xD}E^2/|\Delta m_{jk}^2|$ . Thus because of precise measurements even those wave packets which have negligible overlap may interfere coherently during detection and give rise to oscillation pattern. However, Eq. (A.42) also implies that with increasing measurement precision of neutrino momentum (or energy), which will lead to increase in  $\sigma_x$ , the localization term starts to become more important and for  $\sigma_x > L_{\text{osc}}^{jk}$  the interference between  $\nu_j$  and  $\nu_k$  wave packets is suppressed resulting in washout of oscillation pattern. Thus the measurement of neutrino momentum or energy cannot be carried out with infinite precision without affecting the oscillation pattern.

## Size of wave packets and coherence length

In usual neutrino experiments the condition  $\sigma_x \ll L_{\text{osc}}^{jk}$  is satisfied and thus the effect of finite neutrino localization during production and detection can be neglected. Neglecting

the localization term in Eq. (A.42) we obtain the transition probability

$$\mathcal{P}_{\nu_\alpha \rightarrow \nu_\beta}(L) = \sum_{j,k} U_{\alpha j} U_{\alpha k}^* U_{\beta j}^* U_{\beta k} \exp \left[ -2\pi i \frac{L}{L_{\text{osc}}^{jk}} - \left( \frac{L}{L_{\text{coh}}^{jk}} \right)^2 \right]. \quad (\text{A.43})$$

Now the coherence length (A.39) can be written as

$$L_{\text{coh}}^{jk}(\text{km}) = \frac{4\sqrt{2}E^2(\text{GeV})\sigma_x(\text{cm})}{|\Delta m_{jk}^2(\text{eV}^2)|} \times 10^{13} \quad (\text{A.44})$$

To determine whether decoherence effects are important or not one needs to know the width of neutrino wave packets, which depends on production and detection processes, and energy spectrum of neutrinos. Next we examine two cases, one where decoherence effects are negligible and one where they are significant.

### Pion decay

In accelerator neutrino experiments proton are bombarded on a target which produces pions and kaons. These particles further decay to produce neutrino beams. Consider the decay of 1 GeV pion :  $\pi^+ \rightarrow \mu^+ + \nu_\mu$ . If  $\tau_x$  (here  $\tau_\pi \approx 2.8 \times 10^{-8}$  s) is the lifetime of the decaying particles in the rest frame then the width of the neutrino wave packet  $\sigma_x \sim \tau_x$ . However since particles decay in flight the wave packet size is dilated by Lorentz factor:  $\sigma_x \sim \gamma\tau_x$ , where  $\gamma = E_x/m_x$ ,  $E_x$  and  $m_x$  being energy and rest mass of the decaying particle. For 1 GeV pions decaying in flight  $\gamma \sim 7$ . Then Eq. (A.44) gives the coherence length for the muon neutrinos produced in the accelerator experiment

$$L_{\text{coh}}^{jk} \sim 1.7 \times 10^{20} \text{km} \quad (\text{A.45})$$

In typical accelerator experiments the detector is located at distances  $\sim 1-10^3$  km from the point of neutrino production. Thus  $L_{\text{coh}}^{jk} \gg L$  and decoherence effects can be neglected.

## Solar neutrinos

For neutrinos produced inside the Sun effects of scattering of particles with neighboring nuclei are important. These effects are called collision broadening and limit the size of the neutrino wave packets. Taking these effects into account Nussinov [204] estimated the size of wavepacket for solar neutrinos:  $\sigma_x \sim 10^{-6}$  cm. Thus for  $E \approx 100$  keV neutrinos the coherence length is

$$L_{\text{coh}}^{jk} \sim 10^3 \text{km}. \quad (\text{A.46})$$

Now the distance that solar neutrinos travel before being detected at Earth  $\sim 10^{15}$  km. Thus for the case of solar neutrinos decoherence effects take over and the oscillations due to interference among the wave packets is not observed. The effects that is more prominent for the case of solar neutrinos is called resonant adiabatic transitions that take place inside the Sun due to its varying density. These transitions convert electron type neutrinos to muon and tau neutrinos during their propagation from interior regions to the surface of the Sun producing in a net deficit of electron neutrinos.





---

## APPENDIX B

---



---

### Neutrino evolution equations and Demkov-Kunike model

---

For the case when magnetic field and density of the Sun are given by Eqs. (3.10) and (3.20) the Hamiltonian (3.19) can be written as

$$H = \begin{pmatrix} \frac{-\Delta m^2}{4E} + \frac{V_0}{2}(1 - \tanh(5r/R_\odot)) & \mu B_0 \operatorname{sech}(5r/R_\odot) \\ \mu B_0 \operatorname{sech}(5r/R_\odot) & \frac{\Delta m^2}{4E} - \frac{V_0}{2}(1 - \tanh(5r/R_\odot)) \end{pmatrix}, \quad (\text{B.1})$$

where  $V_0 = \sqrt{2}G_F Y_e^{\text{eff}} \rho_0 / m_N$  with  $\rho_0$  being the density at the solar center. We define

$$a = -\frac{\Delta m^2}{4E} + \frac{V_0}{2}, \quad (\text{B.2})$$

$$b = -\frac{V_0}{2}, \quad (\text{B.3})$$

$$c = \mu B_0. \quad (\text{B.4})$$

For ultra-relativistic neutrinos propagating along the radial direction in the Sun, the flavor equation (3.21) can now be written as

$$\begin{aligned} \frac{d^2 \nu_{eL}}{dr^2} + \frac{5}{R_\odot} \tanh(5r/R_\odot) \frac{d\nu_{eL}}{dr} + \left( c^2 \operatorname{sech}^2(5r/R_\odot) + (a + b \tanh(5r/R_\odot))^2 \right. \\ \left. + \frac{5i}{R_\odot} (a \tanh(5r/R_\odot) + b) \right) \nu_{eL} = 0. \end{aligned} \quad (\text{B.5})$$

Now substituting  $z = (1 + \tanh(5r/R_\odot))/2$ , Eq. (B.5) becomes

$$z(1-z)\frac{d^2\nu_{eL}}{dz^2} + \frac{1}{2}(1-2z)\frac{d\nu_{eL}}{dz} + c^2\left(\frac{R_\odot}{5}\right)^2 q(z)\nu_{eL} = 0, \quad (\text{B.6})$$

where

$$q(z) = 1 + \frac{1}{4c^2z(1-z)}\left(\left(a + b(2z-1)\right)^2 + \frac{5i}{R_\odot}(a(2z-1) + b)\right). \quad (\text{B.7})$$

Finally the substitution  $\nu_{eL} = z^\mu(1-z)^\nu u(z)$ , where

$$\mu = -i(a-b)R_\odot/10, \quad (\text{B.8})$$

$$\nu = i(a+b)R_\odot/10, \quad (\text{B.9})$$

converts Eq. (B.6) to a Gauss hypergeometric equation

$$z(1-z)\frac{d^2u}{dz^2} + (\gamma - (\alpha + \beta + 1)z)\frac{du}{dz} - \alpha\beta u(z) = 0, \quad (\text{B.10})$$

where

$$\alpha = \frac{R_\odot}{10}\left(ib + \sqrt{-b^2 + 4c^2}\right), \quad (\text{B.11})$$

$$\beta = \frac{R_\odot}{10}\left(ib - \sqrt{-b^2 + 4c^2}\right), \quad (\text{B.12})$$

$$\gamma = \frac{1}{2} - i(a-b)\frac{R_\odot}{5}. \quad (\text{B.13})$$

Eq. (B.10) has two linearly independent solutions which can be taken as [212]

$$\nu_{eL\pm} = z^{\pm\mu}(1-z)^\nu u_\pm(z), \quad (\text{B.14})$$

where  $u_{\pm}(z) = u(z)|_{\mu \rightarrow \pm\mu}$ . If the neutrinos are produced at the location  $r_0$  inside the Sun, then the evolution of the state  $\nu_{eL}$  is given by

$$\begin{aligned} \nu_{eL}(r) = & \cos^2 \theta_m e^{i\omega r_0} z^{\mu} (1-z)^{\nu} {}_2F_1(\alpha, \beta, \gamma; z) \\ & + \sin^2 \theta_m e^{-i\omega r_0} z^{-\mu} (1-z)^{\nu} {}_2F_1(\alpha, \beta, \gamma; z)|_{\mu \rightarrow -\mu}, \end{aligned} \quad (\text{B.15})$$

where  $\theta_m = \tan^{-1}(c/a)/2$ ,  $\omega = \sqrt{(a)^2 + (c)^2}$  and  ${}_2F_1(\alpha, \beta, \gamma; z)$  is the Gauss hypergeometric function. Since  $b^2 \gg 4c^2$ , we can use  $\alpha \approx \mu + \nu$ ,  $\beta \approx 0$  and  $\gamma = (1/2) + 2\mu$  for evaluating the survival probability given by  $P_{ee}(r_0, r) = |\nu_{eL}(r)|^2$ . The transition probability  $1 - P_{ee}(r_0, r)$  is then averaged over the  ${}^8B$  neutrino production region to put appropriate bounds on the magnetic field.



# References

- [1] M. Fukugita and T. Yanagida, *Physics of neutrinos and applications to astrophysics*. Springer, 2003.
- [2] R. N. Mohapatra and P. B. Pal, *Massive neutrinos in physics and astrophysics*. World Scientific, 2004.
- [3] K. Zuber, *Neutrino physics*. Taylor & Francis, 2004.
- [4] C. Giunti and C. W. Kim, *Fundamentals of Neutrino Physics and Astrophysics*. Oxford University Press, 2007.
- [5] S. Bilenky, *Introduction to the physics of massive and mixed neutrinos*. Springer, 2010.
- [6] Z.-Z. Xing and S. Zhou, *Neutrinos in Particle Physics, Astronomy and Cosmology*. Springer, 2011.
- [7] A. Pich, “The Standard Model of Electroweak Interactions,” in *2010 European School of High Energy Physics*, pp. 1–50. 1, 2012. [arXiv:1201.0537 \[hep-ph\]](#).
- [8] C.-N. Yang and R. L. Mills, “Conservation of Isotopic Spin and Isotopic Gauge Invariance,” *Phys. Rev.* **96** (1954) 191–195.
- [9] F. Englert and R. Brout, “Broken Symmetry and the Mass of Gauge Vector Mesons,” *Phys. Rev. Lett.* **13** (1964) 321–323.

- [10] P. W. Higgs, “Broken Symmetries and the Masses of Gauge Bosons,” *Phys. Rev. Lett.* **13** (1964) 508–509.
- [11] G. Guralnik, C. Hagen, and T. Kibble, “Global Conservation Laws and Massless Particles,” *Phys. Rev. Lett.* **13** (1964) 585–587.
- [12] T. Kibble, “Symmetry breaking in nonAbelian gauge theories,” *Phys. Rev.* **155** (1967) 1554–1561.
- [13] S. Weinberg, “A Model of Leptons,” *Phys. Rev. Lett.* **19** (1967) 1264–1266.
- [14] **ATLAS** Collaboration, G. Aad *et al.*, “Observation of a new particle in the search for the Standard Model Higgs boson with the ATLAS detector at the LHC,” *Phys. Lett. B* **716** (2012) 1–29, [arXiv:1207.7214 \[hep-ex\]](#).
- [15] **CMS** Collaboration, S. Chatrchyan *et al.*, “Observation of a New Boson at a Mass of 125 GeV with the CMS Experiment at the LHC,” *Phys. Lett. B* **716** (2012) 30–61, [arXiv:1207.7235 \[hep-ex\]](#).
- [16] **KATRIN** Collaboration, M. Aker *et al.*, “Improved Upper Limit on the Neutrino Mass from a Direct Kinematic Method by KATRIN,” *Phys. Rev. Lett.* **123** no. 22, (2019) 221802, [arXiv:1909.06048 \[hep-ex\]](#).
- [17] Z. Maki, M. Nakagawa, and S. Sakata, “Remarks on the unified model of elementary particles,” *Prog. Theor. Phys.* **28** (1962) 870–880.
- [18] B. Pontecorvo, “Neutrino Experiments and the Problem of Conservation of Leptonic Charge,” *Sov. Phys. JETP* **26** (1968) 984–988.
- [19] T.-K. Kuo and J. T. Pantaleone, “Neutrino Oscillations in Matter,” *Rev. Mod. Phys.* **61** (1989) 937.
- [20] I. Esteban, M. Gonzalez-Garcia, M. Maltoni, I. Martinez-Soler, and T. Schwetz, “Updated fit to three neutrino mixing: exploring the accelerator-reactor complementarity,” *JHEP* **01** (2017) 087, [arXiv:1611.01514 \[hep-ph\]](#).

- [21] L. Wolfenstein, “Neutrino Oscillations in Matter,” *Phys. Rev.* **D17** (1978) 2369–2374.
- [22] J. Linder, “Derivation of neutrino matter potentials induced by earth,” [arXiv:hep-ph/0504264](https://arxiv.org/abs/hep-ph/0504264).
- [23] S. P. Mikheev and A. Yu. Smirnov, “Neutrino Oscillations in a Variable Density Medium and Neutrino Bursts Due to the Gravitational Collapse of Stars,” *Sov. Phys. JETP* **64** (1986) 4–7, [arXiv:0706.0454](https://arxiv.org/abs/0706.0454) [hep-ph]. [*Zh. Eksp. Teor. Fiz.*91,7(1986)].
- [24] S. P. Mikheev and A. Yu. Smirnov, “Resonant amplification of neutrino oscillations in matter and solar neutrino spectroscopy,” *Nuovo Cim.* **C9** (1986) 17–26.
- [25] S. Bilenky, “Neutrino oscillations: From a historical perspective to the present status,” *Nucl. Phys. B* **908** (2016) 2–13, [arXiv:1602.00170](https://arxiv.org/abs/1602.00170) [hep-ph].
- [26] T. Kajita, “Nobel Lecture: Discovery of atmospheric neutrino oscillations,” *Rev. Mod. Phys.* **88** no. 3, (2016) 030501.
- [27] A. B. McDonald, “Nobel Lecture: The Sudbury Neutrino Observatory: Observation of flavor change for solar neutrinos,” *Rev. Mod. Phys.* **88** no. 3, (2016) 030502.
- [28] **T2K** Collaboration, K. Abe *et al.*, “Constraint on the matter–antimatter symmetry-violating phase in neutrino oscillations,” *Nature* **580** no. 7803, (2020) 339–344, [arXiv:1910.03887](https://arxiv.org/abs/1910.03887) [hep-ex]. [Erratum: *Nature* 583, E16 (2020)].
- [29] **Daya Bay** Collaboration, D. Adey *et al.*, “Extraction of the  $^{235}\text{U}$  and  $^{239}\text{Pu}$  Antineutrino Spectra at Daya Bay,” *Phys. Rev. Lett.* **123** no. 11, (2019) 111801, [arXiv:1904.07812](https://arxiv.org/abs/1904.07812) [hep-ex].

- [30] **BOREXINO** Collaboration, M. Agostini *et al.*, “Experimental evidence of neutrinos produced in the CNO fusion cycle in the Sun,” *Nature* **587** (2020) 577–582, [arXiv:2006.15115 \[hep-ex\]](#).
- [31] C. Giunti and A. Studenikin, “Neutrino electromagnetic interactions: a window to new physics,” *Rev. Mod. Phys.* **87** (2015) 531, [arXiv:1403.6344 \[hep-ph\]](#).
- [32] C. Giunti, K. A. Kouzakov, Y.-F. Li, A. V. Lokhov, A. I. Studenikin, and S. Zhou, “Electromagnetic neutrinos in laboratory experiments and astrophysics,” *Annalen Phys.* **528** (2016) 198–215, [arXiv:1506.05387 \[hep-ph\]](#).
- [33] M. Nowakowski, E. Paschos, and J. Rodriguez, “All electromagnetic form-factors,” *Eur. J. Phys.* **26** (2005) 545–560, [arXiv:physics/0402058](#).
- [34] C. Itzykson and J. Zuber, *Quantum Field Theory*. McGraw-Hill, New York, 1980.
- [35] B. Kayser, “Majorana neutrinos,” *Comments Nucl. Part. Phys.* **14** no. 2, (1985) 69–86.
- [36] R. E. Shrock, “Electromagnetic Properties and Decays of Dirac and Majorana Neutrinos in a General Class of Gauge Theories,” *Nucl. Phys.* **B206** (1982) 359–379.
- [37] P. B. Pal and L. Wolfenstein, “Radiative Decays of Massive Neutrinos,” *Phys. Rev.* **D25** (1982) 766.
- [38] M. Dvornikov and A. Studenikin, “Electric charge and magnetic moment of massive neutrino,” *Phys. Rev. D* **69** (2004) 073001, [arXiv:hep-ph/0305206](#).
- [39] J. Welter, *Phenomenology of neutrino magnetic moments*. PhD thesis, Heidelberg U., 2017.
- [40] H. Wong and H.-B. Li, “Neutrino magnetic moments,” *Mod. Phys. Lett. A* **20** (2005) 1103–1117.

- [41] P. Vogel and J. Engel, “Neutrino Electromagnetic Form-Factors,” *Phys. Rev. D* **39** (1989) 3378.
- [42] J. F. Beacom and P. Vogel, “Neutrino magnetic moments, flavor mixing, and the Super-Kamiokande solar data,” *Phys. Rev. Lett.* **83** (1999) 5222–5225, [arXiv:hep-ph/9907383](#).
- [43] **MUNU** Collaboration, Z. Daraktchieva *et al.*, “Final results on the neutrino magnetic moment from the MUNU experiment,” *Phys. Lett. B* **615** (2005) 153–159, [arXiv:hep-ex/0502037](#).
- [44] **TEXONO** Collaboration, H. Wong *et al.*, “A Search of Neutrino Magnetic Moments with a High-Purity Germanium Detector at the Kuo-Sheng Nuclear Power Station,” *Phys. Rev. D* **75** (2007) 012001, [arXiv:hep-ex/0605006](#).
- [45] A. G. Beda, V. B. Brudanin, V. G. Egorov, D. V. Medvedev, V. S. Pogosov, M. V. Shirchenko, and A. S. Starostin, “The results of search for the neutrino magnetic moment in GEMMA experiment,” *Adv. High Energy Phys.* **2012** (2012) 350150.
- [46] R. Allen *et al.*, “Study of electron-neutrino electron elastic scattering at LAMPF,” *Phys. Rev. D* **47** (1993) 11–28.
- [47] **LSND** Collaboration, L. Auerbach *et al.*, “Measurement of electron - neutrino - electron elastic scattering,” *Phys. Rev. D* **63** (2001) 112001, [arXiv:hep-ex/0101039](#).
- [48] **DONUT** Collaboration, R. Schwienhorst *et al.*, “A New upper limit for the tau - neutrino magnetic moment,” *Phys. Lett. B* **513** (2001) 23–29, [arXiv:hep-ex/0102026](#).
- [49] **Super-Kamiokande** Collaboration, D. Liu *et al.*, “Limits on the neutrino magnetic moment using 1496 days of Super-Kamiokande-I solar neutrino data,” *Phys. Rev. Lett.* **93** (2004) 021802, [arXiv:hep-ex/0402015](#).

- [50] **Borexino** Collaboration, M. Agostini *et al.*, “Limiting neutrino magnetic moments with Borexino Phase-II solar neutrino data,” *Phys. Rev. D* **96** no. 9, (2017) 091103, [arXiv:1707.09355 \[hep-ex\]](#).
- [51] **XENON** Collaboration, E. Aprile *et al.*, “Excess electronic recoil events in XENON1T,” *Phys. Rev. D* **102** no. 7, (2020) 072004, [arXiv:2006.09721 \[hep-ex\]](#).
- [52] K. Babu, S. Jana, and M. Lindner, “Large Neutrino Magnetic Moments in the Light of Recent Experiments,” *JHEP* **10** (2020) 040, [arXiv:2007.04291 \[hep-ph\]](#).
- [53] O. Miranda, D. Papoulias, M. Tórtola, and J. Valle, “XENON1T signal from transition neutrino magnetic moments,” *Phys. Lett. B* **808** (2020) 135685, [arXiv:2007.01765 \[hep-ph\]](#).
- [54] W. J. Marciano and A. I. Sanda, “Exotic Decays of the Muon and Heavy Leptons in Gauge Theories,” *Phys. Lett.* **B67** (1977) 303–305.
- [55] M. Czakon, J. Gluza, and M. Zralek, “Neutrino magnetic moments in left-right symmetric models,” *Phys. Rev. D* **59** (1999) 013010.
- [56] M. Fukugita and T. Yanagida, “A Particle Physics Model for Voloshin-Vysotskii-Okun Solution to the Solar Neutrino Problem,” *Phys. Rev. Lett.* **58** (1987) 1807.
- [57] K. S. Babu and V. S. Mathur, “Magnetic Moments of Dirac and Majorana Neutrinos,” *Phys. Lett.* **B196** (1987) 218–222.
- [58] S. Rajpoot, “Dirac neutrino magnetic moments in the Left-Right symmetric model,” *Phys. Lett.* **B237** (1990) 77–80.
- [59] M. Lindner, B. Radovčić, and J. Welter, “Revisiting Large Neutrino Magnetic Moments,” *JHEP* **07** (2017) 139, [arXiv:1706.02555 \[hep-ph\]](#).

- [60] N. F. Bell, V. Cirigliano, M. J. Ramsey-Musolf, P. Vogel, and M. B. Wise, “How magnetic is the Dirac neutrino?,” *Phys. Rev. Lett.* **95** (2005) 151802, [arXiv:hep-ph/0504134 \[hep-ph\]](#).
- [61] S. Davidson, M. Gorbahn, and A. Santamaria, “From transition magnetic moments to majorana neutrino masses,” *Phys. Lett. B* **626** (2005) 151–160, [arXiv:hep-ph/0506085](#).
- [62] N. F. Bell, M. Gorchtein, M. J. Ramsey-Musolf, P. Vogel, and P. Wang, “Model independent bounds on magnetic moments of Majorana neutrinos,” *Phys. Lett.* **B642** (2006) 377–383, [arXiv:hep-ph/0606248 \[hep-ph\]](#).
- [63] M. Voloshin, “On Compatibility of Small Mass with Large Magnetic Moment of Neutrino,” *Sov. J. Nucl. Phys.* **48** (1988) 512.
- [64] R. Barbieri and G. Fiorentini, “The Solar Neutrino Puzzle and the Neutrino (L)  $\rightarrow$  Neutrino (R) Conversion Hypothesis,” *Nucl. Phys.* **B304** (1988) 909–920.
- [65] P. B. Pal, “Particle physics confronts the solar neutrino problem,” *Int. J. Mod. Phys.* **A7** (1992) 5387–5460.
- [66] K. Babu and R. N. Mohapatra, “Large transition magnetic moment of the neutrino from horizontal symmetry,” *Phys. Rev. D* **42** (1990) 3778–3793.
- [67] G. Ecker, W. Grimus, and H. Neufeld, “A Light Zeldovich-konopinski-mahmoud Neutrino With a Large Magnetic Moment,” *Phys. Lett. B* **232** (1989) 217–221.
- [68] M. Leurer and N. Marcus, “A Model for a Large Neutrino Magnetic Transition Moment and Naturally Small Mass,” *Phys. Lett. B* **237** (1990) 81–87.
- [69] D. Choudhury and U. Sarkar, “Large Magnetic Moments for Near Massless Neutrinos,” *Phys. Lett. B* **235** (1990) 113–116.
- [70] D. Chang, W.-Y. Keung, and G. Senjanovic, “Neutrino transitional magnetic moment and nonAbelian discrete symmetry,” *Phys. Rev. D* **42** (1990) 1599–1603.

- [71] H. Georgi and L. Randall, “Charge Conjugation and Neutrino Magnetic Moments,” *Phys. Lett. B* **244** (1990) 196–202.
- [72] S. M. Barr, E. Freire, and A. Zee, “A Mechanism for large neutrino magnetic moments,” *Phys. Rev. Lett.* **65** (1990) 2626–2629.
- [73] A. Zee, “A Theory of Lepton Number Violation, Neutrino Majorana Mass, and Oscillation,” *Phys. Lett. B* **93** (1980) 389. [Erratum: *Phys.Lett.B* 95, 461 (1980)].
- [74] L. B. Okun, M. B. Voloshin, and M. I. Vysotsky, “Neutrino Electrodynamics and Possible Effects for Solar Neutrinos,” *Sov. Phys. JETP* **64** (1986) 446–452. [*Zh. Eksp. Teor. Fiz.* 91,754(1986)].
- [75] A. M. Egorov, A. E. Lobanov, and A. I. Studenikin, “Neutrino oscillations in electromagnetic fields,” *Phys. Lett.* **B491** (2000) 137–142, [arXiv:hep-ph/9910476](https://arxiv.org/abs/hep-ph/9910476) [hep-ph].
- [76] C.-S. Lim and W. J. Marciano, “Resonant Spin - Flavor Precession of Solar and Supernova Neutrinos,” *Phys. Rev.* **D37** (1988) 1368–1373.
- [77] E. K. Akhmedov and M. Yu. Khlopov, “Resonant Amplification of Neutrino Oscillations in Longitudinal Magnetic Field,” *Mod. Phys. Lett.* **A3** (1988) 451–457.
- [78] S. Joshi and S. R. Jain, “Neutrino spin-flavor oscillations in solar environment,” *Res. Astron. Astrophys.* **20** no. 8, (2020) 123, [arXiv:1906.09475](https://arxiv.org/abs/1906.09475) [hep-ph].
- [79] B. T. Cleveland, T. Daily, R. Davis, Jr., J. R. Distel, K. Lande, C. K. Lee, P. S. Wildenhain, and J. Ullman, “Measurement of the solar electron neutrino flux with the Homestake chlorine detector,” *Astrophys. J.* **496** (1998) 505–526.
- [80] **SAGE** Collaboration, J. N. Abdurashitov *et al.*, “Results from SAGE,” *Phys. Lett.* **B328** (1994) 234–248.

- [81] **GALLEX** Collaboration, P. Anselmann *et al.*, “GALLEX solar neutrino observations: Complete results for GALLEX II,” *Phys. Lett.* **B357** (1995) 237–247. [Erratum: *Phys. Lett.*B361,235(1995)].
- [82] **GALLEX** Collaboration, W. Hampel *et al.*, “GALLEX solar neutrino observations: Results for GALLEX III,” *Phys. Lett.* **B388** (1996) 384–396.
- [83] **Kamiokande** Collaboration, Y. Fukuda *et al.*, “Solar neutrino data covering solar cycle 22,” *Phys. Rev. Lett.* **77** (1996) 1683–1686.
- [84] S. M. Bilenky and B. Pontecorvo, “Lepton Mixing and Neutrino Oscillations,” *Phys. Rept.* **41** (1978) 225–261.
- [85] **SNO** Collaboration, Q. R. Ahmad *et al.*, “Direct evidence for neutrino flavor transformation from neutral current interactions in the Sudbury Neutrino Observatory,” *Phys. Rev. Lett.* **89** (2002) 011301, [arXiv:nucl-ex/0204008 \[nucl-ex\]](#).
- [86] **Super-Kamiokande** Collaboration, J. Hosaka *et al.*, “Solar neutrino measurements in super-Kamiokande-I,” *Phys. Rev.* **D73** (2006) 112001, [arXiv:hep-ex/0508053 \[hep-ex\]](#).
- [87] **KamLAND** Collaboration, S. Abe *et al.*, “Precision Measurement of Neutrino Oscillation Parameters with KamLAND,” *Phys. Rev. Lett.* **100** (2008) 221803, [arXiv:0801.4589 \[hep-ex\]](#).
- [88] **BOREXINO** Collaboration, M. Agostini *et al.*, “Comprehensive measurement of *pp*-chain solar neutrinos,” *Nature* **562** no. 7728, (2018) 505–510.
- [89] W. C. Haxton, R. G. Hamish Robertson, and A. M. Serenelli, “Solar Neutrinos: Status and Prospects,” *Ann. Rev. Astron. Astrophys.* **51** (2013) 21–61, [arXiv:1208.5723 \[astro-ph.SR\]](#).

- [90] M. Maltoni and A. Yu. Smirnov, “Solar neutrinos and neutrino physics,” *Eur. Phys. J. A* **52** no. 4, (2016) 87, [arXiv:1507.05287 \[hep-ph\]](#).
- [91] M. Wurm, “Solar Neutrino Spectroscopy,” *Phys. Rept.* **685** (2017) 1–52, [arXiv:1704.06331 \[hep-ex\]](#).
- [92] S. T. Petcov, “The Solar neutrino problem and solar neutrino oscillations in vacuum and in matter,” *Lect. Notes Phys.* **512** (1998) 281–328, [arXiv:hep-ph/9806466 \[hep-ph\]](#).
- [93] J. N. Bahcall and C. Pena-Garay, “Solar models and solar neutrino oscillations,” *New J. Phys.* **6** (2004) 63, [arXiv:hep-ph/0404061](#).
- [94] T.-K. Kuo and J. T. Pantaleone, “The Solar Neutrino Problem and Three Neutrino Oscillations,” *Phys. Rev. Lett.* **57** (1986) 1805–1808.
- [95] A. Cisneros, “Effect of neutrino magnetic moment on solar neutrino observations,” *Astrophys. Space Sci.* **10** (1971) 87–92.
- [96] R. Davis, “A review of the Homestake solar neutrino experiment,” *Prog. Part. Nucl. Phys.* **32** (1994) 13–32.
- [97] **KamLAND** Collaboration, K. Eguchi *et al.*, “A High sensitivity search for anti- $\nu(e)$ ’s from the sun and other sources at KamLAND,” *Phys. Rev. Lett.* **92** (2004) 071301, [arXiv:hep-ex/0310047 \[hep-ex\]](#).
- [98] E. K. Akhmedov, “Resonant Amplification of Neutrino Spin Rotation in Matter and the Solar Neutrino Problem,” *Phys. Lett.* **B213** (1988) 64–68.
- [99] S. Joshi and S. R. Jain, “Geometric phase for neutrino propagation in magnetic field,” *Phys. Lett.* **B754** (2016) 135–138, [arXiv:1601.05255 \[hep-ph\]](#).
- [100] S. Joshi and S. R. Jain, “Noncyclic geometric phases and helicity transitions for neutrino oscillations in a magnetic field,” *Phys. Rev. D* **96** no. 9, (2017) 096004, [arXiv:1703.05027 \[hep-ph\]](#).

- [101] Y. Farzan and M. Tortola, “Neutrino oscillations and Non-Standard Interactions,” *Front.in Phys.* **6** (2018) 10, [arXiv:1710.09360 \[hep-ph\]](#).
- [102] I. Lopes and J. Silk, “Dark matter imprint on  $^8\text{B}$  neutrino spectrum,” *Phys. Rev.* **D99** no. 2, (2019) 023008, [arXiv:1812.07426 \[hep-ph\]](#).
- [103] SNO Collaboration, B. Aharmim *et al.*, “Constraints on Neutrino Lifetime from the Sudbury Neutrino Observatory,” *Phys. Rev.* **D99** no. 3, (2019) 032013, [arXiv:1812.01088 \[hep-ex\]](#).
- [104] D. Yilmaz, “Combined effect of NSI and SFP on solar electron neutrino oscillation,” *Adv. High Energy Phys.* **2016** (2016) 1435191, [arXiv:1601.03161 \[hep-ph\]](#).
- [105] J. Schechter and J. W. F. Valle, “Majorana Neutrinos and Magnetic Fields,” *Phys. Rev.* **D24** (1981) 1883–1889. [Erratum: *Phys. Rev.* **D25**,283(1982)].
- [106] B. W. Lee and R. E. Shrock, “Natural Suppression of Symmetry Violation in Gauge Theories: Muon - Lepton and Electron Lepton Number Nonconservation,” *Phys. Rev.* **D16** (1977) 1444.
- [107] E. Torrente-Lujan, “KamLAND bounds on solar anti-neutrinos and neutrino transition magnetic moments,” *JHEP* **04** (2003) 054, [arXiv:hep-ph/0302082 \[hep-ph\]](#).
- [108] E. K. Akhmedov and J. Pulido, “Solar neutrino oscillations and bounds on neutrino magnetic moment and solar magnetic field,” *Phys. Lett.* **B553** (2003) 7–17, [arXiv:hep-ph/0209192 \[hep-ph\]](#).
- [109] O. G. Miranda, T. I. Rashba, A. I. Rez, and J. W. F. Valle, “Enhanced solar anti-neutrino flux in random magnetic fields,” *Phys. Rev.* **D70** (2004) 113002, [arXiv:hep-ph/0406066 \[hep-ph\]](#).

- [110] M. M. Guzzo, P. C. de Holanda, and O. L. G. Peres, “Random magnetic fields inducing solar neutrino spin-flavor precession in a three generation context,” *Phys. Rev. D* **72** (2005) 073004, [arXiv:hep-ph/0504185](#) [hep-ph].
- [111] B. C. Chauhan, J. Pulido, and R. S. Raghavan, “Low energy solar neutrinos and spin flavor precession,” *JHEP* **07** (2005) 051, [arXiv:hep-ph/0504069](#) [hep-ph].
- [112] A. B. Balantekin and C. Volpe, “Does the neutrino magnetic moment have an impact on solar physics?,” *Phys. Rev. D* **72** (2005) 033008, [arXiv:hep-ph/0411148](#) [hep-ph].
- [113] A. Friedland, “Do solar neutrinos probe neutrino electromagnetic properties?,” [arXiv:hep-ph/0505165](#) [hep-ph].
- [114] C. R. Das, J. Pulido, and M. Picariello, “Light sterile neutrinos, spin flavour precession and the solar neutrino experiments,” *Phys. Rev. D* **79** (2009) 073010, [arXiv:0902.1310](#) [hep-ph].
- [115] Y. Fan, “Magnetic fields in the solar convection zone,” *Living Reviews in Solar Physics* **6** no. 1, (2009) 4.
- [116] R. Dicke, “A magnetic core in the sun? the solar rotator,” *Solar Physics* **78** no. 1, (1982) 3–16.
- [117] A. Friedland and A. Gruzinov, “Bounds on the magnetic fields in the radiative zone of the sun,” *Astrophys. J.* **601** (2004) 570–576, [arXiv:astro-ph/0211377](#) [astro-ph].
- [118] S. Couvidat, S. Turck-Chieze, and A. G. Kosovichev, “Solar seismic models and the neutrino predictions,” *Astrophys. J.* **599** (2003) 1434–1448, [arXiv:astro-ph/0203107](#) [astro-ph].

- [119] N. Boruta, “Solar dynamo surface waves in the presence of a primordial magnetic field: A 30 gauss upper limit in the solar core,” *Astrophys. J.* **458** (1996) 832.
- [120] H. M. Antia, “Subsurface magnetic fields from helioseismology,” *ESA Spec. Publ.* **505** (2002) 71, [arXiv:astro-ph/0208339](#) [astro-ph].
- [121] O. G. Miranda, C. Pena-Garay, T. I. Rashba, V. B. Semikoz, and J. W. F. Valle, “The Simplest resonant spin flavor solution to the solar neutrino problem,” *Nucl. Phys.* **B595** (2001) 360–380, [arXiv:hep-ph/0005259](#) [hep-ph].
- [122] J. Barranco, D. Delepine, M. Napsuciale, and A. Yebra, “Distinguishing Dirac and Majorana neutrinos with astrophysical fluxes,” [arXiv:1704.01549](#) [hep-ph].
- [123] J. N. Bahcall, A. M. Serenelli, and S. Basu, “New solar opacities, abundances, helioseismology, and neutrino fluxes,” *Astrophys. J.* **621** (2005) L85–L88, [arXiv:astro-ph/0412440](#) [astro-ph].
- [124] C. Aneziris and J. Schechter, “Three majorana neutrinos in a twisting magnetic field,” *Phys. Rev.* **D45** (1992) 1053–1058.
- [125] D. Yilmaz, “An analytic solution to the spin flavor precession for solar Majorana neutrinos in the case of three neutrino generations,” *Turk. J. Phys.* **42** no. 5, (2018) 600–612, [arXiv:1704.04756](#) [hep-ph].
- [126] K.-A. Suominen and B. Garraway, “Population transfer in a level-crossing model with two time scales,” *Phys. Rev.* **A45** no. 1, (1992) 374.
- [127] M. Kenmoe, A. Tchapa, and L. Fai, “Demkov-kunike models with decay,” *J. Math. Phys.* **57** no. 12, (2016) 122106.
- [128] **Borexino** Collaboration, G. Bellini *et al.*, “Study of solar and other unknown anti-neutrino fluxes with Borexino at LNGS,” *Phys. Lett.* **B696** (2011) 191–196, [arXiv:1010.0029](#) [hep-ex].

- [129] A. Friedland, “On the evolution of the neutrino state inside the sun,” *Phys. Rev.* **D64** (2001) 013008, [arXiv:hep-ph/0010231](#) [hep-ph].
- [130] H. J. Mosquera Cuesta and G. Lambiase, “Neutrino mass spectrum from gravitational waves generated by double neutrino spin-flip in supernovae,” *Astrophys. J.* **689** (2008) 371, [arXiv:0809.0526](#) [astro-ph].
- [131] S. Joshi, *Geometric Phase*. Credit Seminar Report, HBNI, 2017.
- [132] M. V. Berry, “Quantal phase factors accompanying adiabatic changes,” *Proc. Roy. Soc. Lond.* **A392** (1984) 45–57.
- [133] S. Pancharatnam, “Generalized theory of interference and its applications,” in *Proceedings of the Indian Academy of Sciences-Section A*, vol. 44, pp. 398–417, Springer. 1956.
- [134] C. A. Mead, “The geometric phase in molecular systems,” *Rev. Mod. Phys.* **64** (1992) 51–85.
- [135] T. Bitter and D. Dubbers, “Manifestation of Berry’s topological phase in neutron spin rotation,” *Phys. Rev. Lett.* **59** (1987) 251–254.
- [136] A. Tomita and R. Y. Chiao, “Observation of Berry’s Topological Phase by Use of an Optical Fiber,” *Phys. Rev. Lett.* **57** (1986) 937–940.
- [137] F. Wilczek and A. Shapere, *Geometric phases in physics*, vol. 5. World Scientific, 1989.
- [138] C. Pedder, J. Sonner, and D. Tong, “The Geometric Phase in Supersymmetric Quantum Mechanics,” *Phys. Rev.* **D77** (2008) 025009, [arXiv:0709.0731](#) [hep-th].
- [139] A. Capolupo, “Probing CPT violation in meson mixing by non-cyclic phase,” *Phys. Rev.* **D84** (2011) 116002, [arXiv:1112.1337](#) [hep-ph].

- [140] A. Capolupo, G. Lambiaseand, and G. Vitiello, “Probing mixing of photons and axion-like particles by geometric phase,” *Adv. High Energy Phys.* **2015** (2015) 826051, [arXiv:1510.07288 \[hep-ph\]](#).
- [141] L. I. Schiff, *Quantum Mechanics*. McGraw-Hill, 1968.
- [142] A. Messiah, *Quantum mechanics, Vol. 2*. North Holland, 1961.
- [143] B. R. Holstein, “The adiabatic theorem and berry’s phase,” *Am. J. Phys.* **57** (1989) 1079–1084.
- [144] B. Simon, “Holonomy, the quantum adiabatic theorem, and Berry’s phase,” *Phys. Rev. Lett.* **51** (1983) 2167–2170.
- [145] J. W. Zwanziger, M. Koenig, and A. Pines, “Berry’s phase,” *Ann. Rev. Phys. Chem.* **41** (1990) 601–646.
- [146] Y. Aharonov and J. Anandan, “Phase Change During a Cyclic Quantum Evolution,” *Phys. Rev. Lett.* **58** (1987) 1593.
- [147] D. Chruscinski and A. Jamiolkowski, *Geometric phases in classical and quantum mechanics*. Springer Science & Business Media, 2012.
- [148] J. Samuel and R. Bhandari, “General Setting for Berry’s Phase,” *Phys. Rev. Lett.* **60** (1988) 2339–2342.
- [149] G. Garcia de Polavieja and E. Sjoqvist, “Extending the quantal adiabatic theorem: Geometry of noncyclic motion,” *Am. J. Phys.* **66** (1998) 431, [arXiv:quant-ph/9801013 \[quant-ph\]](#).
- [150] N. Mukunda and R. Simon, “Quantum kinematic approach to the geometric phase. 1. General formalism,” *Annals Phys.* **228** (1993) 205–268.
- [151] N. Nakagawa, “Geometrical Phase Factors and Higher Order Adiabatic Approximations,” *Annals Phys.* **179** (1987) 145.

- [152] J. Vidal and J. Wudka, “Nondynamical contributions to left-right transitions in the solar neutrino problem,” *Phys. Lett.* **B249** (1990) 473–477.
- [153] A. Yu. Smirnov, “The Geometrical phase in neutrino spin precession and the solar neutrino problem,” *Phys. Lett.* **B260** (1991) 161–164.
- [154] V. A. Naumov, “Three neutrino oscillations in matter, CP violation and topological phases,” *Int. J. Mod. Phys.* **D1** (1992) 379–399.
- [155] V. A. Naumov, “Berry’s phases for three neutrino oscillations in matter,” *Phys. Lett.* **B323** (1994) 351–359.
- [156] M. Blasone, P. A. Henning, and G. Vitiello, “Berry phase for oscillating neutrinos,” *Phys. Lett.* **B466** (1999) 262–266, [arXiv:hep-th/9902124](#) [hep-th].
- [157] X.-B. Wang, L. C. Kwek, Y. Liu, and C. H. Oh, “Noncyclic geometric phase for neutrino oscillation,” *Phys. Rev.* **D63** (2001) 053003, [arXiv:hep-ph/0006204](#) [hep-ph].
- [158] X.-G. He, X.-Q. Li, B. H. J. McKellar, and Y. Zhang, “Berry phase in neutrino oscillations,” *Phys. Rev.* **D72** (2005) 053012, [arXiv:hep-ph/0412374](#) [hep-ph].
- [159] Z. Y. Law, A. H. Chan, and C. H. Oh, “Non-cyclic phase for 4-flavor neutrino oscillation,” *Phys. Lett.* **B648** (2007) 289–293.
- [160] P. Mehta, “Topological phase in two flavor neutrino oscillations,” *Phys. Rev.* **D79** (2009) 096013, [arXiv:0901.0790](#) [hep-ph].
- [161] J. Dajka, J. Syska, and J. Luczka, “Geometric phase of neutrino propagating through dissipative matter,” *Phys. Rev.* **D83** (2011) 097302, [arXiv:1309.7628](#) [hep-ph].

- [162] Z. Wang and H. Pan, “Exploration of CPT violation via time-dependent geometric quantities embedded in neutrino oscillation through fluctuating matter,” *Nucl. Phys. B* **915** (2017) 414–430, [arXiv:1512.02777 \[quant-ph\]](#).
- [163] A. Capolupo, S. Giampaolo, B. Hiesmayr, and G. Vitiello, “Geometric phase of neutrinos: differences between Dirac and Majorana neutrinos,” *Phys. Lett. B* **780** (2018) 216–220, [arXiv:1610.08679 \[hep-ph\]](#).
- [164] L. Johns and G. M. Fuller, “Geometric phases in neutrino oscillations with nonlinear refraction,” *Phys. Rev. D* **95** no. 4, (2017) 043003, [arXiv:1612.06940 \[hep-ph\]](#).
- [165] K. Dixit, A. K. Alok, S. Banerjee, and D. Kumar, “Geometric phase and neutrino mass hierarchy problem,” *J. Phys. G* **45** no. 8, (2018) 085002, [arXiv:1703.09894 \[hep-ph\]](#).
- [166] V. Bargmann, L. Michel, and V. L. Telegdi, “Precession of the polarization of particles moving in a homogeneous electromagnetic field,” *Phys. Rev. Lett.* **2** (1959) 435–436.
- [167] E. K. Akhmedov, A. Yu. Smirnov, and P. I. Krastev, “Resonant neutrino spin flip transitions in twisting magnetic fields,” *Z. Phys.* **C52** (1991) 701–709.
- [168] R. P. Feynman, F. L. Vernon, Jr., and R. W. Hellwarth, “Geometrical Representation of the Schrodinger Equation for Solving Maser Problems,” *J. Appl. Phys.* **28** (1957) 49–52.
- [169] V. V. Usov, “Millisecond pulsars with extremely strong magnetic fields as a cosmological source of gamma-ray bursts,” *Nature* **357** (1992) 472–474.
- [170] D. Lai and S. L. Shapiro, “Cold equation of state in a strong magnetic field - Effects of inverse beta-decay,” *Astrophys. J.* **383** (1991) 745.

- [171] G. Baym and C. Pethick, “Neutron Stars,” *Annu. Rev. Nucl. Part. Sci.* **25** (1975) 27–77.
- [172] J. M. Lattimer and M. Prakash, “The physics of neutron stars,” *Science* **304** (2004) 536–542, [arXiv:astro-ph/0405262](#) [astro-ph].
- [173] S. L. Shapiro and S. A. Teukolsky, *Black Holes, White Dwarfs, and Neutron Stars: The Physics of Compact Objects*. Wiley, New York, 1983.
- [174] H.-Y. Chiu and E. E. Salpeter, “Surface X-Ray Emission from Neutron Stars,” *Phys. Rev. Lett.* **12** (1964) 413–415.
- [175] D. G. Yakovlev, A. D. Kaminker, O. Y. Gnedin, and P. Haensel, “Neutrino emission from neutron stars,” *Phys. Rept.* **354** (2001) 1, [arXiv:astro-ph/0012122](#) [astro-ph].
- [176] J. M. Lattimer and M. Prakash, “The Equation of State of Hot, Dense Matter and Neutron Stars,” *Phys. Rep.* **621** (2016) 127–164, [arXiv:1512.07820](#) [astro-ph.SR].
- [177] D. Bandyopadhyay, S. Chakrabarty, and S. Pal, “The Quantizing magnetic field and quark - hadron phase transition in a neutron star,” *Phys. Rev. Lett.* **79** (1997) 2176–2179, [arXiv:astro-ph/9703066](#) [astro-ph].
- [178] G. G. Likhachev and A. I. Studenikin, “Neutrino oscillations in the magnetic field of the sun, supernovae, and neutron stars,” *J. Exp. Theor. Phys.* **81** (1995) 419–425. [*Zh. Eksp. Teor. Fiz.*108,769(1995)].
- [179] I. M. Georgescu, S. Ashhab, and F. Nori, “Quantum Simulation,” *Rev. Mod. Phys.* **86** (2014) 153, [arXiv:1308.6253](#) [quant-ph].
- [180] Z. S. Wang, X. Cai, and H. Pan, “Trapped ionic simulation of neutrino electromagnetic properties in neutrino oscillation,” *Nucl. Phys.* **B900** (2015) 560–575.

- [181] D. Suter, G. C. Chingas, R. A. Harris, and A. Pines, “Berry’s phase in magnetic resonance,” *Molecular Physics* **61** no. 6, (1987) 1327–1340.
- [182] S. Joshi, “Mixed state geometric phase for neutrino oscillations,” *Phys. Lett. B* **809** (2020) 135766, [arXiv:2008.07952 \[hep-ph\]](#).
- [183] C. Kim, J. Kim, and W. Sze, “On the Geometrical Representation of Neutrino Oscillations in Vacuum and Matter,” *Phys. Rev. D* **37** (1988) 1072.
- [184] C. Kim, W. Sze, and S. Nussinov, “On Neutrino Oscillations and the Landau-zener Formula,” *Phys. Rev. D* **35** (1987) 4014.
- [185] I. J. R. Aitchison and K. Wanelik, “On the real and complex geometric phases,” *Proc. Roy. Soc. Lond.* **A439** (1992) 25–34.
- [186] A. K. Pati, “Geometric aspects of noncyclic quantum evolutions,” *Phys. Rev. A* **52** (1995) 2576.
- [187] S. R. Jain and A. K. Pati, “Adiabatic Geometric Phases and Response Functions,” *Phys. Rev. Lett.* **80** (1998) 650–653.
- [188] C. Giunti, “No Effect of Majorana Phases in Neutrino Oscillations,” *Phys. Lett. B* **686** (2010) 41–43, [arXiv:1001.0760 \[hep-ph\]](#).
- [189] K. Singh, D. Tong, K. Basu, J. Chen, and J. Du, “Geometric phases for nondegenerate and degenerate mixed states,” *Phys. Rev. A* **67** no. 3, (2003) 032106.
- [190] A. Uhlmann, “Parallel transport and “quantum holonomy” along density operators,” *Rept. Math. Phys.* **24** no. 2, (1986) 229–240.
- [191] E. Sjöqvist, A. K. Pati, A. Ekert, J. S. Anandan, M. Ericsson, D. K. Oi, and V. Vedral, “Geometric phases for mixed states in interferometry,” *Phys. Rev. Lett.* **85** no. 14, (2000) 2845.

- [192] A. K. Pati, “Geometric phases for mixed states during unitary and non-unitary evolutions,” *Int. J. Quant. Inf.* **1** no. 01, (2003) 135–152.
- [193] E. Sjöqvist, “Geometric phases in quantum information,” *Int. J. Quant. Chem.* **115** no. 19, (2015) 1311–1326.
- [194] P. B. Slater, “Mixed state holonomies,” *Lett. Math. Phys.* **60** no. 2, (2002) 123–133.
- [195] M. Ericsson, A. K. Pati, E. Sjöqvist, J. Brännlund, and D. K. Oi, “Mixed state geometric phases, entangled systems, and local unitary transformations,” *Phys. Rev. Lett.* **91** no. 9, (2003) 090405.
- [196] U. Fano, “Description of states in quantum mechanics by density matrix and operator techniques,” *Rev. Mod. Phys.* **29** no. 1, (1957) 74.
- [197] D. Bruss and L. Sehgal, “Distinguishing a coherent from an incoherent mixture of neutrino flavors,” *Phys. Lett.* **B216** (1989) 426–430.
- [198] B. Jones, “Dynamical pion collapse and the coherence of conventional neutrino beams,” *Phys. Rev.* **D91** no. 5, (2015) 053002, [arXiv:1412.2264](https://arxiv.org/abs/1412.2264) [hep-ph].
- [199] X.-K. Song, Y. Huang, J. Ling, and M.-H. Yung, “Quantifying Quantum Coherence in Experimentally-Observed Neutrino Oscillations,” *Phys. Rev. A* **98** no. 5, (2018) 050302, [arXiv:1806.00715](https://arxiv.org/abs/1806.00715) [hep-ph].
- [200] M. Byrd, L. J. Boya, M. Mims, and E. Sudarshan, “Geometry of n-state systems, pure and mixed,” *J.Phys.:Conf. Ser.* **87** (2007) 012006.
- [201] **Super-Kamiokande** Collaboration, Y. Fukuda *et al.*, “Evidence for oscillation of atmospheric neutrinos,” *Phys. Rev. Lett.* **81** (1998) 1562–1567, [arXiv:hep-ex/9807003](https://arxiv.org/abs/hep-ex/9807003) [hep-ex].

- [202] **SNO Collaboration**, Q. R. Ahmad *et al.*, “Measurement of the rate of  $\nu_e + d \rightarrow p + p + e^-$  interactions produced by  $^8B$  solar neutrinos at the Sudbury Neutrino Observatory,” *Phys. Rev. Lett.* **87** (2001) 071301, [arXiv:nucl-ex/0106015 \[nucl-ex\]](#).
- [203] **Particle Data Group** Collaboration, C. Patrignani *et al.*, “Review of Particle Physics,” *Chin. Phys.* **C40** no. 10, (2016) 100001.
- [204] S. Nussinov, “Solar Neutrinos and Neutrino Mixing,” *Phys. Lett.* **63B** (1976) 201–203.
- [205] M. Zralek, “From kaons to neutrinos: Quantum mechanics of particle oscillations,” *Acta Phys. Polon.* **B29** (1998) 3925–3956, [arXiv:hep-ph/9810543 \[hep-ph\]](#).
- [206] M. Beuthe, “Oscillations of neutrinos and mesons in quantum field theory,” *Phys. Rept.* **375** (2003) 105–218, [arXiv:hep-ph/0109119 \[hep-ph\]](#).
- [207] C. Giunti, “Coherence and wave packets in neutrino oscillations,” *Found. Phys. Lett.* **17** (2004) 103–124, [arXiv:hep-ph/0302026](#).
- [208] E. Akhmedov, J. Kopp, and M. Lindner, “Collective neutrino oscillations and neutrino wave packets,” *JCAP* **09** (2017) 017, [arXiv:1702.08338 \[hep-ph\]](#).
- [209] **Daya Bay** Collaboration, F. P. An *et al.*, “Study of the wave packet treatment of neutrino oscillation at Daya Bay,” *Eur. Phys. J. C* **77** no. 9, (2017) 606, [arXiv:1608.01661 \[hep-ex\]](#).
- [210] S. Joshi, *Open quantum systems and decoherence in neutrino oscillations*. Credit Seminar Report, HBNI, 2017.
- [211] C. Giunti and C. W. Kim, “Coherence of neutrino oscillations in the wave packet approach,” *Phys. Rev.* **D58** (1998) 017301, [arXiv:hep-ph/9711363 \[hep-ph\]](#).

[212] D. Notzold, “Exact Analytic Solutions for Mikheev-smirnov-wolfenstein Level Crossings,” *Phys. Rev.* **D36** (1987) 1625.